The Isolation and Study of Rheological and Mass Transfer Parameters in the Spinning of Advanced Hollow Fibre Membranes for Gas Separation

By

Iain Douglas Sharpe BEng (Hons)

A thesis submitted for the degree of Doctor of Philosophy at The Department of Chemical and Process Engineering

University of Strathclyde

Glasgow

2002

Declaration of Author's Rights

Acknowledgements

First I would like to thank my supervisor Dr Simon J. Shilton for his patience and understanding throughout the duration of this research. His interest and support coupled with an informal and friendly environment led to an enjoyable period of study.

I gratefully thank Mr. Jim Murphy and the other workshop technicians Mr. Les Allan and Mr. John Wilkie for their outstanding workmanship, interest and support throughout the course of my research.

Thanks to the Departmental secretaries for keeping me supplied in pens and biscuits during my studies.

Thanks to Dr. Sergey Gordeyev for useful discussion and information on rheology and also on reinforcing and filling polymers.

Thanks to Dr. Nick Hudson and Mr. Jim Morrow for help in studying the mechanical properties of fibres.

Thanks also to Prof. C. D. Grant for tolerating and then employing me.

Abstract

The main objective of this investigation was to study in detail the fundamental parameters of extrusion shear and forced convection residence time in the dry gap in dry/wet spinning of hollow fibre gas separation membranes. To achieve this, studies were undertaken in which extrusion shear and forced convection residence time were, for the first time de-coupled and studied in isolation. Much of the previous work in the literature has concentrated on the effects of precipitation conditions i.e. phase inversion on membrane formation. This study adopts a rheological perspective and closely considers the mass transfer and skin formation processes in the dry gap.

In the first phase of work two spinning programmes were carried out; one where extrusion shear was varied while forced convection residence time was kept constant and the second where forced convection residence time was varied at constant extrusion shear. In both campaigns the dry gap chamber height was altered as appropriate. The studies utilised a sophisticated multi-component polymer dope designed to produce asymmetric gas separation membranes from forced convection dry/wet phase inversion. The forced convection system utilised here was of a unique design that produced aggressive mass transfer conditions.

The resulting fibres were studied using a combination of gas permeation testing, structural modelling studies, mechanical studies and electron microscopy. These studies showed the previously undiscovered effect of extrusion shear on membrane active layer thickness and the subtle effects of forced convection residence time. The fibres produced displayed above recognised intrinsic selectivities for the gas

separations studied and this was attributed to shear enhanced molecular orientation in the membrane active layer. The membranes from this phase were however mechanically weak.

The second phase of work utilised a homologous higher polymer content dope to spin tougher membranes - ones that would withstand an industrial environment. Again, the experimental campaigns were designed to isolate shear and forced convection residence time so both could be studied independently. The spinning rig had to be modified to accommodate the increase in viscosity of the high polymer content spinning dope.

The second phase "industrial" membranes were again studied using gas permeation studies, structural modelling, mechanical studies and electron microscopy. Due to the unique nature of the forced convection process in the spin line, the resulting fibres while displaying increased mechanical strength and intrinsic selectivity where not productive enough to be utilised in an industrial environment. Their skins were too thick and hence membrane permeability was prohibitively low.

To solve the strength vs. gas separation properties conflict, a third phase of research was carried out to strengthen membranes spun from the lower concentration dope by introducing a sub micron filler: Vapour Grown Carbon Fibre (VGCF). It was hoped that these mechanically reinforced composite hollow fibres would be both robust and exhibit attractive gas separation properties. These unique membranes displayed the

productivity of the previous low polymer content fibres and indeed increased mechanical strength, but were unfortunately less selective due to surface defects.

The fourth phase of work involved developing two more models to closely study the mass transfer occurring in the forced convection process and the skin formation mechanism during dry/wet spinning. The first model developed described the different areas of mass transfer in the forced convection chamber. This model explained the unique nature of the forced convection process in this spin line. The second model related the formation of the active layer to residence time in the dry gap.

Further work should be undertaken to study the effect of extrusion shear on polymer solubility and phase inversion in order to produce high strength super selective membranes in the future.

Table of Contents

List of Tables

List of Figures

List of Symbols

A	Membrane area
A_p	Area of pores on membrane surface
b	Hole affinity constant
C	Concentration
C_D	Concentration dissolved by Henrys' law
C_H	Concentration dissolved in microcavities (Langmuir isotherm)
C'_H	Hole saturation coefficient
CED	Cohesive energy density of polymer
D	Diffusion coefficient
D_o	Constant in eqn. 1.12
d_m	Molecule diameter
E_{app}	Apparent activation energy for diffusion
E_D	Actual activation energy for diffusion
G	Polymer shear modulus
J	Flux
k_D	Henrys' law constant
L	Length of pore
l	membrane thickness
M_a	Molecular weight of component a
N	Avogadros' Number
P_i	Permeability coefficient of component i
P_i	Pressure normalised flux of component i
P_c	Capillary pressure

Δp	Pressure difference
p	Pressure
Q	Flow rate
R_o	Universal gas constant
r	Radius of pore
S	Henrys' law solubility coefficient
T	Temperature
T_g	Glass transition temperature
x	Co-ordinate direction of permeation in polymer
y	Mole fraction

Greek Symbols

α^i_j	Ideal or intrinsic selectivity from permeability coefficient
γ	Surface tension
$\dot{\gamma}$	Shear rate
$\dot{\varepsilon}$	Strain rate
η	Viscosity
η_e	Elongational viscosity
λ	Membrane skin thickness
λ	Mean free path of molecule in eqn. 1.1
λ	Length of cylindrical void in eqn. 1.13
Ω^i_j	Selectivity with respect to components i and j
ρ	Density
σ	Elongational stress

Chapter 1:

Introduction

1.1 History

The scientific discovery of membranes can be traced to 1748 and Abbe Nollets invention of the word osmosis [1]. He observed the flux of water into an alcohol filled vessel sealed with an animal bladder. The bladder swelled and even burst due to the influx of water.

In 1831 Mitchell carried out the first gas separation experiments using membranes [2]. He observed the rates of escape for different gases from India rubber balloons under identical conditions.

The first use of synthetic membranes in gas separation studies was by Fick in 1855 [3]. In his studies "Uber diffusion" he used membranes prepared from collodin (nitro-cellulose). He stated that the flux within a medium is proportional to the concentration gradient (now known as Ficks' first law). The constant of proportionality he defined as the diffusion coefficient or diffusivity.

In 1860 Graham systematically studied the molecular mobility in porous and non-porous membranes [4]. He observed the enrichment of oxygen in air using a rubber coated paper bag. As a result of his experiments using natural rubber he proposed the "solution-diffusion" mechanism of transport. This is still the basis of today's understanding of the penetration of gases in non-porous media. When a gas is at a higher pressure on one face of a membrane it dissolves to an equilibrium

concentration at that face and diffuses across the membrane and down the concentration gradient to the far side where it evaporates.

Von Wroblewski quantified Grahams work in 1879 [5]. He demonstrated that a gas dissolves into a polymer to a concentration that is directly proportional to the pressure above it (Henrys' law is obeyed). This combined with Ficks' first law led Von Wroblewski to define the "permeability coefficient". He showed that in general gas flux was directly proportional to the pressure gradient and inversely proportional to the thickness of the membrane. He also showed that the permeability coefficient corresponded to the product of the diffusivity and the solubility. Membranes can separate gases because their permeabilities differ.

All this pioneering work remained of little relevance to the industrial gas separation community until the ground breaking work of Loeb and Sourirajan in 1962 [6]. Early membrane gas separation processes were limited by the low productivity of the thick membranes produced.

Loeb and Sourirajan developed asymmetric membranes using a phase inversion technique. The structure of these new membranes consisted of a thin non-porous active layer supported on a porous sub structure.

Fig 1.1 Asymmetric Membrane Structure

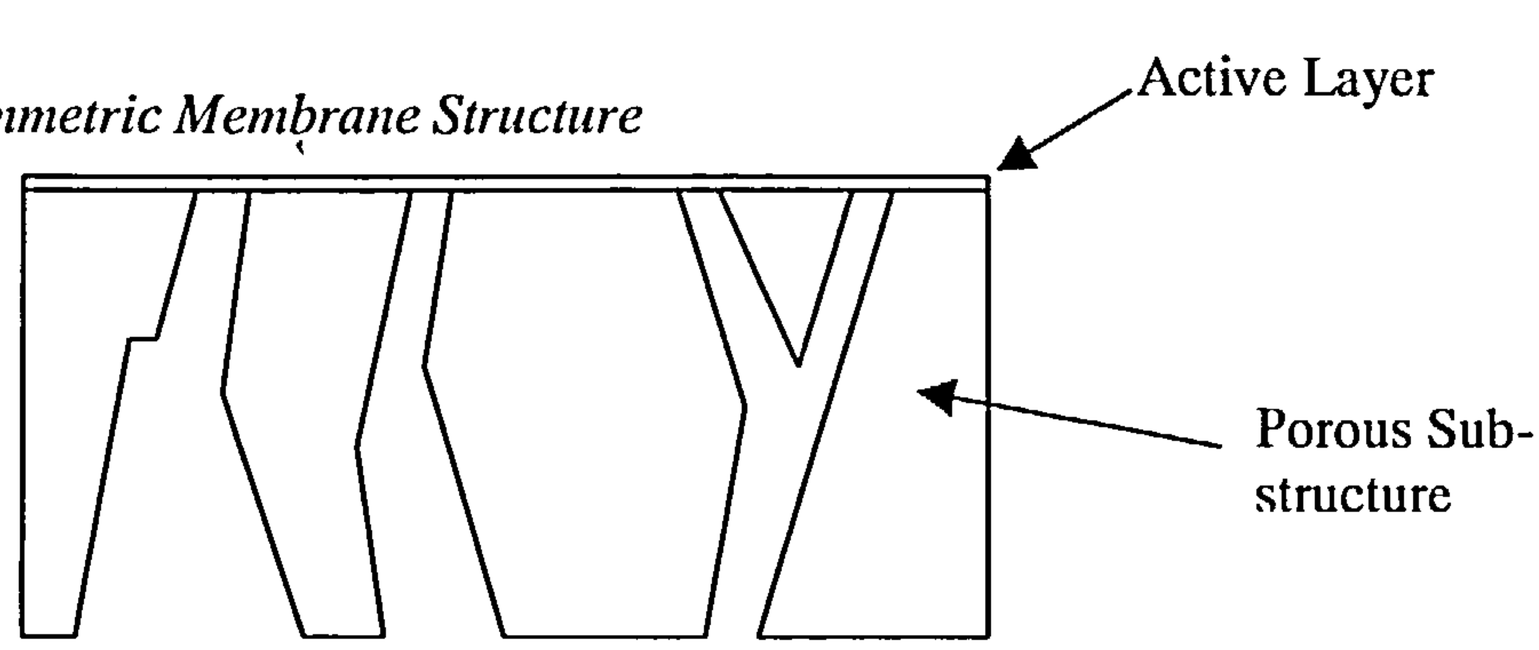

The thickness of the active layer was of the order 0.1 to 1 micron. Typical membranes of the time were of the order 100 to 200 microns thick. This 1000 fold decrease in apparent membrane thickness opened the door to much larger fluxes and large scale industrial use.

Despite the discovery of Loeb and Sourirajan it was another twenty years and another major breakthrough before the first successful commercial gas separation membrane process was launched.

In 1980 Henis and Tripodi developed a method for repairing surface defects in membranes [7,8]. Even the tiniest percentage of surface porosity can render a membrane useless for gas separation. [9] The repair method developed by Henis and Tripodi enabled membranes to realise the full separation potential of the polymer used in their construction.

1.2 Commercial Development

There are 3 main types of membrane geometry: flat sheet, tubular and hollow fibre. These different membrane forms can be built into different types of module as shown in Table 1.1.

Table1.1 Types of Membrane Module [10]

Module type	Tubular	Plate and Frame	Spiral wound	Hollow fibre
Packing density (m^2/m^3)	<300	100-400	300-1000	Up to 30000
Manufacturing cost ($/$m^2$)	50-200	100-300	30-100	5-20
Resistance to fouling	Very good	Good	Moderate	Very poor
Parastatic pressure drops	Low	Moderate	Moderate	High
Suitable for high pressure operation	With Difficulty	With Difficulty	Yes	Yes
Membrane Replacement	Yes	Yes	No	No

As can be seen from the table hollow fibres offer excellent properties for gas separation processes. They offer unrivalled surface area per unit volume of module and can withstand high pressure operation resulting in productive modules that can handle large volumes of gas. The high pressure results in a product gas at a useful pressure without the need for recompression.

The choice of material is also important in the design of a gas separation system. The membrane must be as selective and permeable as possible. In order to produce ever more effective membranes many novel polymers have been invented. Table 1.2 below traces the development of some significant polymers used in membrane formation.

Table1.2 [11] Polymer Development

Year	Polymer	α O_2/N_2	P O_2 Barrers
1982	4-methyl-1-pentene (TPX)	3.6	24.0
1985	Ethyl cellulose	3.4	15.0
1986	Polysulfone	6.0	1.2
1989	Polyphenylene oxide	4.0	16.0
1989	Halogen substituted polycarbonates	6.5	3.5
1996	Polyimides	6-9	0.1-4.0

The task is to design ever more selective and permeable polymers that also have suitable properties in order to produce a membrane that is easily fabricated and mechanically sound.

The structure of the membrane is also of vital importance in producing a successful process. The membrane must have as thin an active layer as possible in order to

increase flux but must also be defect free in order to furnish the high selectivities required in a commercial process.

The process to produce a successful system is summarised in Fig 1.2.

Fig 1.2 Critical Membrane Considerations

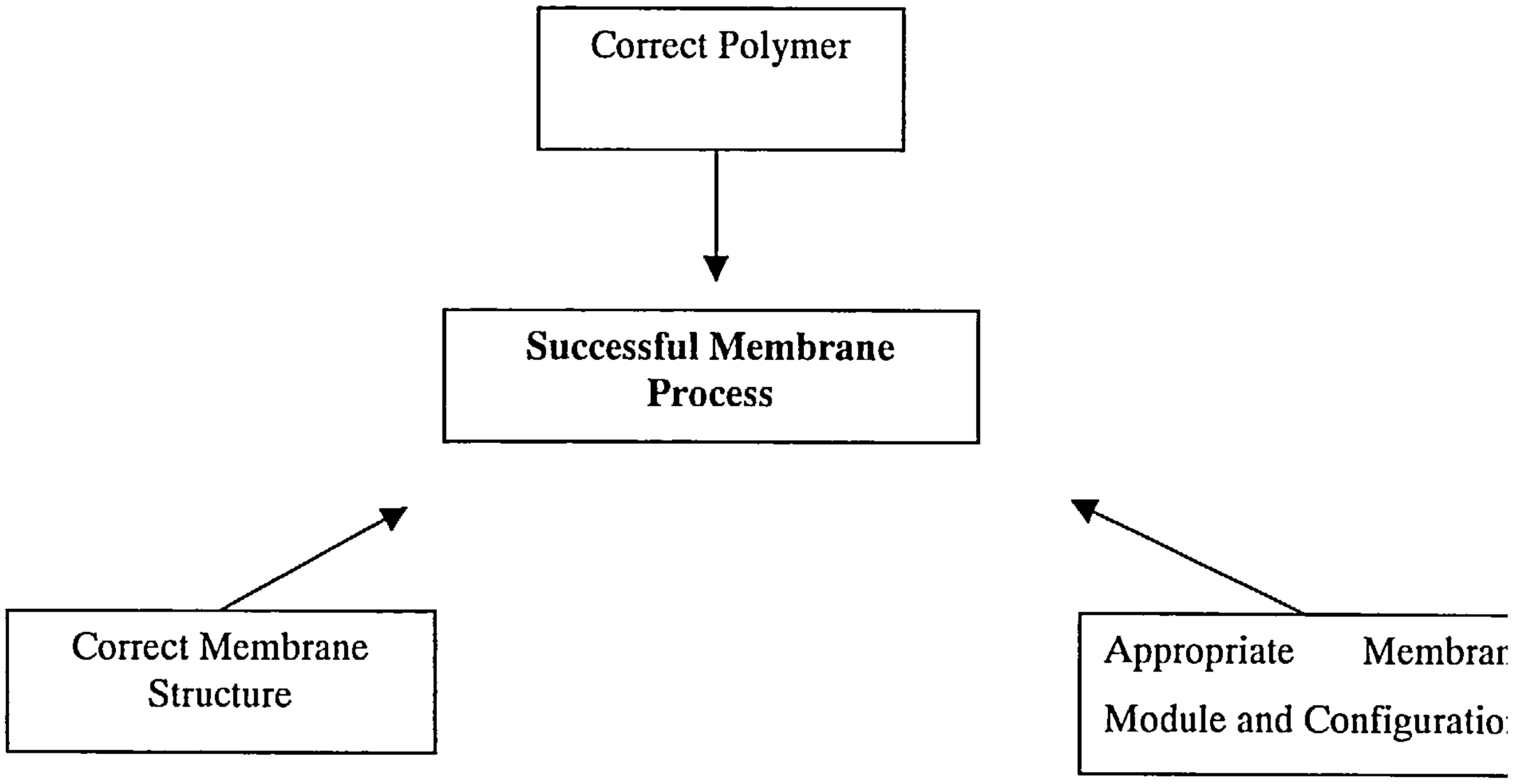

The major structural breakthroughs and fabrication developments in the production of gas separation membranes can be summarised in the Table 1.3.

Table1.3 [11] Membrane Advances

Year	Workers	Discovery	US Patent #
1964	Loeb and Sourirajan	Asymmetric membrane formation	3133132
1972	Riley	Composite membrane formation	3648845
1975	Browall and Salemme	Multilayer composite laminate	38744986
1976	Browall	Surface defect coating on laminate	3980456
1980	Henis and Tripodi	Multicomponent membranes	4230463
1984	Coptan and Burchesky	Hollow fibre composite membrane	4467001
1987	Langsam	Chemically surface treated membranes	4657564
1987	Puri	Highly permeable coatings	4968470
1988	Hayes	UV cross linked polyimide membranes	4717393
1988	Peinemann and Pinnau	In-situ multicomponent membranes	4746333
1989	Sanders, Clark, Jensvold, Beck, Lipscomb and Coanu	Internal separating layer of asymmetric membrane (POWADIR)	4772392
1989	Kesting, Fritzsche, Murphy, Handermann, Cruse and Malon	Asymmetric membranes formed from Lewis acid base complexes	4871494
1992	Exiner, Hayes and Manow	Integrally skinned asymmetric composite membranes	5085676
1992	Kusuki, Yoshinaga and Shimazaki	Integrally skinned asymmetric composite membranes	5141642

The first successful commercial gas separation process was launched by Monsanto in 1980. The Prism separator utilised coated polysulphone hollow fibre membranes. The prism separator was initially used to recover hydrogen from an ammonia purge stream [12]. It has since been used in the recovery of carbon dioxide during oil

recovery and in nitrogen production [13]. After the success of the Prism system many other companies entered the membrane gas separation market as shown in Table 1.4.

Table1.4 [11] Commercial Membrane Developments

Year	Company	Membrane/System
1980	Monsanto (Permea)	Polysulfone hollow fibre H_2, CO, CO_2 separations
1982	Separex	Cellulose triacetate flat sheet H_2, CO_2 separations
1984	Dow chemicals	Polyolelin hollow fibre Air separation
1986	Permea	Density gradient polysulphone hollow fibre Air separation
1987	Innovative membrane systems	Thin film composite hollow fibre H_2 separation
1988	Dow Chemicals	Tetrabromo bisphenol polycarbonate hollow fibre Air separation
1989	Ube	Polyamide Hollow fibre H_2 separation
1991	Delair	Polyphenylene oxide fibers Air separation

The growth of commercial membrane applications is impressive. The worldwide annual installed gas handling capacity of membrane systems stood in excess of 4000 million cubic metres in 1999 and was growing at a rate of 8% p.a. [14].

1.3 Gas Separation

Membranes separate gases using the principle of selective permeation. For a membrane gas separation system the gas is made to transfer through the membrane by applying a pressure difference across the membrane. The permeate stream is enriched in the faster permeating components and the retentate stream is enriched in the slower permeating gases.

The pressure normalised flux P is used to measure flow across membranes, it takes into account the surface area of the membrane and the driving force across the membrane. The standard units of pressure normalised flux are $cm^3(STP)/s\ cm^2$ cm Hg.

The ratio of pressure normalised fluxes for pure gases (P_i/P_j), gives the selectivity Ω^1_j of the membrane, this is a measure of how well the membrane separates the gases.

For a defect free polymer membrane the pressure normalised flux is inversely proportional to the thickness of the membrane and so is standardised with respect to thickness, $P\lambda$ (where λ is the thickness of the membrane) this gives the permeability coefficient P_c of the polymer for that gas, $P_c = P\lambda$. The permeability coefficient is a measure of the intrinsic permeability of a gas through the particular polymer. The permeability coefficient is different for different gases and so it can be seen that the selectivity for a defect free polymer membrane is simply the ratio of the permeability

coefficients, $\alpha^i_j = P_i/P_j$. The ratio of permeability coefficients α^i_j is known as the intrinsic or ideal selectivity.

1.3.1 Gas Permeation in Porous Media

Although gas separation membranes are intended to be defect free there are inevitably some defects in the active layer. This requires a knowledge of the different types of gas flow in pores.

Knudsen Diffusion

This type of flow occurs when the knudsen number (λ/r) is greater than 10.

λ, the mean free path of a gas molecule is given by

$$\lambda = \frac{R_o \cdot T}{\sqrt{2} \cdot \pi \cdot \rho \cdot N \cdot d_m^{\,2}} \qquad (1.1)$$

And r is the diameter of the pore.

The flow due to knudsen diffusion is given by

$$Q = \frac{8}{3} \cdot \left(\frac{1}{2 \cdot \pi \cdot R_0 \cdot T \cdot M} \right)^{\frac{1}{2}} \cdot \frac{r}{L} \cdot \Delta p \qquad (1.2)$$

The flow rate is seen to be dependent on the molecular weight of the gas molecule. Gases with different molecular weights therefore flow at different rates through the same pore. The selectivity for gases separated by knudsen diffusion is therefore

$$Selectivity = \sqrt{\frac{M_b}{M_a}} \qquad (1.3)$$

The low selectivities associated with knudsen diffusion therefore mean it is not a commercially viable process for gas separations. It is however used to separate Uranium isotopes [15].

Viscous Flow

When the knudsen number is less than 0.01 viscous flow dominates. The flowrate for viscous flow is given by

$$Q = \frac{r^2}{8 \cdot R_o \cdot T} \cdot \frac{1}{L\eta} \cdot \left(\frac{p_f + p_p}{2} \right) \cdot \Delta p \qquad (1.4)$$

The viscosity of a gas (η) is essentially independent of pressure. It can be shown from Kinetic theory that

$$\eta = \left(\frac{MR_oT}{\pi^3} \right)^{\frac{1}{2}} \cdot \frac{1}{Nd_m^{\,2}} \qquad (1.5)$$

Viscous flow only occurs significantly at pores of radius greater than 300Å, even at pores of 1000Å only 50% of the flow is viscous the rest is knudsen. Viscous flow exhibits no selectivity and the membranes in this study do not exhibit pores of 300Å (from electron microscope studies) so is not studied in any detail.

Molecular Sieving

Recent developments in zeolite production have given rise to increasing importance of molecular sieving [16]. This type of separation depends on the size of the molecule and therefore the pore structure must be tightly controlled. This type of pore structure is not seen in the membranes studied here.

1.3.2 Gas Permeation Through Non Porous Media

Solution Diffusion

The work of Graham is still the basis of understanding for permeation through non - porous media today. According to the solution diffusion mechanism the transport of a gas molecule occurs by solution of the gas molecule at the high pressure side, diffusion across the membrane due to the concentration gradient and the desorption of the gas molecule at the low pressure side.

Polymer chains are in a constant state of thermal agitation and the penetrant molecules migrate through the transient gaps formed by the agitation of the polymer chains.

Solution

The concentration of the gas in the polymer at the surface is described by Henrys' law:

$$C = Sp \qquad (1.6)$$

Where: C is the concentration of the penetrant

p is the partial pressure of the penetrant above the polymer

S is the Henrys' law solubility coefficient. This is specific to the polymer penetrant system.

Diffusion

The diffusion of a gas through a polymer matrix is normally described by Ficks' first law.

$$J = -D\left(\frac{\partial C}{\partial x}\right) \qquad (1.7)$$

where: J is the flux

D is the diffusion coefficient of the penetrant in the polymer.

C is the concentration of the penetrant

x is the co-ordinate direction of the permeation in the polymer matrix

Under steady state conditions equation (no 1.7) can be integrated from the high to low pressure side of the polymer matrix (denoted by h and l respectively).

$$J = D\frac{C_h - C_l}{l} \qquad (1.8)$$

where l is the thickness of the polymer matrix.

Combining 1.6 & 1.8 gives

$$J = \frac{DS}{l}(p_h - p_l) \qquad (1.9)$$

$$\text{and so } Q = \frac{PA}{l}\Delta p \qquad (1.10)$$

where: Q is the gas flowrate (standardized)

A is the membrane area

P is the permeability coefficient = DS

Δp is the pressure difference

The permeability coefficient is the most commonly used quantity to describe the gas permeation performance of a polymer. The permeability coefficient is a basic

property of the polymer/penetrant system, it is independent of the thickness of the material.

For pure gas applications the intrinsic (ideal) selectivity is the ratio of the permeabilities of the two gases i.e.

$$\alpha_{AB} = \frac{P_A}{P_B} \qquad (1.11)$$

This is known as the ideal selectivity of the polymer and is a useful fundamental parameter. At present polymers with a high selectivity exhibit low permeabilities due to the crystalline nature of the polymers. In order to produce useful membranes not only the selectivity but also the flux must be high. As can be seen from equation 1.10 in order to increase flux if the permeability coefficient is fixed the thickness of the membrane must be reduced.

The measurement of D and S are frequently required in diffusion studies. The time lag technique of Daynes [17] and Barrer [18] are most commonly used to determine these constants.

Diffusion Theory of Small Molecules in Polymer Matrices

The solution-diffusion mechanism of gas permeation is a macroscopic model. At the microscopic level however the phenomenon of gas diffusion in polymer matrices is more complex.

In order to describe the mechanisms of gas transport numerous theoretical models have been developed. The development of these models is complicated by the difference in diffusion properties of rubbery and glassy polymers. This is because glassy polymers are not in true thermodynamic equilibrium [19,20].

These models attempt to give a better understanding of gas transport mechanisms. A better understanding of gas transport leads to better designed polymers giving more permeable and selective membranes.

Diffusion Models for Rubbery Polymers

Diffusion models for rubbery polymers take two forms.

1. Molecular models
2. Free volume models

Molecular Models

Molecular models analyse the specific motion of penetrant molecules and the surrounding polymer chains relative to each other and take into account the pertinent intermolecular forces. Molecular models typically assume that fluctuating holes exist in the polymer matrix and at equilibrium a definite size distribution is established on a time average basis. A hole of sufficient size contains a dissolved penetrant molecule which can jump into a neighbouring hole once it acquires sufficient energy. Diffusion is achieved when holes which have become vacant are occupied by other penetrant molecules. Molecular models largely follow Arrhenius type behaviour of diffusion coefficients observed experimentally as below.

$$D = D_o \exp^{\left(\frac{-Eapp}{R_o T}\right)} \qquad (1.12)$$

where: E_{app} is the apparent activation energy for diffusion

D_o is a constant

R_o is the universal gas constant

T is the absolute temperature

A correlation is found between E_{app} and the molecular diameter of the penetrant but no theoretical description for the diffusion coefficient D has been made with molecular models [20].

The first molecular model for diffusion in rubbery polymers was proposed by Meares [21]. He found that the activation energy for diffusion correlates with the square of the penetrant diameter. With these findings he concluded that the diffusion step is not governed by the energy necessary to create a hole that can accommodate a penetrant molecule. He concluded that the energy required to separate polymer chains to form a cylindrical void that allows the penetrant molecule to jump from one position to another was the governing step. Meares proposed the following expression.

$$E_D = \frac{\pi}{4}\sigma^2 N\lambda(CED) \qquad (1.13)$$

where: E_D is the actual activation energy for diffusion

σ is the collision diameter of the penetrant.

N is Avogadros number.

λ is the length of the cylindrical void (and jump length)

CED is the cohesive energy density of the polymer

In a later model Brandt considered polymer structure in order to estimate the activation energy. He proposed that the activation energy consists of two parts. An

intermolecular contribution E_b due to the repulsion the bent chain experiences from its' neighbours and an intramolecular contribution E_I due to the chains resistance to bending. This model was successfully tested by studying the diffusion of gases in fluorocarbon polymers [22,23].

Another model by DiBenedetto and Paul considered a gas molecule in a void formed by four parallel polymer chains [24]. In order for the gas molecule to jump the four chains rotate into an activated state. The activation energy is the potential difference between the normal dissolved state and the activated state.

Free Volume Models

Free volume models relate mutual diffusion coefficients for a gas/polymer system to the free or empty volume of the system. The models developed for rubbery polymers are based on Cohen and Turnbulls' theory for diffusion in hard sphere liquids [25]. The free volume model was made of two contributions; 1. Vibrations in molecules that cannot be redistributed without a large energy change, 2. Discontinuous voids. Diffusion in such a liquid is not due to a thermal activation process but is as a result of a redistribution of free volume voids caused by random fluctuations in local densities [20,26].

Fujita developed a free volume model that described the strong concentration dependence of diffusion of organic vapours in some rubbery polymers [27]. This model breaks down however for small penetrant molecules whose diffusion is largely independent of their concentration [28].

Stern and Frisch extended the Fujita model to deal with the permeation of small gases and binary gas mixtures [29-33]. The extended model satisfactorily described the dependence of permeability coefficients on pressure and temperature.

Diffusion Models for Glassy Polymers

Diffusion mechanisms for gas molecules in glassy polymers are markedly different to rubbery polymers. Diffusion depends on the temperature of operation and whether or not that is above the glass transition temperature (Tg). Typically diffusion coefficients for light gases in glassy polymers are found to be highly non linear functions of the penetrant concentration. This is due to intersegmental packing defects that are frozen into the structure as the polymer is cooled through the glass transition.

Glassy polymers are not in a state of true thermodynamic equilibrium and have un-relaxed volume segments called holes or microcavities of different sizes. Glassy polymers also have very long relaxation times due to the restricted motion of the chain segments. Therefore in the presence of a penetrant the chain motion is not fast enough to homogenize the environment of the penetrant. This inhomogenity at the molecular level is believed to cause two modes of transport through the polymer and hence the "dual-mode sorption theory" [33,34].

The two modes of transport are 1. Regular Fickian diffusion through the polymer matrix. 2. Penetrant molecules are absorbed (accommodated) in irregular cavities,

these have very different intrinsic diffusional mobilities to the polymer matrix [20,35].

The Dual-Mode Sorption Model

The dual-mode sorption model is the most widely accepted phenomenonological description of the dependence of diffusion, solubility and permeability coefficient on penetrant concentration in glassy polymers. The model postulates that the gas dissolved in a glassy polymer is made up of two fractions, 1. Molecules dissolved in the polymer matrix described by Henrys' law, similar to that above Tg. 2. Molecules dissolved in a finite number of fixed pre-existing microvoids in the polymer matrix, described by Langmuir isotherms.

The second fraction is unique to glassy polymers. It is related to the abrupt change in the free volume of the polymer as the glass transition temperature is traversed, shown below in Fig. (1.3)

Fig 1.3 Free Volume against T

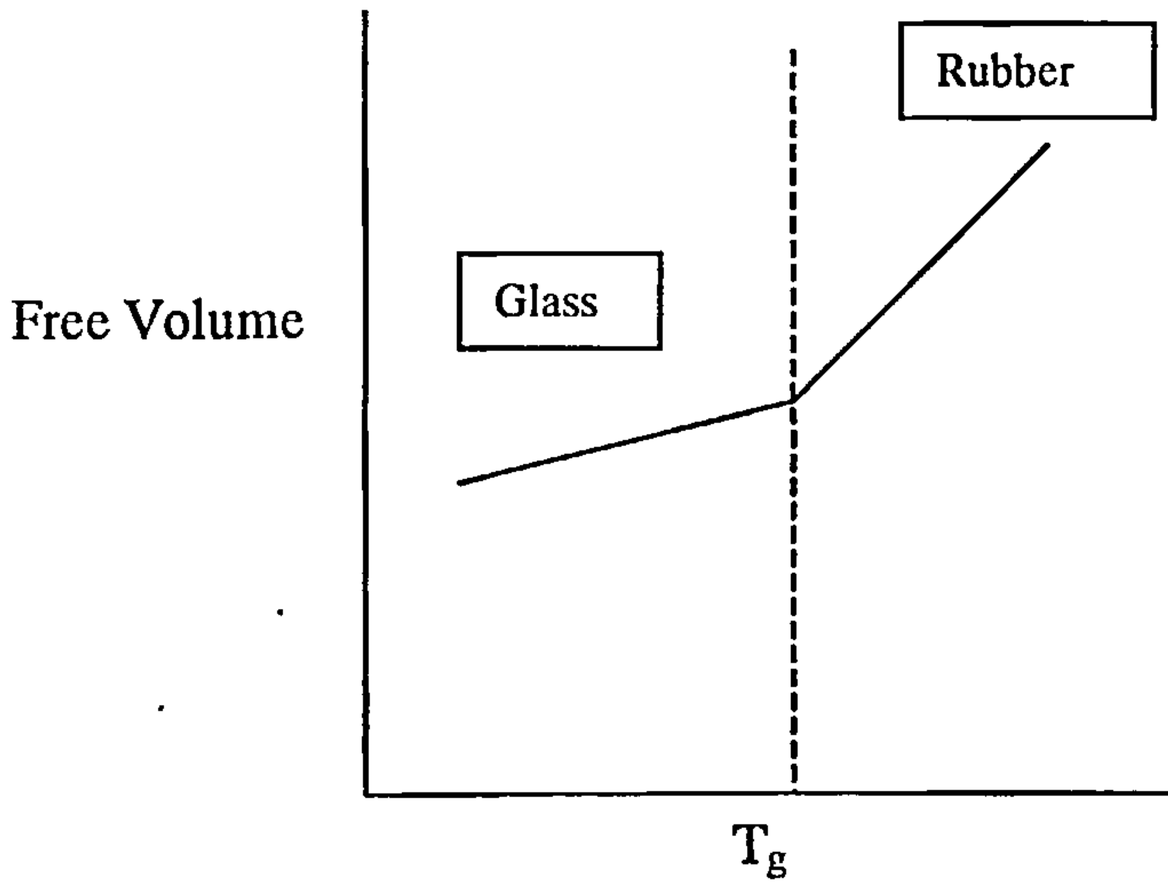

The overall solubility isotherm in the dual-mode sorption model is given by

$$C = C_D + C_H = k_D p + \frac{C'_H bp}{(1+bp)} \qquad (1.14)$$

Where: C_D is the concentration of molecules dissolved by the normal dissolution process, known as the Henrys' law Isotherm.

C_H is the concentration of molecules dissolved in microcavities known as the Langmuir Isotherm.

p is the penetrant pressure.

b is the hole affinity constant.

C'_H is the hole saturation constant, which is a measure of the sorption capacity of the unrelaxed volume.

In this early approach the penetrant molecules dissolved in the microcavities were assumed to be totally immobilised. Under these conditions the mean permeability is simply the product of the Henry's law constant and the diffusivity of the mobile fraction of the dissolved molecules,

$$P = k_D D_D. \qquad (1.15)$$

The dual-mode sorption model was extended by Koros and Paul [36-38]. They postulated that the molecules sorbed into the Langmuir mode might not be totally immobilised. They called this the partial immobilisation model and the diffusive flux is given by:

$$J = -D_D \frac{\partial C_D}{\partial x} - D_H \frac{\partial C_H}{\partial x} \qquad (1.16)$$

Where: J is the diffusive flux

D_D is the Henry's law diffusion coefficient

D_H is the Langmuir Isotherm diffusion coefficient

This model was tested with a variety of gases and gives good results [34,38-40]. The main limitation with the dual-mode sorption model is that it is not directly related to the polymer structure.

Two models have been developed that work well for both glassy and rubbery polymers. Pace and Datyner developed a detailed molecular model incorporating features of the Brandt and DiBenedetto and Paul models [41-42].

Vrentas and Duda developed a free volume model incorporating both the Cohen and Turnbull and Fujita free volume models [43]. The model also incorporated Flory's thermodynamic theory and Bueches entanglement theory.

1.3.3 Gas Mixtures

In industrial processes the purpose is to separate gases and so the feed to a membrane module is a mixture of gases. Most membrane characterisation research uses pure gases to calculate membrane properties such as permeability and selectivity. In order to simulate an industrial environment the membranes produced in this study were also characterised using gas mixtures as well as pure gases.

In order to calculate membrane properties such as permeability and selectivity the system has to be modelled according to the system conditions. A model to describe module conditions is the well mixed model. This is shown below in Fig 1.4.

Fig 1.4 A well mixed module.

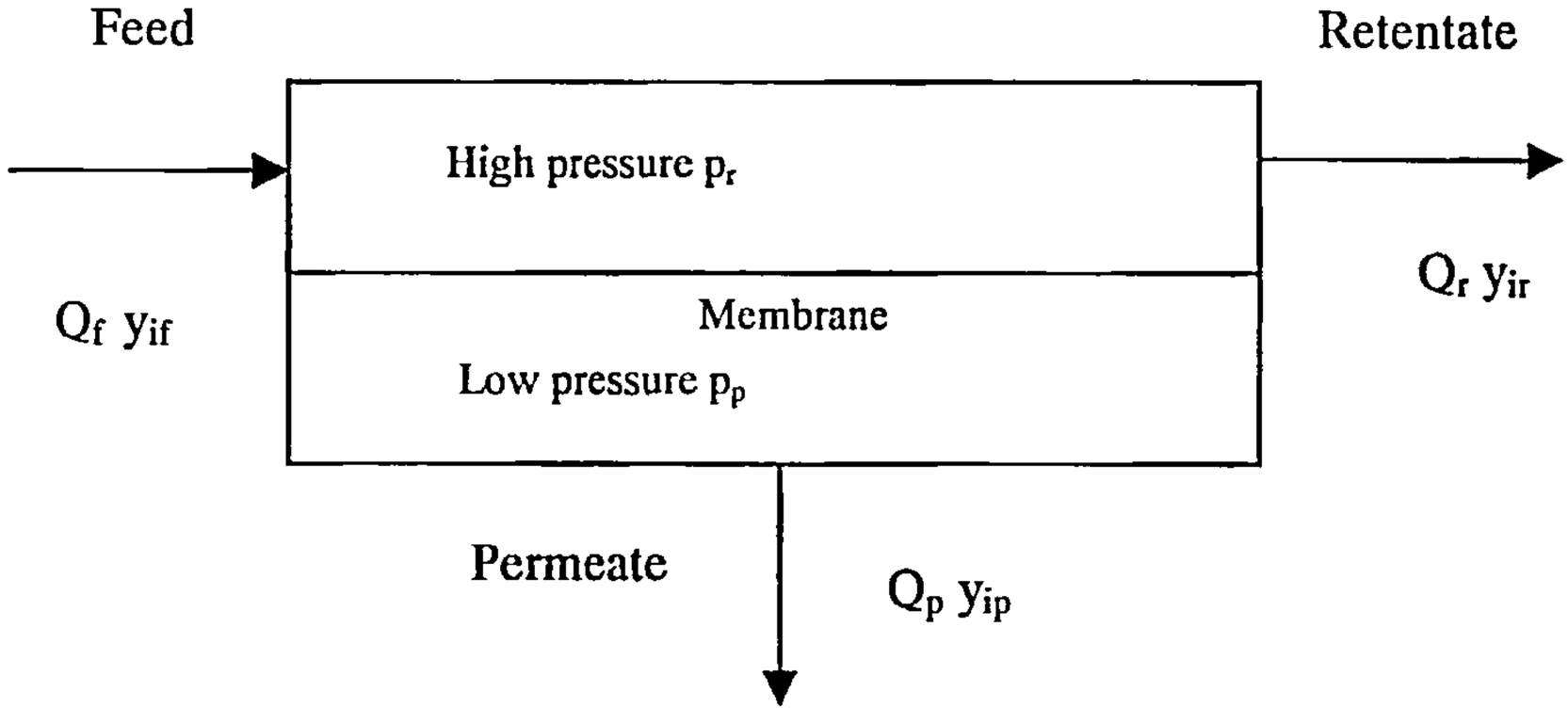

For a well mixed permeator and a binary gas mixture (i and j) it can be shown that the flows of the gases can be represented as thus.

$$Q_p y_{ip} = P_i A [y_{ir} p_r - y_{ip} p_p] \quad (1.18)$$

$$Q_p y_{jp} = P_j A [(y_{jr} p_r - y_{jr} p_p] \quad (1.19)$$

Where $P_{i/j}$ is the pressure normalised flux of component i or j and A is the membrane area.

Now $y_j = 1 - y_i$

Therefore (1.19) = $Q_p(1-y_{ip}) = P_j A [(1-y_{ir})p_r - (1-y_{ip})p_p]$

The selectivity of the membrane is the ratio of the pressure normalised fluxes of the two components.

$$\Omega = \frac{y_{ip}}{1 - y_{ip}} \left[\frac{(1 - y_{ir}) p_r - (1 - y_{ip}) p_p}{y_{ir} p_r - y_{ip} p_p} \right] \quad (1.20)$$

By altering the module operating pressures the concentration of the retentate and permeate can be varied. However the selectivity is fixed by the nature of the membrane.

1.4 Resistance Modelling

Henis and Tripodi developed their revolutionary coating technique in 1980 [7,8]. Their coating technique allowed previously useless membranes to exhibit close to the intrinsic selectivity of the polymer matrix. They rationalised their coating process in terms of resistances in series and parallel.

Fig 1.5 Resistance Model

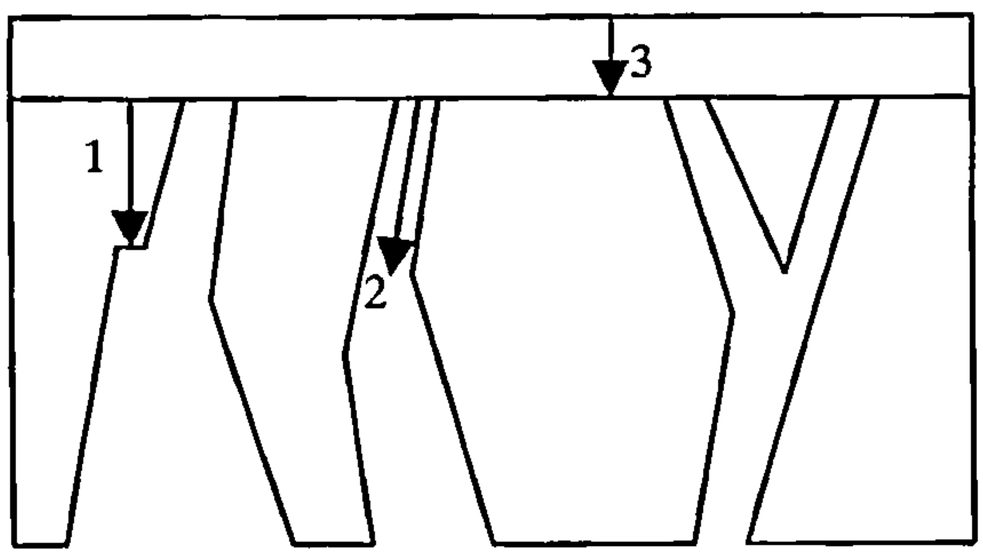

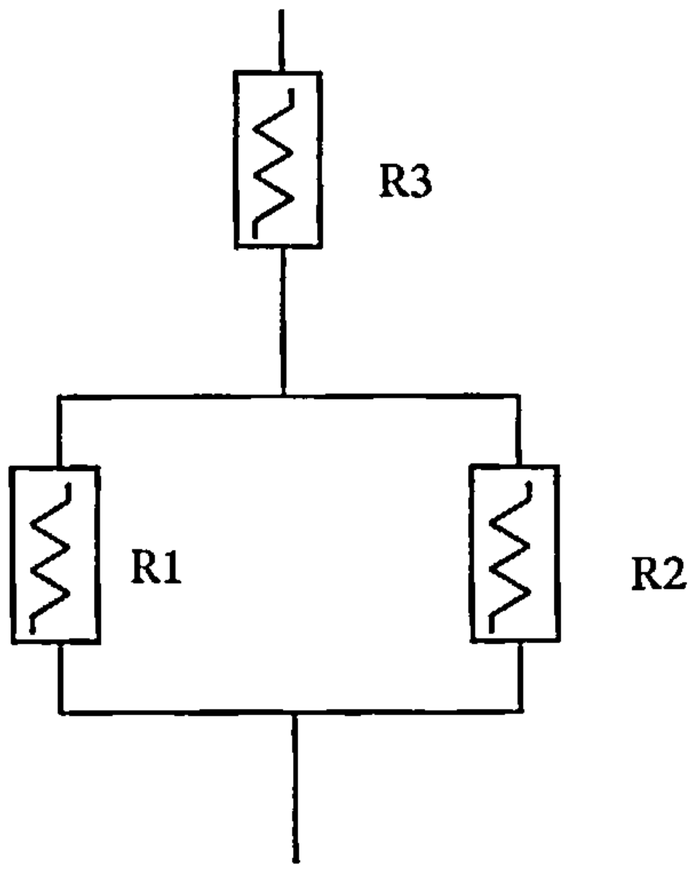

The resistance of the solid polymer is represented by R1, the resistance of the pore is represented by R2 and the resistance of the coating layer is given by R3. They made assumptions about coating thickness and the depth the coating penetrates into pores and applied their model to typical membrane structures.

Fouda et al exposed limitations in the Henis and Tripodi model when fitting actual permeation data to possible membrane structures [44]. They developed a Wheatstone bridge resistance model which gave better results. The model took into account the resistance of cross flow between the parallel and vertical flows.

Fig 1.6 Wheatstone Bridge Resistance Model

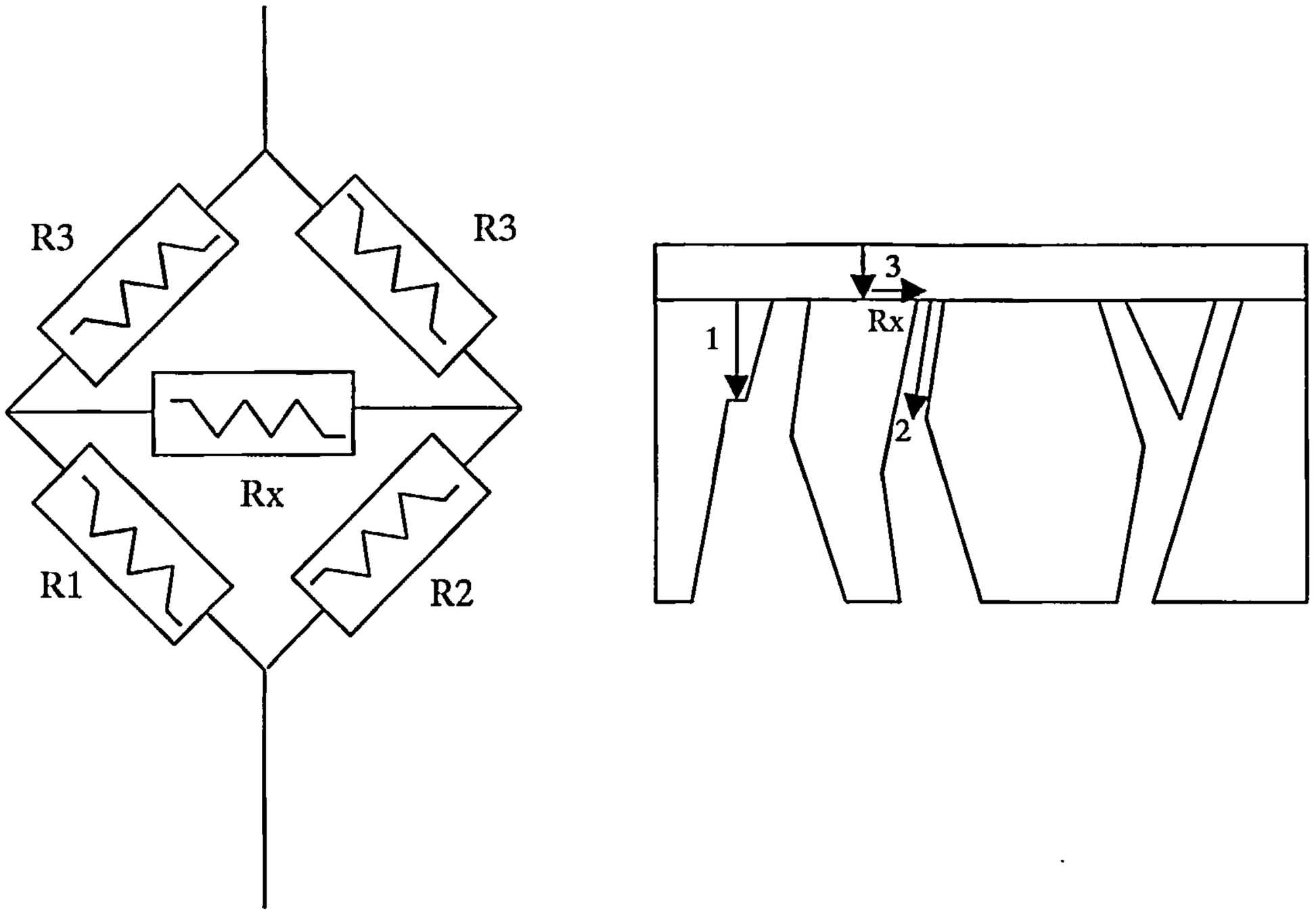

Shilton et al then developed the Fouda model to deduce the structural details of gas separation membranes [45]. The model took into account a distribution of pore size and depth of pore penetration for the coating material.

A resistance model is built up from the different types of flow present in membranes. The total flow is built up from contributions from flow due to solution diffusion, knudsen diffusion and viscous flow. The amount of flow from each regime depends on the size and surface area of pores and the thickness of the membrane active layer. By using different gases and studying coated and uncoated membranes a model can be built which predicts size and distribution of pores and the thickness of the active layer. Models of this type are multi-parameter fit exercises and in the past have proved unwieldy [9].

A simple resistance model to describe membrane characteristics uses uncoated data to calculate the thickness of the active layer and surface porosity. The model uses the two types of flow seen in the uncoated membranes, Knudsen diffusion and solution diffusion. The model is illustrated in Fig 1.7.

Fig 1.7 Uncoated resistance model.

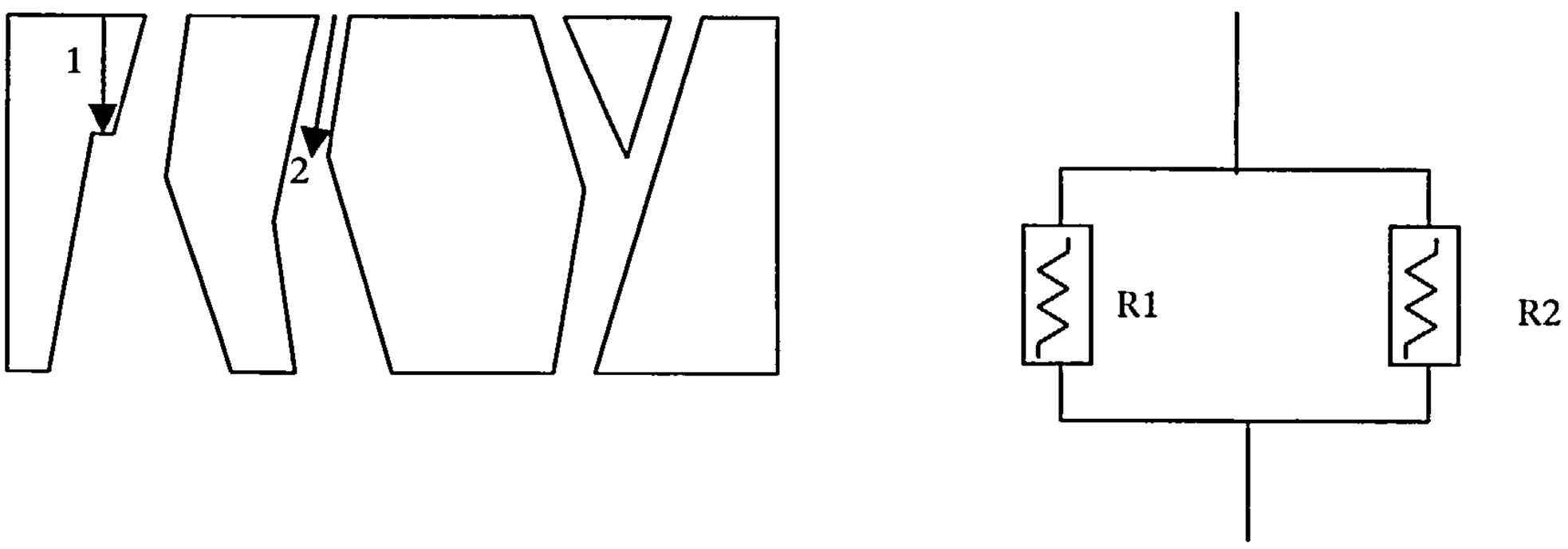

The two flows through the membrane are described by the following equations.

$$Q = \frac{\overline{P}}{\lambda} A \Delta p \qquad \text{Flow 1 (Solution Diffusion)}$$

$$Q = \frac{8}{3}\left(\frac{1}{2\pi R_o TM}\right)^{\frac{1}{2}} \frac{r}{\lambda} A_p A \Delta p \qquad \text{Flow 2 (Knudsen Diffusion)}$$

The total flow = Flow 1 + Flow 2

Flow 1 is the flow through the solid polymer and flow 2 is the flow through the pores in the active layer. The Flow through both the solid polymer and pores is different for different gases due to the different intrinsic permeabilities and molecular weights. By studying different gases and solving the model the active layer thickness and surface porosity can be calculated.

1.5 Phase Separation

Most commercial polymer membranes and the ones in this study are made by phase separation [46]. Phase separation occurs when a stable polymer solution splits into two distinct phases due to a change in the thermodynamics of the system. These two phases are described as the polymer rich and polymer poor phases. Once the polymer rich phase solidifies this gives the membrane structure. By controlling the nature of the phase separation the final structure of the membrane can be controlled. Van de Wittes' review paper studies the different types of phase separation in relation to membrane formation [47]. This means phase separation can be used to produce membranes for as diverse purposes as gas separation and micro filtration. There are many types of phase separation used in the production of membranes and these are described below.

Precipitation by solvent evaporation

This is the most simple technique for fabricating membranes. The polymer is dissolved in a solvent to form a solution. The solvent is then allowed to evaporate in an inert atmosphere.

Precipitation from the vapour phase

A cast film of a polymer/solvent solution is placed in an inert atmosphere of non-solvent saturated with solvent vapour. The solvent in the vapour phase prevents evaporation of the solvent from the film. Precipitation occurs as the non-solvent in the vapour diffuses into the polymer solution.

Precipitation by controlled evaporation

In this case a three component solution is prepared (polymer, solvent and non-solvent). The solvent is allowed to evaporate and the solution phase separates.

Thermal inversion phase separation (T.I.P.S.)

A polymer solution is prepared at an elevated temperature. As the solution is cooled it becomes unstable and phase separates.

Immersion Precipitation

Most commercial membranes are prepared in this way. A polymer solution is immersed in a bath of non-solvent. Precipitation is as a result of solvent/non-solvent exchange.

The two types of phase separation used in this work are evaporation and immersion so these will be studied in more depth. For a greater understanding of the other types of phases separation the reader is encouraged to consult Mulder [48].

1.5.1 Thermodynamics

The basic principle of phase separation is that a stable polymer solution is made unstable and so de-mixes into two phases. This is all due to the thermodynamics of the system so a basic understanding of polymer solution theory is given here.

The basic parameter describing the miscibility of a system is the Gibbs free energy of mixing (ΔG_m).

$$\Delta G_m = \Delta H_m - T\Delta S_m \qquad (1.21)$$

Where: ΔH_m is the enthalpy of mixing

ΔS_m is the entropy of mixing

The components will mix freely if ΔG_m is negative. A closed system reaches equilibrium at a given pressure and temperature when the free enthalpy is at a minimum. When two components are mixed with each other the free enthalpy of mixing is determined by the partial free enthalpies (the chemical potential, μ) of both components. The chemical potential of a component i is defined as

$$\mu_i = \left(\frac{\partial G}{\partial n_i}\right)_{P,T,n_j,n_k,\ldots} \qquad (1.22)$$

Where: μ_i is the change in the free enthalpy of a system containing n_i moles when the pressure, temperature and number of moles of all other components are held constant.

Because of their large size the entropy of mixing for polymers is small, this is explained by Flory-Huggins theory [49]. This can also be seen in Fig 1.8 below.

Fig 1.8 Polymer Mixing Entropy

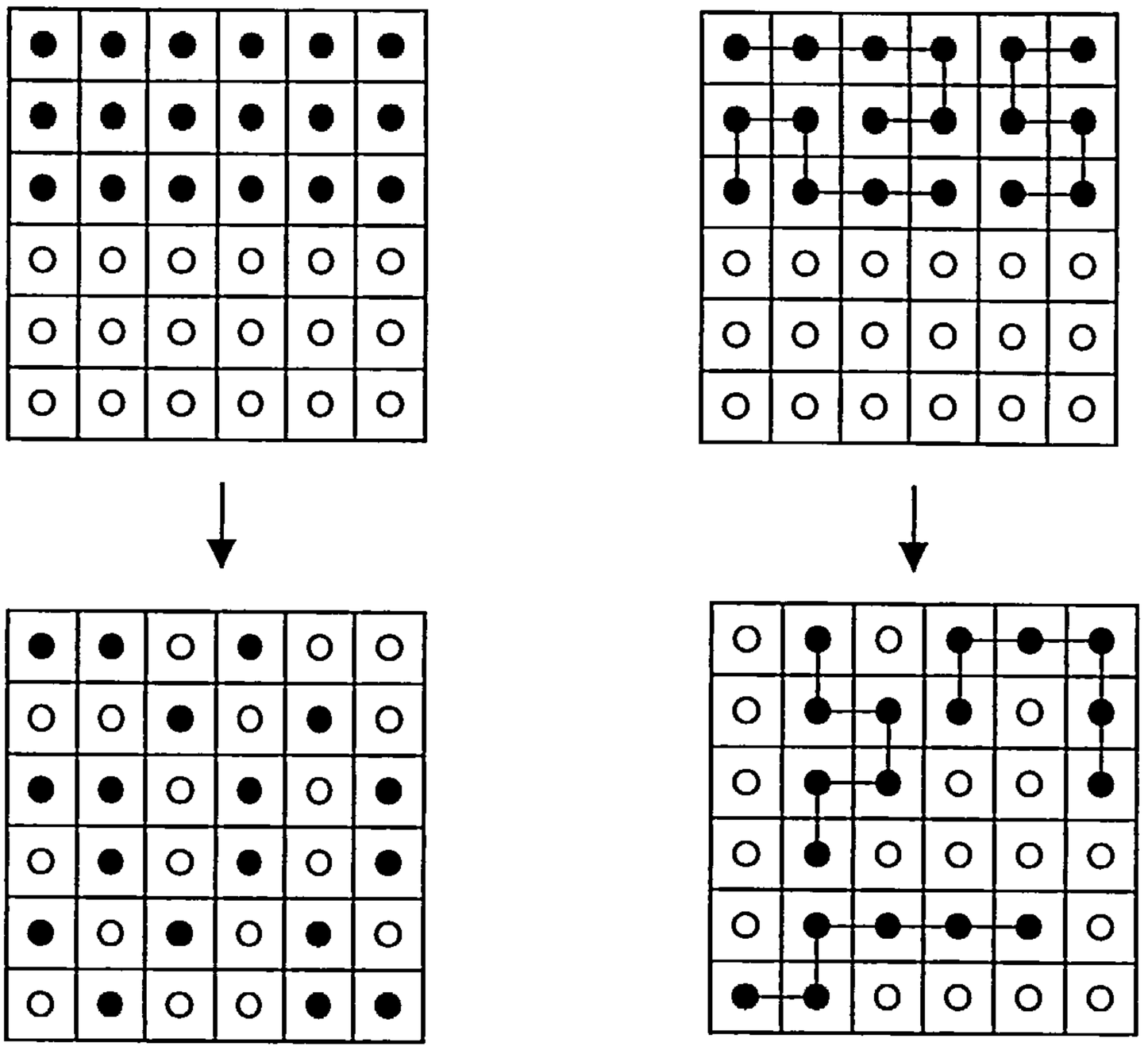

Because the entropy of mixing is small for a polymer solution this means only a slightly positive enthalpy of mixing ($\Delta H_m > 0$) is required to give a positive Gibbs free energy of mixing and so demixing. This change in the enthalpy of mixing is caused by the ingress of non-solvent in the case of immersion precipitation or the loss of solvent in the case of evaporation precipitation.

De-mixing Processes

There are two types of de-mixing observed in phase separation, these are delayed and instantaneous de-mixing [48,50]. The type of de-mixing that takes place depends on the thermodynamic stability and composition of the initial solution. This is best explained by first considering a binary system. Figure 1.9 gives a plot of ΔG_m against composition (Φ) and the first and second derivatives of ΔG_m against Φ.

Fig 1.9 Gibbs Free Energy Curves

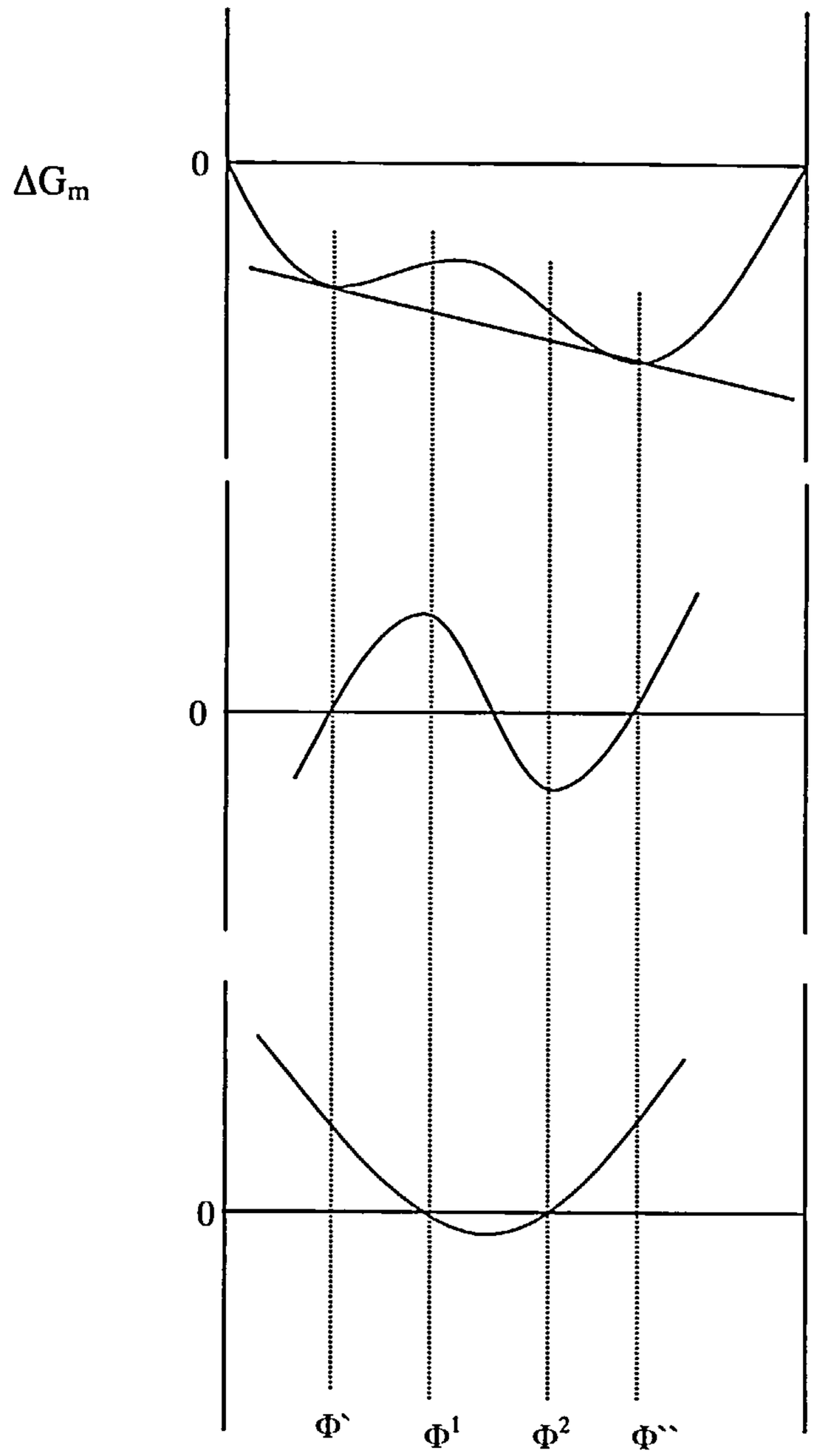

A solution with composition in the interval $\Phi` < \Phi < \Phi``$ can decrease its free energy of mixing by de-mixing into two phases of composition $\Phi`$ and $\Phi``$. These two phases are in equilibrium with each other.

If the second derivative of ΔG_m against Φ is considered (or $\frac{\partial \mu_i}{\partial \phi_i}$) it can be seen that between Φ^1 and Φ^2 $\frac{\partial \mu_i}{\partial \phi_i}<0$. This implies that the solution is thermodynamically unstable and will de-mix spontaneously. Random fluctuations in the composition increase in amplitude as time increases and after some time the solution de-mixes into small interconnected regions of composition $\Phi`$ and $\Phi``$. This mechanism is called Spinodal (or instantaneous) de-mixing and was first observed by Cahn [51]. The de-mixing process is illustrated by Fig 1.10.

Fig 1.10 Spinodal Composition vs. Time

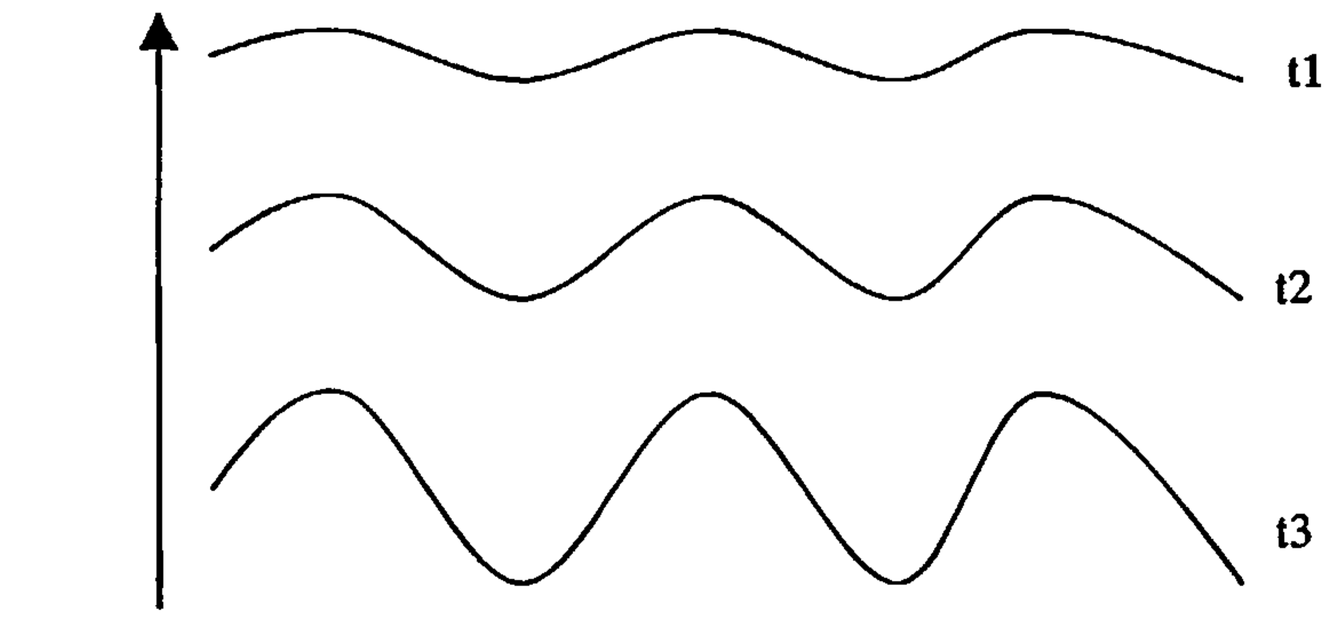

This type of de-mixing gives an open bicontinuous structure when the polymer solidifies. This type of structure is generally not useful for gas separation membranes as there is no defect free skin formed to give the separating layer. The open structure is however a useful substructure for membranes as the open structure offers no resistance to flow.

If the second derivative is considered again, the compositions over the intervals $\Phi` < \Phi < \Phi^1$ and $\Phi^2 < \Phi < \Phi``$ are positive i.e. $\frac{\partial \mu_i}{\partial \phi_i} > 0$. This means there is no driving force for spontaneous de-mixing and the two phases separate by nucleation and growth. Whether it is the polymer poor or rich phase that is the continuous phase depends on the initial composition of the polymer solution.

If the polymer poor phase grows by nucleation and growth then the final structure will be a sponge. The holes in the sponge are left when the polymer has solidified and the polymer poor phase has drained away.

If the polymer rich phase is the minor phase then the final structure is that of a latex. This structure is too weak to withstand the pressures required for commercial gas separation and unless the structure is modified does not have a non-porous skin.

1.5.2 Ternary Systems

Most membranes formed by immersion or evaporation phase separation are formed from a three component system. The three components are polymer, solvent and non-solvent. The solubility behaviour of the system is described using a ternary diagram. Ternary diagrams are also useful to describe the process undertaken during membrane production.

Fig 1.11 Ternary diagram

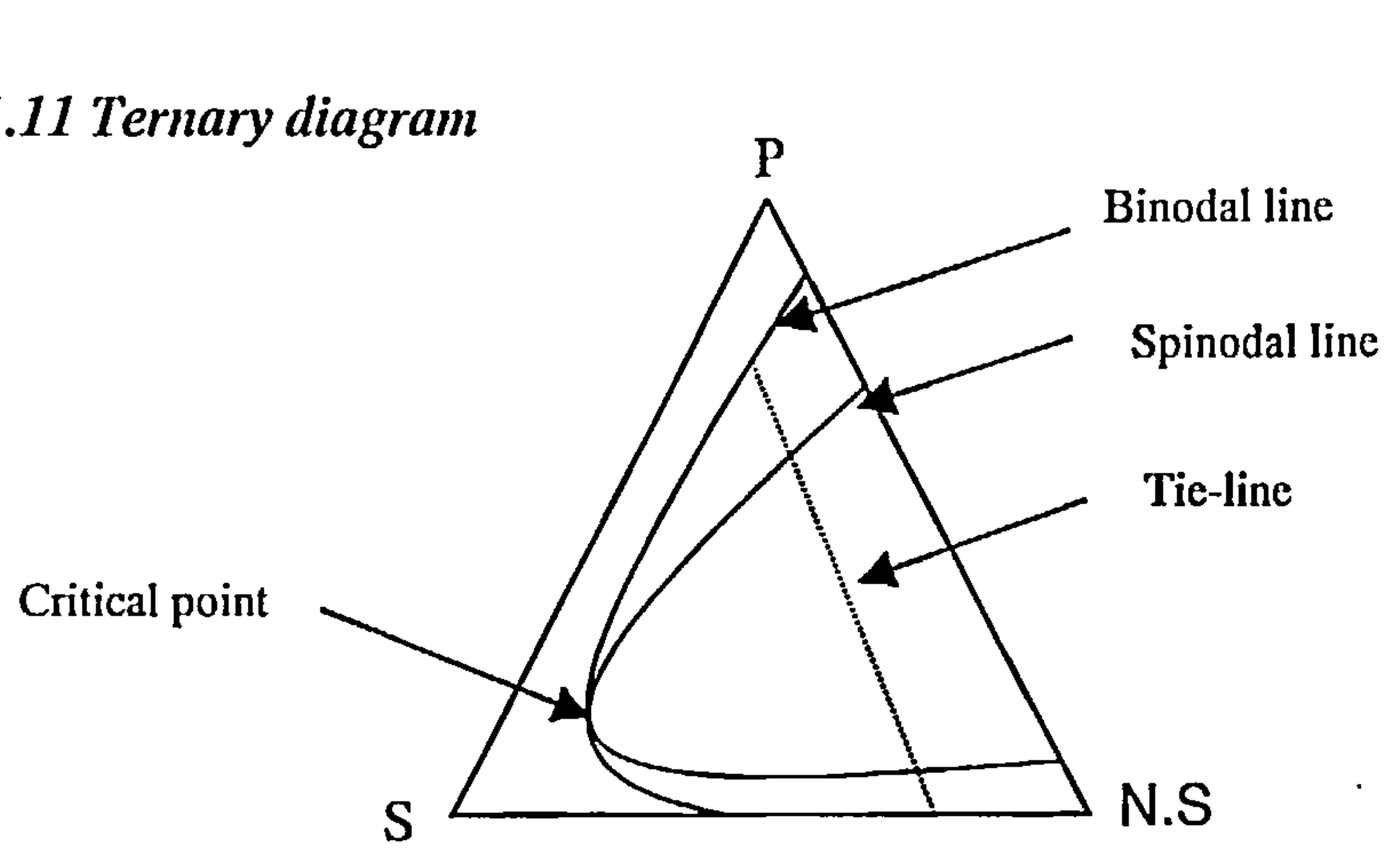

The three corners of the diagram represent the pure components. Ternary diagrams can be prepared by titration or by light scattering experiments [52-55]. Wolf and Barth recently developed a technique to quickly form phase diagrams using a combination of experimental techniques and theoretical calculations [56]. They calculated interaction parameters using Headspace-Gas Chromatography, light scattering and swelling experiments. The calculated phase diagrams were very similar to those obtained by experiment.

Any point within the triangle represents a mixture of the three components. The binodal and spinodal lines are shown as well as tie lines and the critical point. If the composition of the system lies within the binodal then separation takes place by nucleation and growth, if the composition lies within the spinodal then separation takes place instantaneously. The composition of the two phases after separation is calculated using the tie lines and a simple mass balance.

If the composition of the solution lies above the critical point in the binodal area then phase separation proceeds by nucleation and growth of the polymer poor phase and vice versa.

In some polymer systems the ternary diagram also has an area where the polymer exhibits glass properties, this is shown on Fig 1.12.

Fig 1.12 Ternary Diagram with glass region

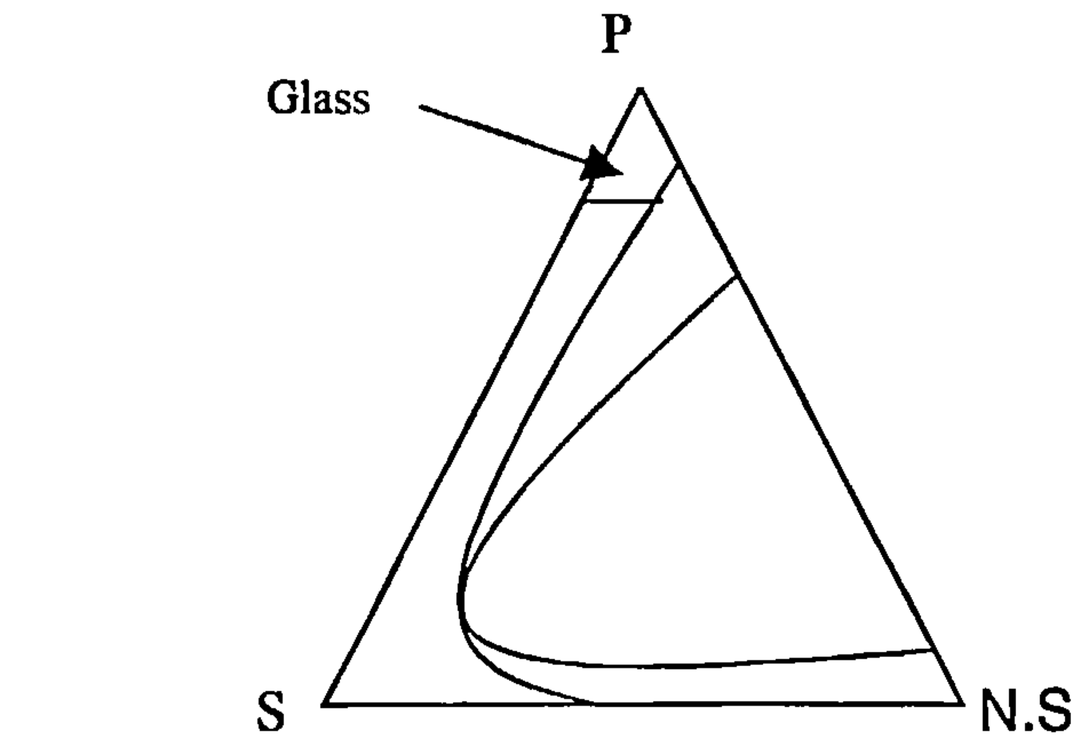

The processes of immersion and evaporation precipitation can both be illustrated on a ternary diagram.

In immersion phase separation the polymer/solvent ratio stays constant however both the polymer/non-solvent and solvent/non-solvent ratios decrease as the membrane forming system is immersed in non-solvent. This is shown by the dotted line on the ternary diagram of Fig 1.13. As the amount of non-solvent is increased first the binodal and if enough non-solvent is present the spinodal lines are crossed and the system phase separates.

Fig 1.13 Ternary diagram showing Immersion Pathway

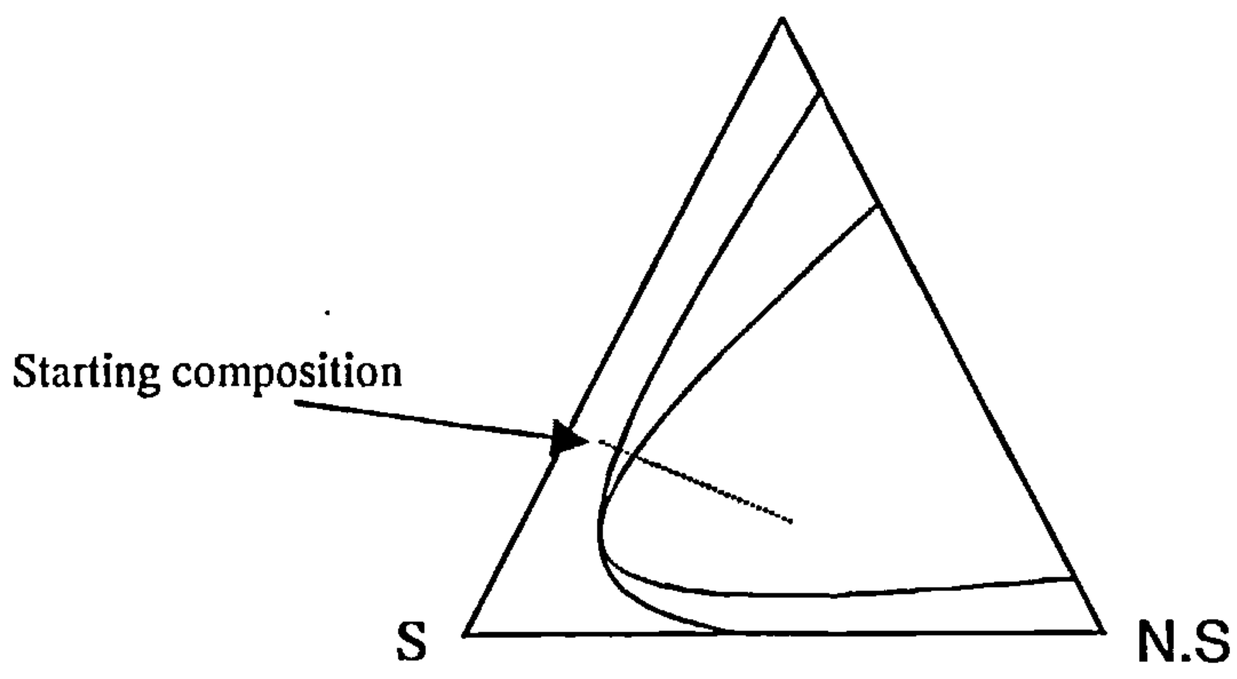

In the case of evaporation phase separation the polymer/non-solvent ratio stays constant but the polymer/solvent and non-solvent/solvent ratio both increase as the solvent evaporates. This is shown by the dotted line on the ternary diagram Fig 1.14. As the amount of solvent decreases the binodal line is crossed and if more solvent evaporates then the spinodal line is crossed.

Fig 1.14 Ternary diagram showing Evaporation pathway

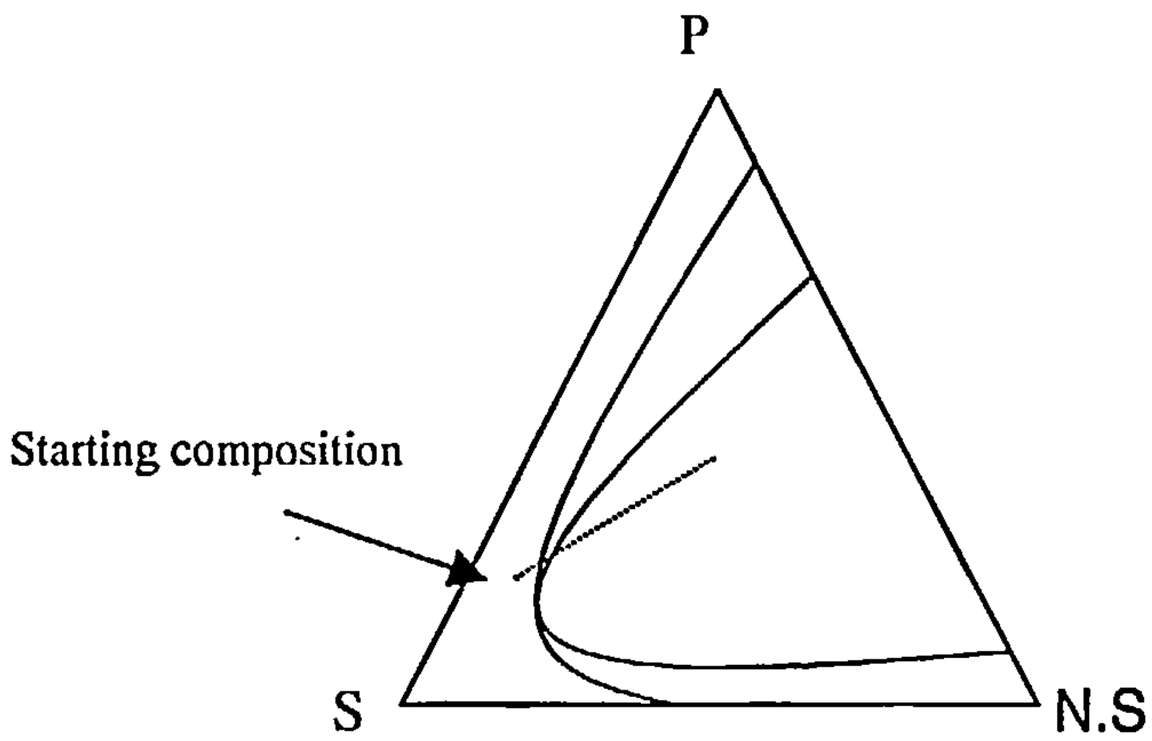

1.5.3 Membrane Structure

When a membrane is formed by phase inversion the final structure formed depends on a variety of factors. The thermodynamics of the initial system, the kinetics of the phase separation and the physical production method all affect the final structure and are all interrelated.

One consideration when making a polymer membrane is the polymer content of the final membrane. The polymer content greatly affects the strength of the final

membrane and also the structure of the membrane. The structure of the membrane in turn affects the transport and separation characteristics of the membrane.

In order to change the polymer content of the final membrane a variety of approaches can be used. The initial polymer solution could be altered or the production method could be changed.

If the initial polymer solution is changed then the thermodynamics of the system change, affecting the phase separation (possibly changing from delayed to instantaneous demixing). If the polymer solution is changed then the physical properties of the solution like viscosity and density also change. This affects the kinetics of the system and so the speed of phase separation and coagulation change and this in turn affects the final structure.

Kinetics

Phase inversion kinetics are also involved in membrane formation. Thermodynamics will give the beginning and end point of a system but will not describe the speed at which the system changes between the two states. The kinetics of a system will describe how the system changes and this is also very important in membrane formation [57].

The kinetics of a membrane forming system depend on the interactions between all the components of the system and the physical properties of the system. The affinity between the polymer and solvents, the solvents and coagulants (non-solvents) and

polymer and coagulants will affect the final structure of the membrane [58]. When designing a membrane forming system the interactions in the polymer dope, the air gap and in the coagulation bath must all be considered in order to produce the desired structure [59].

As can be seen in Fig 1.15 below, the final membrane structure depends on a variety of factors and these are all interrelated. The versatility of the phase separation system means that membranes of vastly different structures can be made using the same technique and also that the same membrane structure can be made using different techniques.

Fig 1.15 Membrane Production Factors

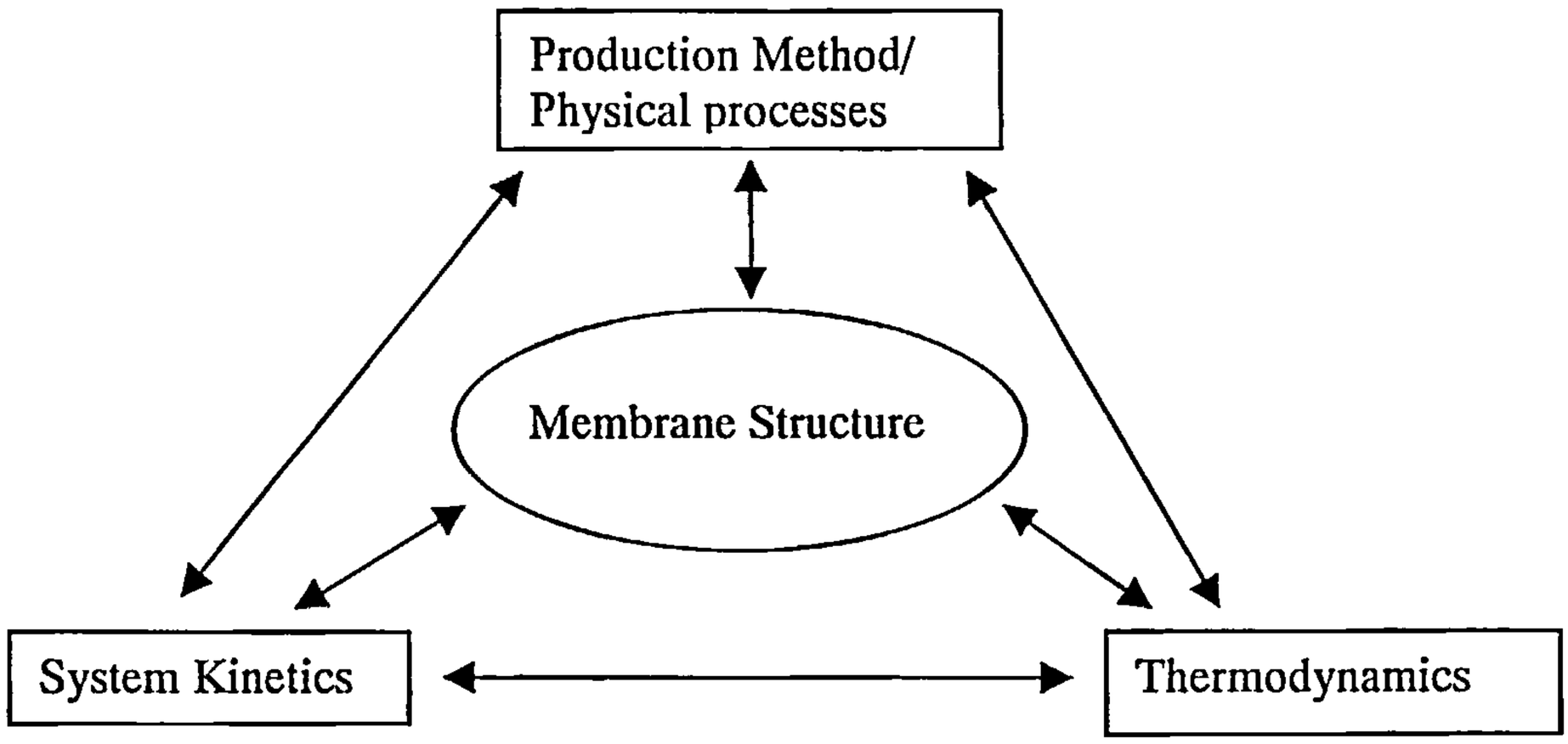

Analysis of how the final membrane structure is related to kinetics, thermodynamics and production processes has been undertaken [48]. In the next chapter the production of gas separation membranes is described and the rationale behind the structures formed is explained.

The ideal membrane structure for gas separation is asymmetric as shown in Fig 1.16. The substructure should give the membrane its strength but offer little resistance to the transmission of gas. The top active layer (skin) should be defect free to provide the separating barrier, this should be as thin as possible in order to produce as high a flux as possible.

Fig 1.16 Asymmetric membrane structure.

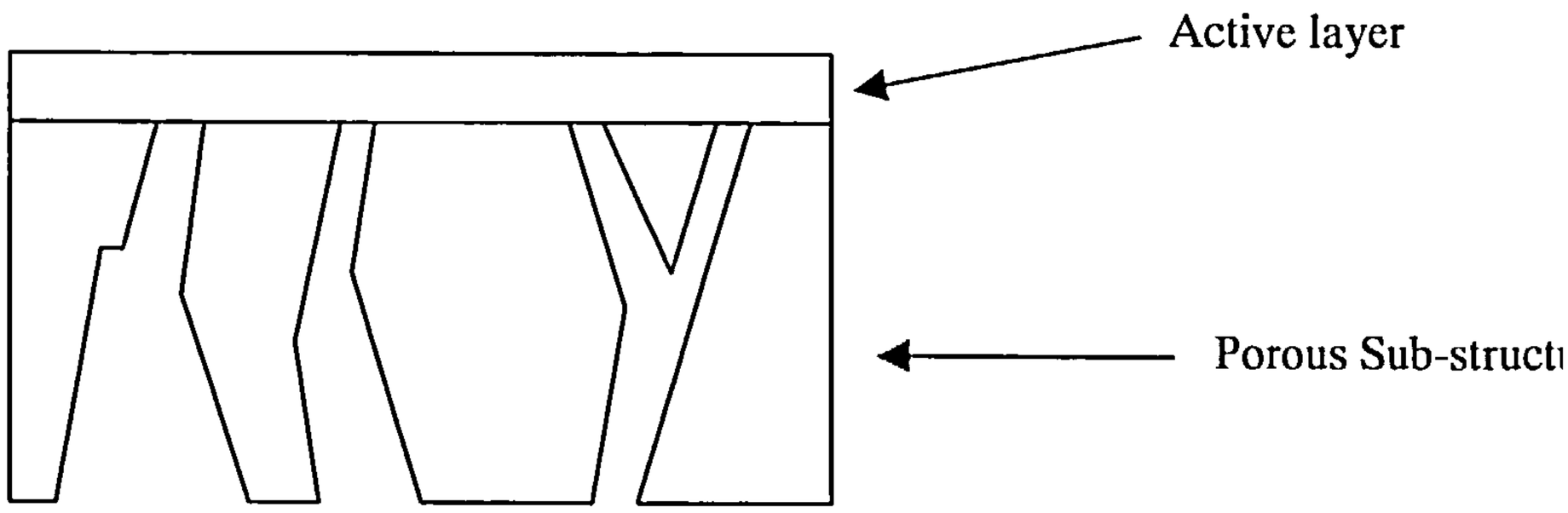

1.6 Production of Gas Separation Membranes

The membranes produced in this study and most membranes produced for gas separation are hollow fibres so this section will concentrate on hollow fibre production.

Hollow fibres are used for gas separation membranes because they are self-supporting and give the highest surface area per unit volume of any membrane type. Hollow fibres are formed by phase separation from the inside and outside simultaneously.

1.6.1 Hollow fibre spinning

Spinning hollow fibres involves the extrusion of a polymer solution or melt through an annular spinneret. The principles are very similar to those of producing textile fibres [60]. There are four main steps involved: solution formulation, extrusion, coagulation and post treatment.

A number of processing parameters affect the final structure of the membrane and these have to be taken into account when designing a membrane production process. The main processing parameters are the selection of coagulants, extrusion shear, jet stretch ratio and draw ratio. All have to be optimised in the production of hollow fibre membranes.

As well as processing parameters the polymer solution has to be optimised and spinnable and the phase separation has to be optimised to produce the correct membrane structure. This involves studying the thermodynamics of the phase separation process and selecting the appropriate coagulants (internal and external) and solvents so that they all interact to give the desired membrane structure. The solution must also have chemical and thermal stability under spinning conditions and be able to yield a continuous filament. Therefore a knowledge of the rheological properties of the solution are required as well.

The major types of spinning techniques used in the commercial production of hollow fibre membranes for gas separation can be summarised below.

Fig 1.17 Fibre spinning techniques

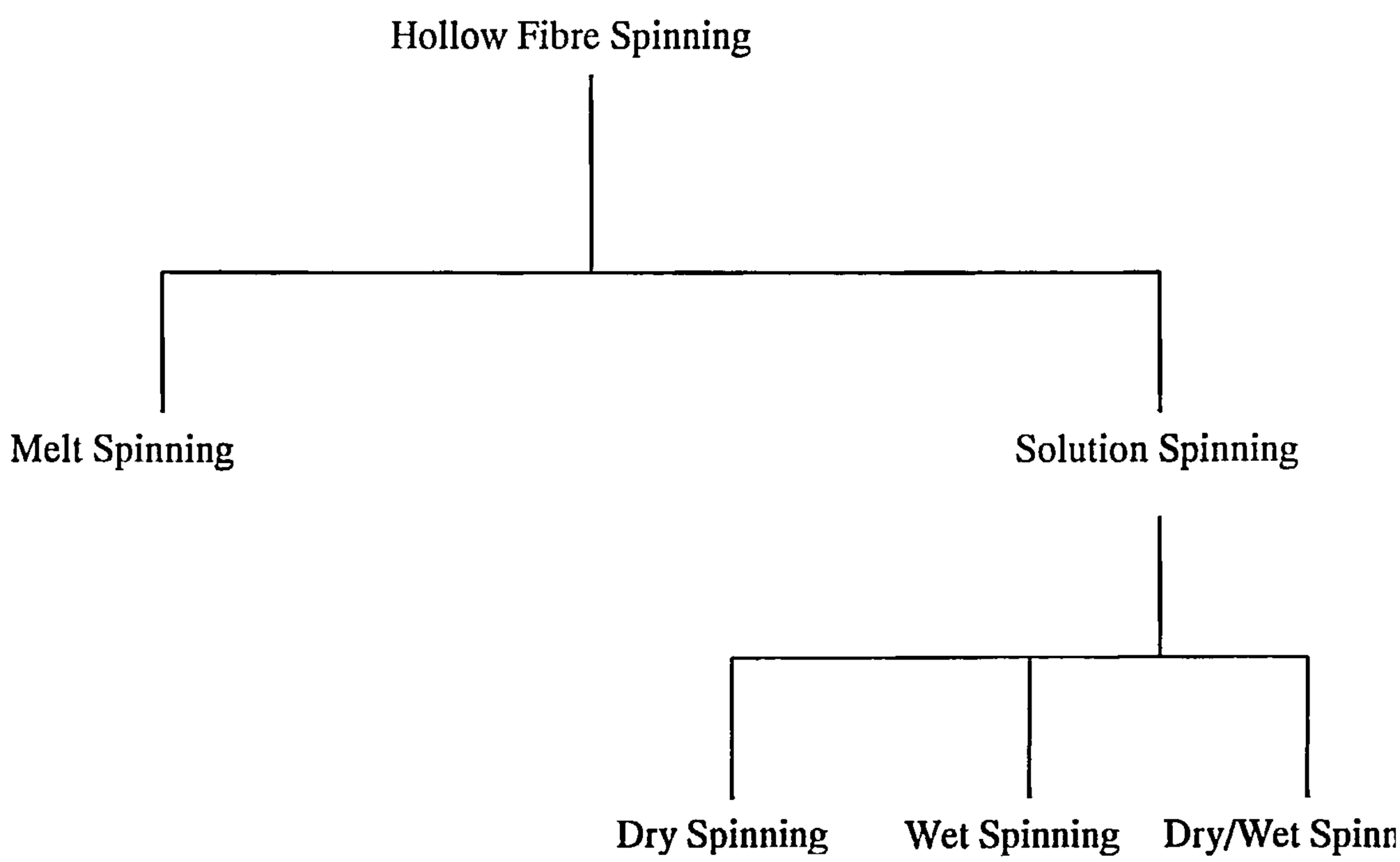

1. Melt Spinning

In melt spinning a molten polymer is extruded through a spinneret and the fibre is formed by cooling the filament in either a liquid or a gas. Dow Chemicals produce asymmetric 4-methyl-1-pentene (TPX) hollow fibre membranes for air separation in this way. They are produced under the trade name Generon [61].

2. Solution Spinning

Solution spinning processes are based on the phase separation technique. The fibres produced can be dense, asymmetric or porous depending on the production conditions. The two most commonly used types of spinning are wet and dry/wet spinning. Dry spinning is rarely used to produce commercial membranes.

Wet Spinning

In wet spinning the polymer solution is extruded directly into a coagulation bath. The speed of phase separation depends on the composition of the bath and polymer solution. If the polymer solution phase separates immediately then the resulting structure is micro-porous or if spun from a high polymer concentration solution is dense. Neither of these structures are suitable for gas separation.

The Wet Spinning process was modified by Van't Hoff et al to produce a structure suitable for gas separation [62]. They developed a "dual-bath" method for wet spinning. The first bath contains a weak non-solvent that causes delayed phase separation, this forms a thin non-porous skin layer. The second bath contains a strong

non-solvent that causes spinodal de-mixing in the remaining membrane structure and so gives an open substructure.

Wienk et al then developed the dual-bath method to spin fibres from a triple orifice spinneret [63]. The third orifice of the spinneret extrudes a coagulant so the polymer solution is sandwiched between two coagulants even though the spinneret is not submerged. This allows for better control of contact time with the first (weak) non-solvent. The fibres produced using this method had a very thin (0.3 μm) skin layer and displayed higher than intrinsic selectivities.

Dry/Wet Spinning

This is the production method used for the fibres produced in this study so is studied in some detail here.

Dry/wet spinning is a combination of evaporation and immersion precipitation. The extruded fibre first passes through an air gap before it passes into a coagulation bath. The air gap is responsible for the formation of a thin dense skin on the outside of the fibre and the bulk of the fibre structure is formed in the coagulation bath [64-67].

The fibre undergoes evaporation phase separation in the dry gap as solvent evaporates. Pinnau and Koros were the first to incorporate a forced convection stage into their membrane production process [64,65]. The membranes formed had a skin thickness of approximately 200Å. They proposed that the aggressive nature of the evaporation step brought the composition of the outer layer of the fibre into a state of

spinodal decomposition, they concluded this because of the turbidity of the fibre in the air gap. However a spinodal outer layer should result in a micro-porous skin and they reported a defect free skin on their membranes. They proposed that another physical process was taking place in the air gap to form the defect free skin [69]. They suggested that capillary pressures resulting from the gas/liquid interface in the polymer poor regions at the membrane surface caused the polymer rich regions to coalesce. This theory was developed from work on latexes by Brown [70].

Brown studied the drying of latexes to produce non-porous films. He observed that the top layer of a latex fused together under capillary pressure. He estimated the capillary pressure using the Young-Laplace equation for perfect wetting conditions (contact angle = 0)

$P_c = 2\gamma/r$

Where: P_c is the capillary pressure

γ is the surface tension of the interstitial fluid

r is the effective radius of the throat in a plane passing through the centres of three adjacent spherical nodules.

Fig 1.18 Capillary forces in nodule coalescence

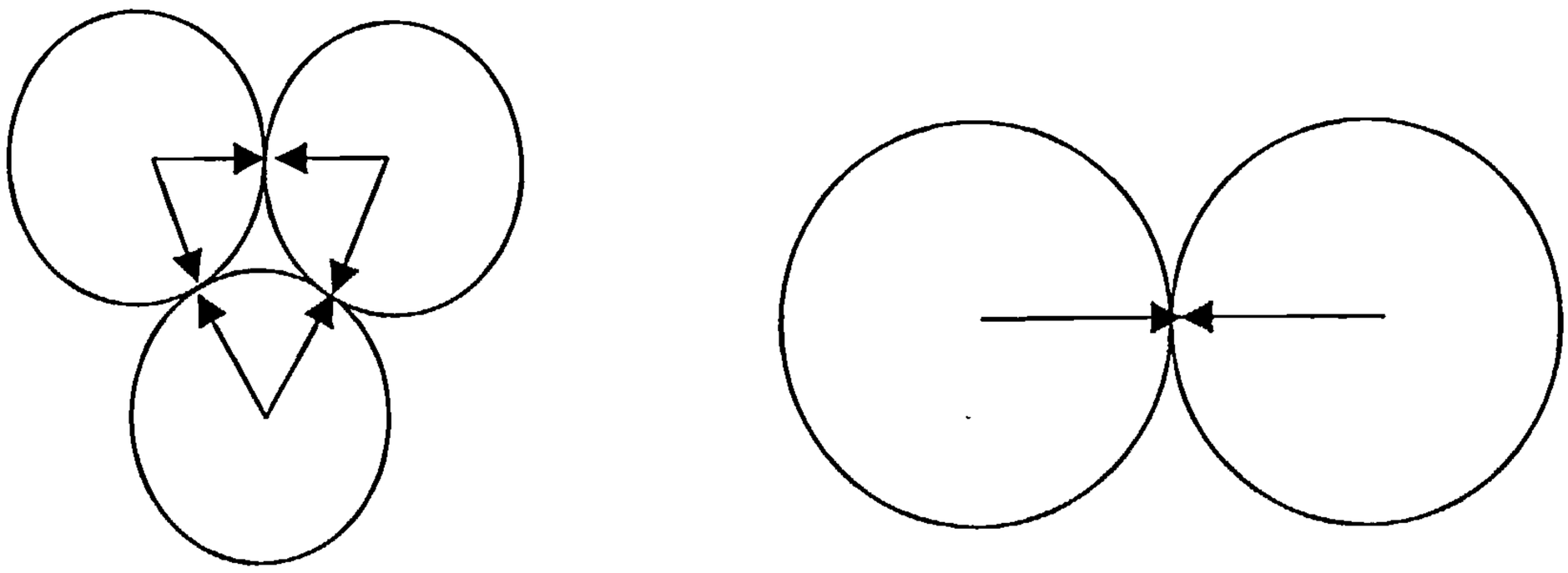

Wienk et al described a mechanism for the formation of nodules in the top layer of an ultrafiltration membrane. They concluded that the nodules were formed as a result of fast phase separation [71]. They proposed that the nodule formation was due to spinodal de-mixing and then rapid vitrification. Han and Bhattacharya also related nodule formation to spinodal de-mixing [72].

In order for the nodules to coalesce the capillary pressure must be greater than the shear modulus, G, of the polymer nodules. Pinnau and Koros proposed that:

$$G<35\gamma/R$$

Where: R is the radius of the polymer nodules

If the composition of the polymer nodules exceeds the solidus tie line then the nodules will not coalesce due to their high rigidity and the skin will be micro-porous. Therefore high polymer concentrations in the initial spinning solution should be avoided.

1.6.2 Defect Repair

Although the fibres produced for gas separation are intended to be defect free in reality they very rarely are. Inevitably there are some defects in the active layer of the membrane which is unsurprising given how thin (≈1000Å) the active layer is. However even a tiny amount of surface porosity ($\approx 10^{-8}$) will result in a useless membrane for gas separation [9]. In order to obtain useful membranes some form of

post production defect repair is required. The defect repair is based on Henis and Tripodi's coating technique [7,8]. The membranes in this study are coated with a silicone rubber which is much more permeable than the polysulphone from which the membrane is made. The silicone rubber blocks any defects in the active layer and allows the membrane to yield the gas separation potential of the polysulphone from which it is made. Although the silicone is much more permeable than the polysulphone it offers considerably more resistance than an open pore.

1.7 Rheology

In the production of textile fibres the effect of rheological conditions on the final morphology and properties have been widely studied [60,73,74]. The rheology of polymer melts and solutions have also been widely studied [75,76]. The effect of extrusion shear on final membrane performance has also been studied [45,77-83].

Polymer solutions experience two type of flow during extrusion to form a hollow fibre, shear and elongation. The solution is sheared as it passes through the annulus and then experiences elongational flow in the air gap.

Flow behaviour under shear is described by the response to tangential force. If the response is linear then the fluid is said to be Newtonian:

$$\tau = \eta\dot{\gamma}$$

where: τ is the shear stress

η is the viscosity

$\dot{\gamma}$ is the shear rate

If the relationship is non-linear then the fluid is said to be non-Newtonian.

$$\tau = k\dot{\gamma}^{n}$$

where k and n are constants for a particular fluid. k is the consistency of the fluid, the higher the value the more viscous the fluid. n is measure of the non-Newtonian properties of the fluid. If n>1 the fluid is said to be shear thickening and if n<1 then the fluid is said to be shear thinning. Many polymer solutions are found to be shear

thinning. This empirical relationship is known as the power law and was proposed by de Waele and Ostwald [84,85].

An important phenomenon related to shear thinning is molecular alignment. As the fluid is sheared the molecules align in the direction of shear, as this happens the viscosity decreases [86].

Recent work has studied the rheology of the polymer solutions used in this work and the degree of molecular orientation present in the final membranes [87,88]. It was found that the molecular orientation resulted in higher than intrinsic selectivities for the membranes produced.

Shilton developed a mathematical model that enables a shear profile to be solved across an annular spinneret for polymer solutions [89]. This enables the shear rate at the outside of the annulus to be calculated and so the level of shear the active layer is subjected to.

Elongational viscosity is measured under tension instead of shear and reflects the stretchability of the fluid. The elongational viscosity is given by

$$\sigma = \eta_e \dot{\varepsilon}$$

Where: σ is the elongational stress

η_e is the elongational viscosity

$\dot{\varepsilon}$ is the strain rate (given by $\frac{W.U.S - L.E.S.}{gap - height}$)

W.U.S. is the wind up speed of the fibre, L.E.S. is the linear extrusion speed of the fibre.

It is difficult to achieve steady state conditions whilst investigating the effect of elongation on a fluid [9]. Previous work has found that polysulphone dopes are strain thinning and therefore not naturally spinnable. This is not found to be the case in reality though, the bore fluid immediately coagulates the lumen of the fibre as it is extruded giving the fibre mechanical strength and enabling a continuous filament to be spun.

The ratio of elongational viscosity to shear viscosity is known as the Trouton ratio. In Newtonian fluids the ratio is 3, a higher ratio indicates the fluid is viscoelastic. Viscoelastic fluids exhibit a non-linear increase in strain rate against time on a stress loading, when the stress is unloaded the fluid relaxes. This gives rise to the concept of relaxation time.

The relaxation time relates to the time taken for strain in the polymer molecules to evanesce i.e. the molecules to transfer from an ordered to a random state. Mackley et al in their paper on characterisation of polymeric and colloidal fluids developed methods to obtain a relaxation spectrum [75]. There exists a spectrum of relaxation times to describe the recovery of a polymer solution after deformation. Each relaxation time relates to a different strain increment. The relaxation time is a complex parameter depending on the nature of the fluid and its flow history.

1.8 Molecular Orientation

Polysulphone membranes produced in this research group have exhibited selectivities above the recognised intrinsic selectivity for the polymer [80,88,90]. This has been attributed to increased molecular orientation in the active layer leading to improved separation properties. The orientation in the active layer has been measured directly using plane polarised FTIR spectroscopy [78,79]. It was proved that increasing the level of extrusion shear increased the level of orientation in the active layer. This next section will discuss the mechanisms of molecular orientation.

There are thought to be three main mechanisms for the development of molecular orientation in polymeric materials. These are phase inversion [91] shear flow [77,78,88,91-93] and elongational flow [60,94-96].

Phase Inversion Induced Molecular Orientation

Serkov and Khanchich examined the development of molecular orientation during the precipitation process of polymer solutions [91]. They found that preorientation was developed during precipitation and that this significantly affected the subsequent stretchability, structure and physical properties of spun fibres. The development of preorientation during phase inversion was explained in a number of ways.

1. Orientation induced by ionotropic coagulation or from the influence of polyvalent metal ions.

2. Orientation as a result of the mechanical stresses set up in the gel as a result of volume decrease due to syneresis.
3. Directional structuration as a result of the movement of the coagulation front.
4. The formation of spherulites.

Molecular orientation by ionotropic coagulation is only applicable to polyelectrolyte precipitation so is not relevant to our system.

The formation of oriented structure due to the stresses set up by syneresis (the spontaneous expulsion of liquid from a gel) involves the two phases set up during phase inversion, the polymer poor and rich phases. The elimination of the polymer poor phase by syneresis causes the gel to shrink. The resultant stresses lead to an ordered structure.

The phase inversion process involves a coagulation front moving through the solution. Serkov and Khanchich suggested that as the front moves through the solution orientation is induced by the coagulation front migration.

Serkov and Khanchich also postulated that as the polymer rich phase solidifies spherulites can form if the energy of interaction with the solvent is high. This process can lead to a highly oriented structure at the molecular level.

Molecular Orientation induced by Shear Flow

Takeuchi et al studied morphological development in a copolyester fibre with increasing shear rate [92]. They observed a skin-core structure in the extrudate and characterised this in terms of band patterns, which were monitored through a polarising microscope. At low shear rates the extrudate showed homogenous textures in the radial direction. At shear rates above 122 1/s the extrudate exhibited a skin-core structure. At a shear rate of 608 1/s a pattern of bands parallel to the shear direction was evident in the outermost region of the filament. Takeuchi et al studied the texture of the extrudate by birefringance and showed that the molecular orientation was concentrated in the skin layer.

Bousmina and Muller proposed a mechanism to explain the development of an ordered structure as a result of shear in an extruded filament [93]. They extruded a polymethylmethacrylate (PMMA)/ rubber blend. By considering the non-Newtonian velocity profile across the filament they described a process which particles become aligned in the direction of shear. Two particles were considered, a and b with positions Z_a and Z_b respectively at time t1. Particle a moves faster than b and catches it at time t2. The particles form a doublet due to interaction and it rotates due to the different velocities of the constituent particles. The doublet then flows downstream, aligned in the direction of extrusion as a unique particle. The process is then repeated as the larger particle catches up with another smaller particle. This is shown in the diagram below.

Fig 1.19 Particle Alignment in Shear Flow

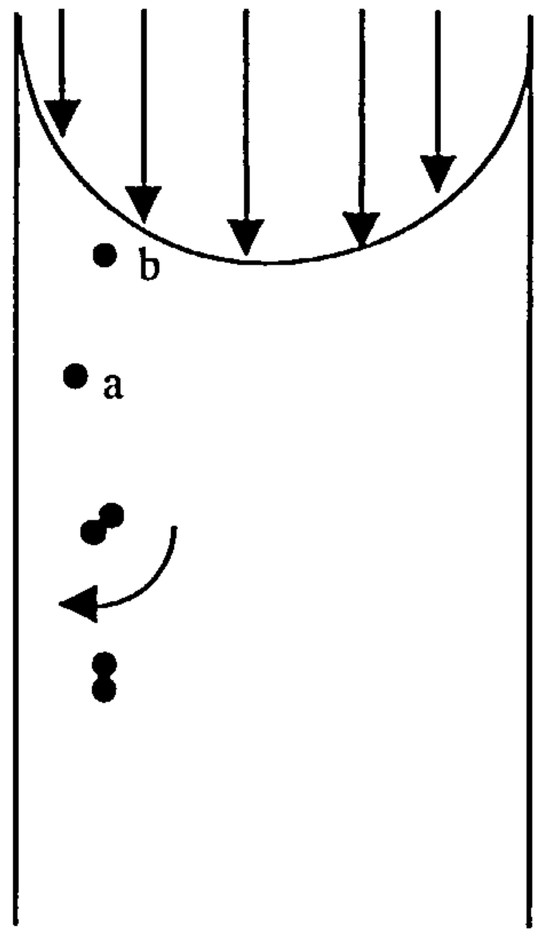

To illustrate the flow profile experienced by the particles Bousmina and Muller conducted a rheological characterisation of the PMMA/rubber blend. In their tests the power law index was in the range 0.15 to 0.3. These values indicate that high shear rates were only experienced at the wall with plug flow in the middle. This explains the skin-core morphology they found. Transmission Electron Microscopy showed that the outer region was oriented.

Mackley studied a variety of flows, both shearing and extensional and observed the effects on end to end distance and flow birefringence [97]. He found that as shear increased the end to end distance increased as well. This would lead to molecular orientation if the molecules could be frozen in this extended state.

Serkov and Khanchich also postulated that shear induced orientation is frozen into the skin of a fibre during extrusion [91].

Ismail et al also directly measured shear induced orientation in membranes and concluded that increased shear leads to increased orientation [78,79].

Molecular Orientation Induced by Elongational Flow

Perepelkin outlined the principle aspects in the structural reorganisation of polymer solutions by elongational flow and these are [94]

1. A change in the orientational and three dimensional order of the structure
2. An increase in the degree of orientation of the crystalline and amorphous sections of the structure.
3. A change in the conformational arrangement of the molecule chains.
4. A change in the supra molecular structure. [An increase in packing density and size of cyrstallites and change in the structure of the amorphous sections.]

Perepelkin stated that although stretching flow causes molecular orientation the mechanical properties of the extrudate are also dependant on the shear induced orientation which occurs in the spinning process.

Serkov and Khanchich demonstrated the alignment of polymer molecules under different stretch ratios using small angle laser scattering [91].

Elongational flow behaviour of Polyacrylonitrile (PAN) solutions and the effect of non-solvent in the dope during the wet spinning of fibres was investigated by Ferguson et al [95]. They found that the addition of water to the dope solution

increased the elastic modulus in elongation of the filament. This results in greater relaxation times and hence more elongation induced molecular orientation being frozen into the structure [96].

Mackley found that for extensional flow once a threshold was passed all the molecules became fully extended [97]. This threshhold depended on the rate of strain and the relaxation time of the polymer molecule. They also found that the relaxation time was dependant on the velocity gradient, as the velocity gradient increased the relaxation time decreased.

1.9 Rheology and Phase Separation

The effect of shear on the phase behaviour of polymer blends and solutions has been widely studied [98,99].

Kammer et al devote an entire chapter in their review paper to the phase behaviour of polymer blends while flowing [98]. They noted that small changes in the rate of deformation can result in dramatic changes in the phase behaviour. The critical temperature was found to change by up to 30°C. This was attributed to the high viscosity of the blends damping out concentration fluctuations and the ability of the molecules to store energy.

Jou et al in their review paper also noted the effects of shear on the phase behaviour of polymer solutions [99]. They noted that the critical points and spinodal lines shift on the phase diagrams of systems under shear as opposed to the same systems at rest. They also noted that some polymers solubility is enhanced by shear and other polymers have their solubility hindered by shear.

Wolf has studied the effects of shear on polymer solutions and blends for some time [100]. In an early paper the thermodynamics of flowing polymer solutions was modelled [101]. The effect of shear on phase separation was modelled and phase diagrams were plotted. It was found that solubility was improved for the systems studied. This was in accordance with experimental findings [102], however Wolf

also noted that for high molecular weight polystyrene in trans-decalin the solubility was hindered by shear.

Wolf and Horst then studied phase diagrams. Horst developed a technique whereby phase diagrams could be calculated for a ternary system using only the Gibbs free energy of mixing [103]. This avoided the need to find the 1st and 2nd derivatives of ΔG_m. The function describing ΔG_m can become very complex because of the interaction parameters for the different components. The technique involved iteratively varying the composition of the mixture. The different points of varying composition are found by dividing the ternary diagram into a grid. The number of points located within the grid is (n-2)(n-1)/2 and 1/n is the distance between the points. In this example n = 5

Fig 1.20 Ternary Diagram in Grid Format

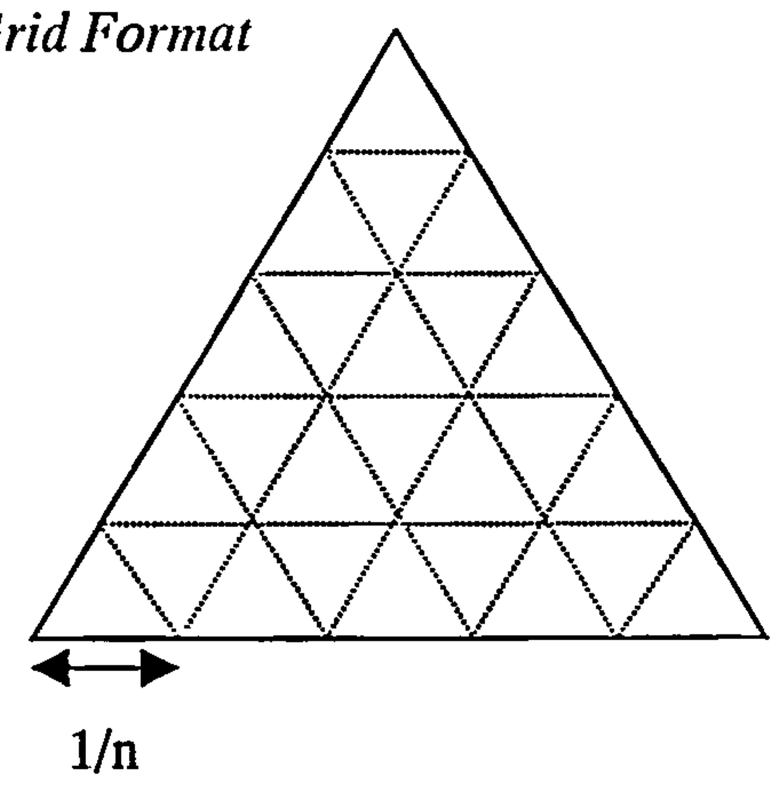

For each point of the iteration (grid pt.) the mixture is arbitrarily split into two phases of equal volume and the value of ΔG is calculated for the two de-mixed phases. If this value is less than the value of ΔG for the homogenous system then the composition lies within the spinodal region. Once all the points within the spinodal

line are calculated the tie lines and binodal line are calculated. The tie lines are calculated by choosing a point within the spinodal region and finding the composition of the two de-mixed phases which give a minimum value of ΔG. This is done by iteratively varying the volume fraction and composition of the two phases with respect to the starting composition. Once the two compositions are found these represent either end of the tie line. Once enough tie lines are found the binodal line can be found by linking the ends of the tie lines together.

The technique was developed for ternary systems but was easily extended to model quaternary polymer blends and even more complex systems [104].

Horst and Wolf then extended the technique to plot phase diagrams for sheared systems [105]. The technique only requires knowledge of the Gibbs energy of mixing and not it's derivatives so the mixing term can be extended to include shear effects without fear of complicating the derivative functions. The contribution to the generalised Gibbs energy of mixing due to shear takes the form of a stored energy term. The stored energy term was developed in an earlier paper [101].

The effect of moderate levels of shear on polymer solubility was studied and phase diagrams were developed from the models. Horst and Wolf found that the behaviour of a ternary polymer blend system under shear was quite complex. At certain levels of shear the mixture became completely homogenous as the shear induced mixing, at other levels of shear the effect was to increase the de-mixing area.

This behaviour is explained in terms of molecular entanglements. At low shear levels the number of entanglements is proportional to $\dot{\gamma}^2$. Once the region of Newtonian behaviour is left the shear rate exceeds the inverse of the characteristic viscometric relaxation time and the number of entanglements decrease with increasing shear [106]. This implies a decrease in the stored energy and so gives rise to the increase in the de-mixing area.

Wolf summarised the effects of shear and pressure on polymer solubility in one recent paper [107]. The paper explains how the effect of shear could increase or decrease the solubility of a polymer depending on the ability of the system to store energy.

Fig 1.21 Effect of shear on Gibbs free energy of mixing

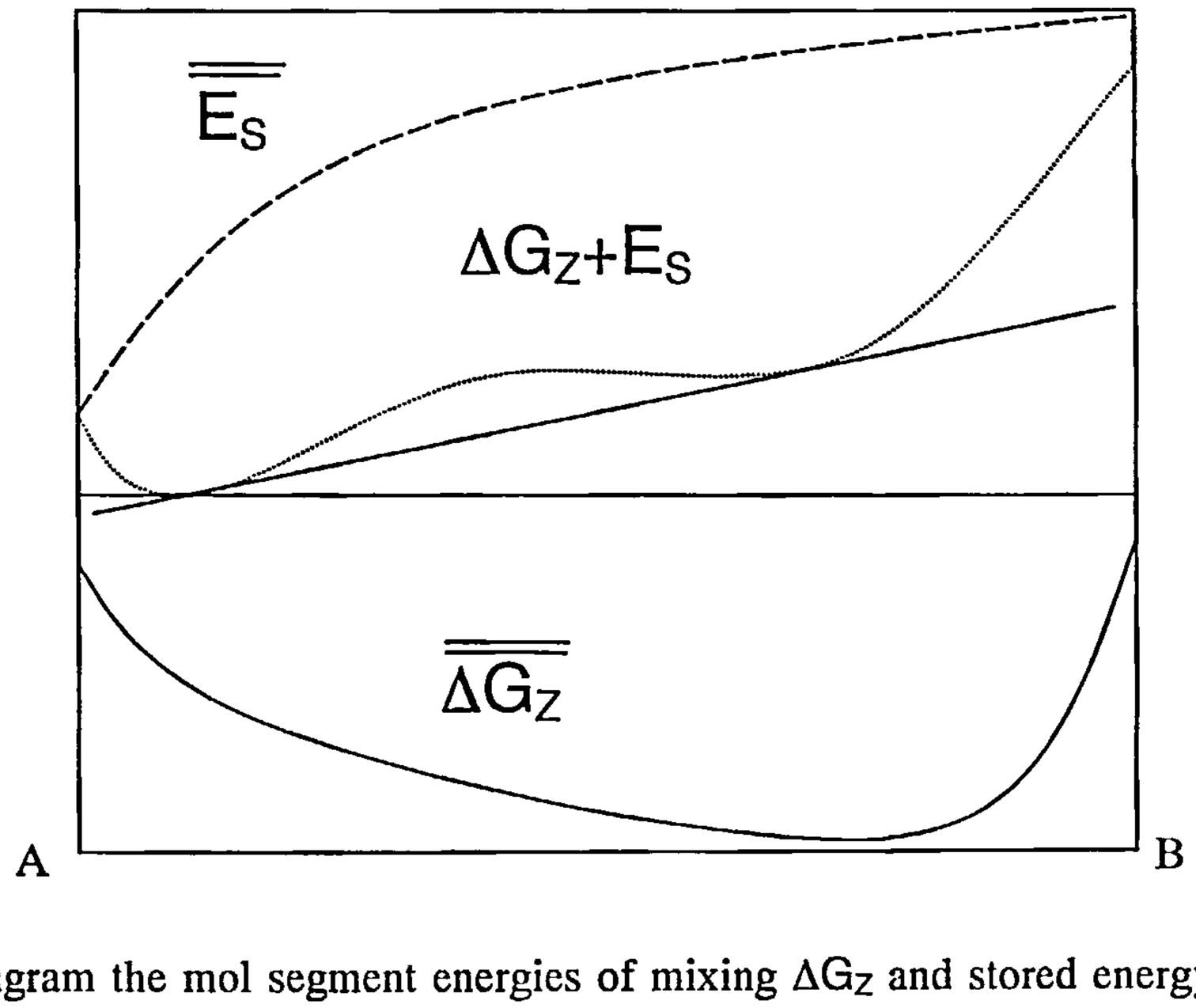

In this diagram the mol segment energies of mixing ΔG_Z and stored energy E_S are shown plotted against composition on the same diagram for a flowing system. The sum of the two energies is also plotted on the diagram. The resulting curve shows

how an apparently stable mixture can phase separate under flow due to the contribution of stored energy.

1.10 Composite Materials.

It has long been recognised that polymer structures can be reinforced by adding either glass or carbon fibres to the polymer matrix. The resulting composite materials have superior mechanical properties. The glass or carbon fibre additives are considerably stiffer than the polymer material and so when added increase the strength of the composite [108].

The attainment of good mechanical properties depends crucially on the efficiency of stress transfer from the resin matrix to the fibre so the adhesion of the fibre to the resin matrix is vital [109].

In this study a novel type of carbon fibre was added to the polymer dope in order to reinforce the spun fibres [110].

1.11 Objectives

Membrane gas separation has now become a commercially viable process. Phase separation aspects of membrane production have been widely studied and now fabrication conditions and their effect on final membrane performance are beginning to be studied. This work studies two fundamental physical aspects of the production of dry/wet spun hollow fibre membranes, the level of shear experienced during extrusion and the residence time in the air gap.

As has been mentioned, prior work in our research group has produced membranes with enhanced selectivities. Such results have been discussed in terms of molecular orientation induced in the membrane active layer during fabrication. However, the underlying reasons for this phenomenon have only been partly understood due to the hitherto lumped treatment of the critical spinning parameters involved.

Two critical influences in establishing the molecular conformation of the active layer and the morphology of the membrane cross section, and hence the separation properties of the membrane, are the extrusion shear in the spinneret and the residence time in the forced convection chamber during spinning. The previous work in our laboratory did not examine these factors independently. In this work however, for the first time, experiments have been designed, to enable the de-coupling of these two effects. This development has allowed the isolated influence of extrusion shear on fibre structure and hence pressure-normalised flux and selectivity to be researched.

This new approach has also allowed the forced convection process to be better understood in terms of the mass transfer occurring during skin formation.

The separate analyses of shear effects and forced convection residence time were initially applied to the "standard dope" used in our laboratory (22% w/w polysulphone). However the membranes were mechanically weak which would preclude them from serious industrial application.

In order to address the strength problem, a higher solids content of the original spinning dope was prepared (40% w/w polysulphone). This solution was significantly more viscous and thermal modifications were made to the spin line to compensate. A programme of research investigating the use of this more concentrated system was then conducted which also successfully unravelled the effects of extrusion shear and forced convection residence time. The resultant fibres were sufficiently robust for industrial use but morphological deficiencies rendered them insufficiently productive for industrial applications.

A final phase of work involved the novel investigation of using fillers to reinforce membranes spun from lower concentration dopes. The objective was to produce highly permeable and selective membranes of sufficient mechanical robustness for industrial use. The filler adopted was vapour grown carbon fibre (VGCF).

During the above research, structural models were developed to deduce the fine morphological details of the membranes. This information was then used to interpret

the relationship between spinning parameters and membrane performance. Two further models were produced, one to analyse the mass transfer occurring during forced convection, and one to explain the mechanism of membrane skin coalescence.

Chapter 2:

Experimental Techniques

2.1 Dope Preparation

The polymer solutions for fibre spinning were prepared using the apparatus shown in fig 2.1.

Fig. 2.1 Dope Preparation Equipment

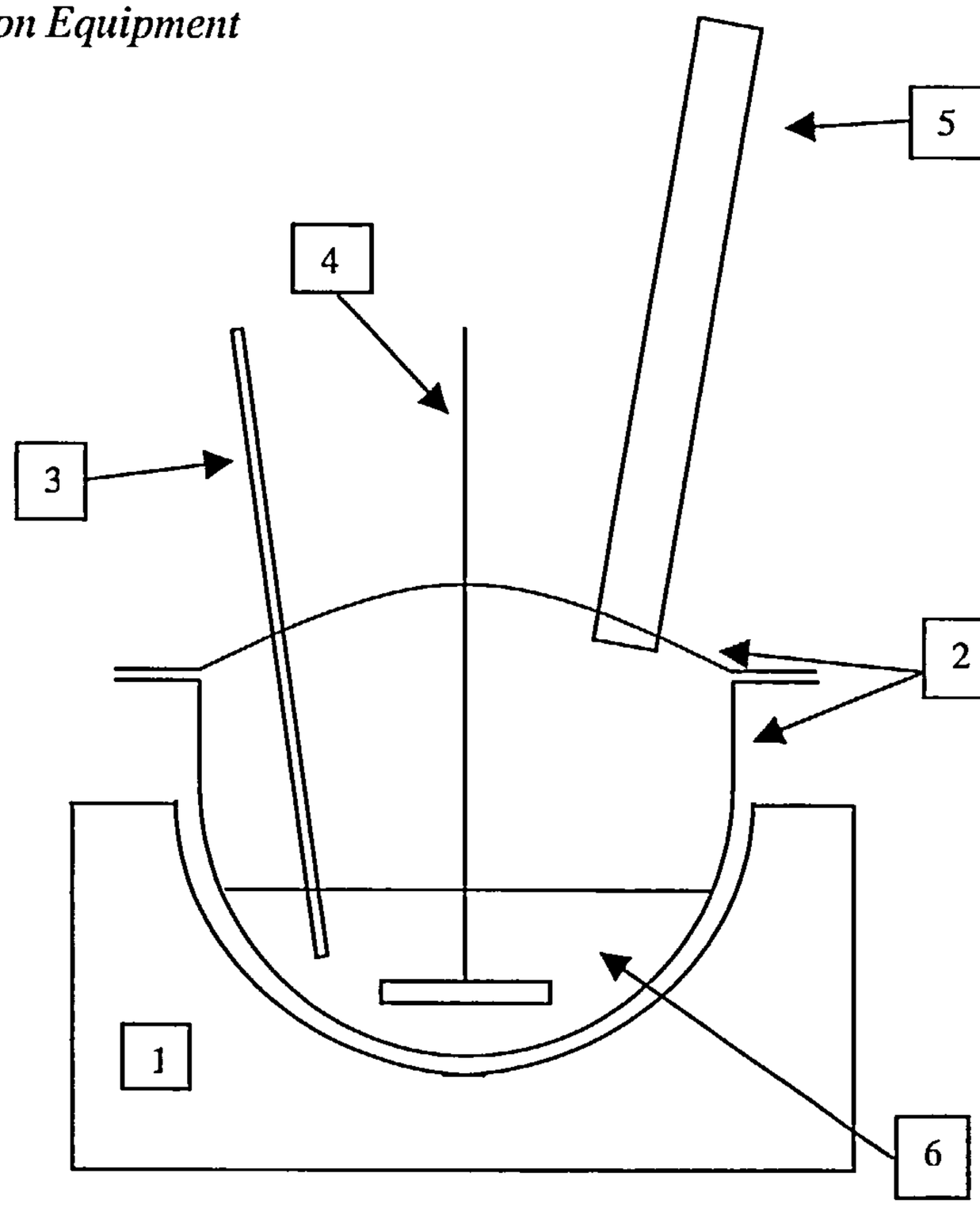

1. Electric Heating Mantle
2. Reaction Flask and Lid
3. Thermometer
4. Electric Stirrer
5. Total Reflux Condenser
6. Polymer Solution

Two polymer dopes were used to spin hollow fibre membranes, a low and high polymer concentration dope. Both polymer dopes were developed by Pesek and Koros [67,68]. The low polymer concentration dope contained 22% w/w Polysulfone (Psf), 31.8% w/w Di-methyl-acetamide (DMAC), 31.8% w/w Tetrahydrafuran (THF) and 14% w/w Ethanol (EtOH). The high polymer concentration dope contained 40% w/w Psf, 35.7% w/w DMAC, 11.9% w/w THF and 12.4% w/w EtOH.

The polysulphone is the membrane forming polymer. The Di-methyl-acetamide is the base solvent: it is a strong solvent and is used to dissolve the polymer. The tetrahydrafuran is the volatile solvent. It is also a solvent for polysulphone but is not as a strong. THF is however very volatile, the purpose of adding THF to the dope is so that it evaporates in the forced convection chamber bringing the polymer dope into a thermodynamically unstable state. The ethanol is a non-solvent and is added to make the dope thermodynamically unstable as the THF evaporates.

Both dopes were prepared using the following method. First the flask was charged with the correct amount of DMAC (the 22% dope was prepared in 500g batches the 40% dope was prepared in 250g batches due to stirrer limitations). The stirrer was then turned on to vigorously agitate the solvent and the polymer was added in one batch. The electric heating mantle and condensor were then turned on and the temperature was allowed to rise to 80°C. Once the polysulfone had dissolved the EtOH and THF were added together to prevent any localised coagulation. The dope was then left for at least 2 hours at 80°C to de-gas.

Table 2.1 gives the manufacturers specification for the different chemicals.

Table 2.1 Chemical Specification

Chemical	Grade	Manufacturer	Other Information
Polysulfone	Udel P 1700 as received.	Amoco Chemical corp.	Weight-average molecular weight 34,500
Tetrahydrafuran	Analytical grade purity (99.7%)	BDH Chemicals	
N,N-Dimethylactamide	HPLC Grade (99.9+ %)	Sigma-Aldrich	
Ethanol	Reagent (99%)	University Chemical Store	Produced in the university

2.2 Rheological Characterisation of Polymer Dopes

The steady state flow properties of the polymer dopes were measured using a T.A. instruments A.R. 1000 rotational rheometer. Due to the volatile nature of the dopes a solvent trap was used to prevent the evaporation of THF from the dope. Reliable and consistent results were achieved using a 2cm parallel plate geometry with a gap of 100μm. The test lasted 5 mins with a 20s period of pre-shear at a minimum shear rate. The test was a continuous ramped experiment. The tests for the 22% dope were carried out at 20°C and for the 40% dope at 50°C.

2.3 Hollow Fibre Spinning

Spinneret

The hollow fibres were spun using a tube in orifice annular spinneret that was developed in house

Fig 2.2 Hollow Fibre Spinneret

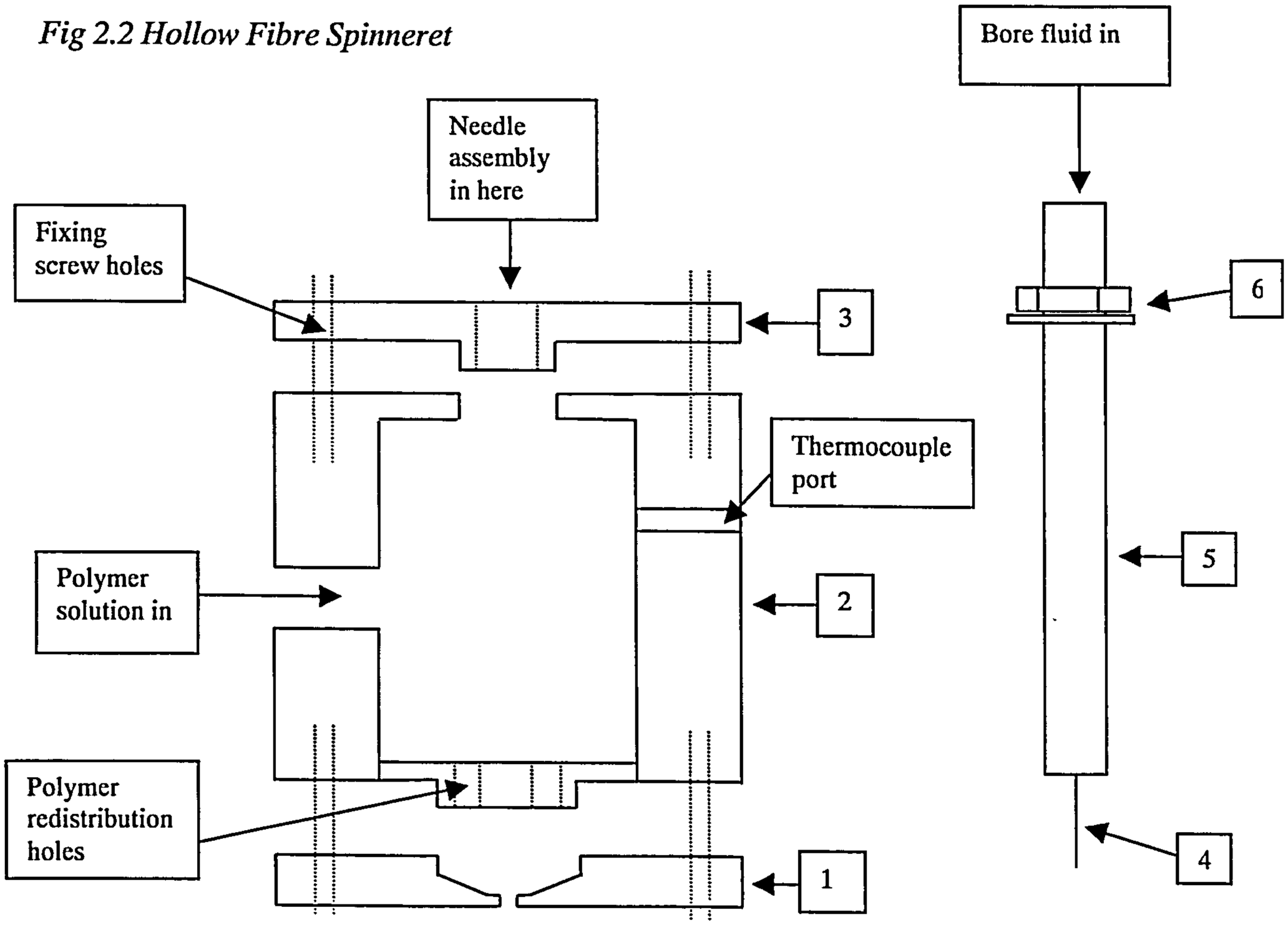

1. Spinneret base plate with extrusion hole
2. Spinneret body
3. Spinneret end plate
4. Bore fluid injection needle
5. Needle holder
6. Length adjusting screw and seal

The spinneret is of modular construction for ease of cleaning and also allows for the needle to be replaced. The spinneret is constructed of stainless steel and has a thermocouple port so the temperature of the dope can be measured as it is spun.

Spin Line

The polymer dope is stored in a stainless steel reservoir which is pressurised to prime the pump. The dope is delivered to the spinneret by a metering gear pump. The gear pump is a robust type of pump and so can handle highly viscous polymer dopes but is also very accurate and so has a precise output. The bore liquid is fed to the spinneret using a calibrated syringe pump. This gives a pulse free and highly accurate flow of bore liquid.

Fig 2.3 Extrusion System

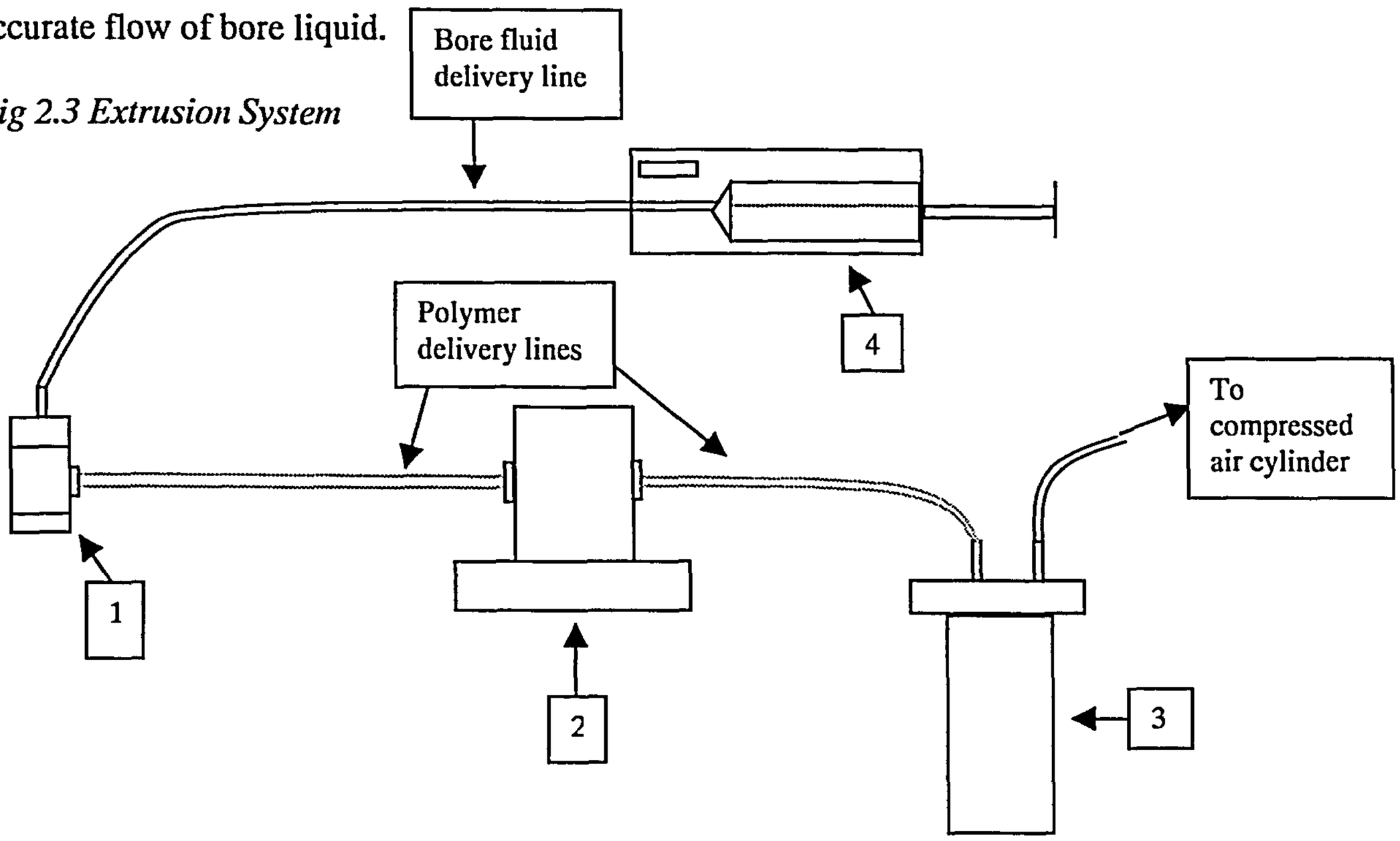

1. Spinneret
2. Metering Gear Pump
3. Dope Reservoir
4. Syringe Pump

On extrusion the polymer filament passes through an air gap of varying length. In this series of experiments the air gap was flushed with 4 litres/min of dry nitrogen. The filament then passes through two coagulation baths before being collected on the wind up drum which also sits in a water bath. The existing spin line was modified for this campaign of spinning to minimise friction in the coagulation baths. The roller layout was modified to ease the changes in direction as the fibre travels through the coagulation baths. The change in residence times in both baths due to the change in roller layout was minimal, however the change in the tension in the filament was significant.

Fig. 2.4 Spin Line

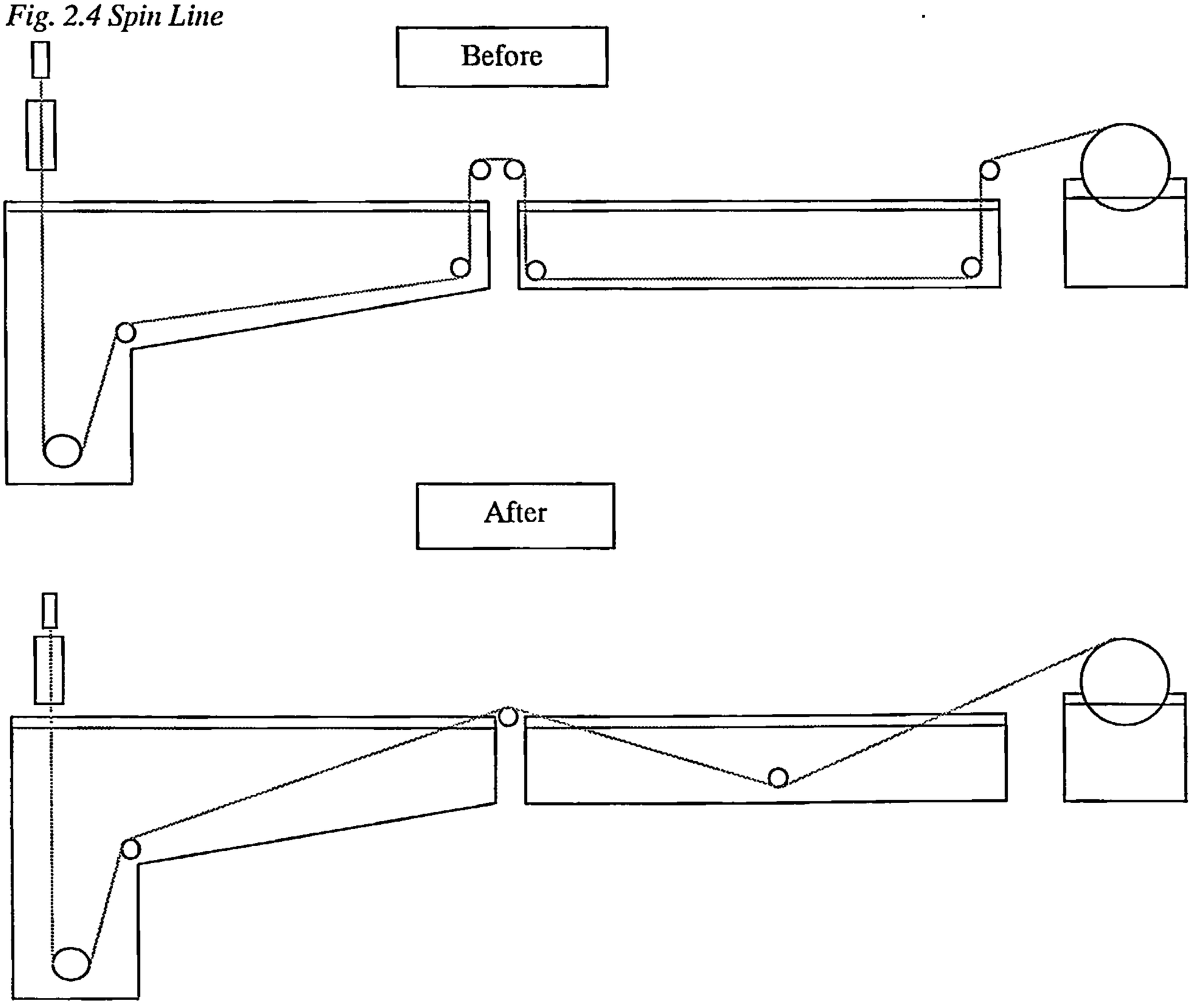

All the baths are filled with pure water. The first bath is temperature controlled at 14°C and the other baths are at room temperature.

The bore fluid used is an aqueous solution of potassium acetate. Throughout the experimental campaign the bore fluid used was a 20% w/w solution, this gives a water activity of 0.9 [68].

Post Treatment

After the fibres are collected from the take up drum they are steeped in distilled water for 48 hours to remove any residual traces of solvents. The fibres are then transferred to a methanol bath for 24 hours where the water is removed. The fibres are then air dried. The water is removed before drying to prevent the fibres being damaged as the water evaporates. As water evaporates from small pores high surface tension forces can be generated and these can damage the membrane active layer [111]. As methanol evaporates it generates much less force so does not damage the membrane.

2.4 Module Preparation

Module Fabrication

In order to test the gas permeation properties of the membranes the fibres are potted into modules. The module consists of a tube sheet and end cap with the fibres in between.

Fig 2.5 Gas Permeation Test Module

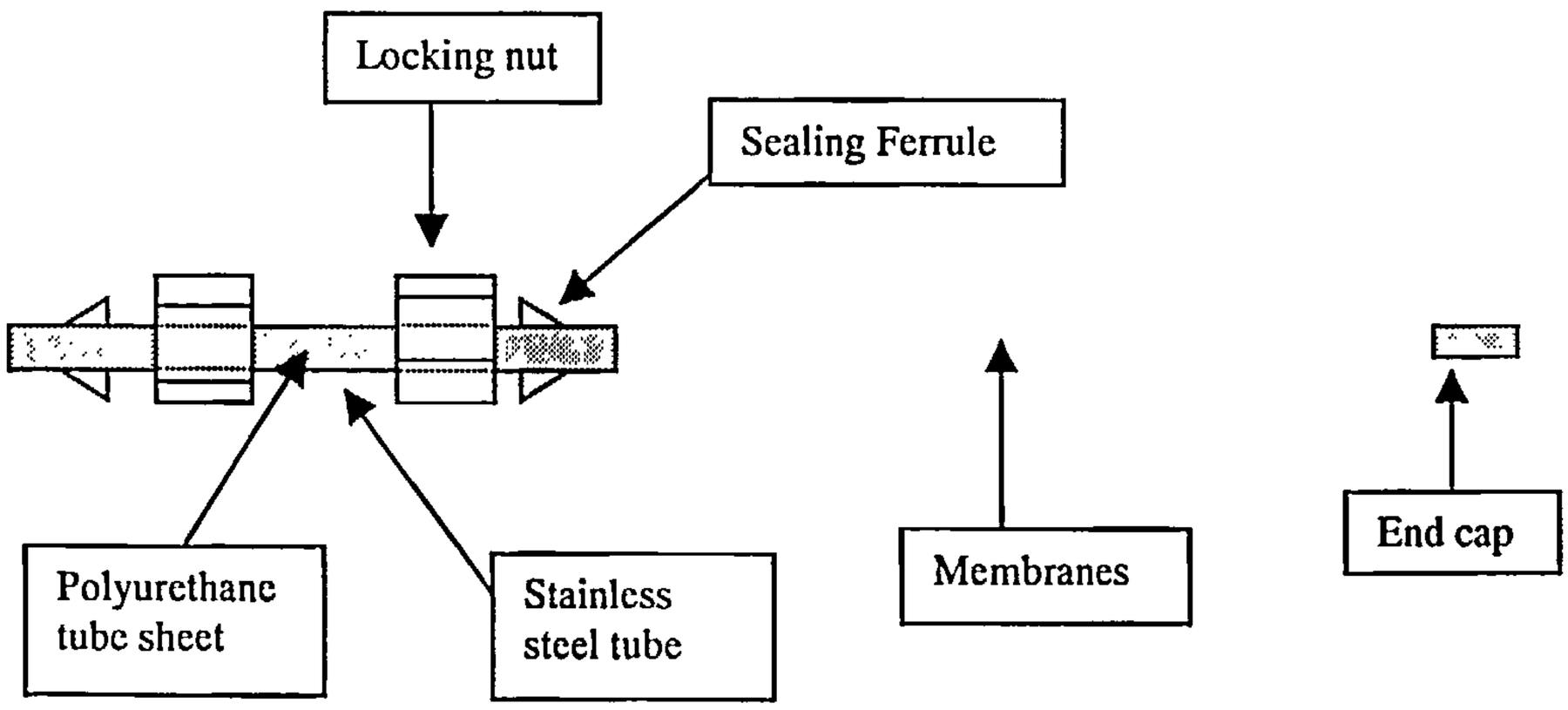

The potting material used to fix the membranes in place was a two component polyurethane resin. This polyurethane resin did not contain any solvents which would damage the fibres and set strong enough to resist the pressures experienced during testing. The resin also had a long enough set time to allow it to be worked with. The details of the resin are given in table 2.2.

In order to construct the modules the components of the module were placed in a jig.

Fig 2.6 Module fabrication rig

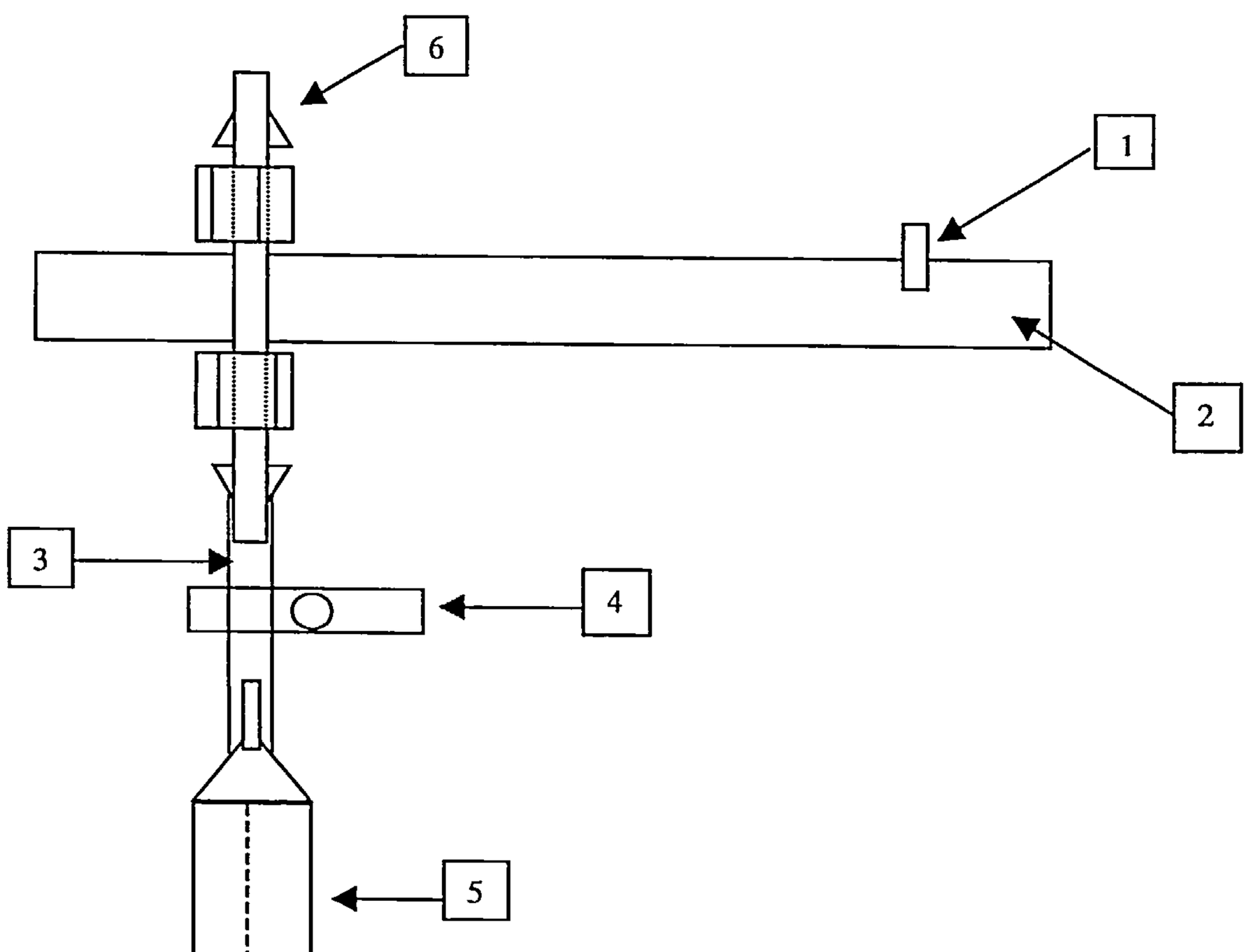

1. Module end cap
2. Potting stage
3. Silicone tube
4. Tube clamp
5. Syringe to inject potting material
6. Membrane tube sheet

The resin was mixed together in the correct proportion and then de-gassed using a vacuum pump. The resin was the injected into the end cap and the fibre fixed in place. The fibre was then fed through the tube sheet and resin was injected up into the tube sheet and the silicone tubing was clamped. The resin was left to set and then the resin plug was cut flush with the tube sheet to expose the fibre lumen.

Table 2.2 Resin Specification

Component	Description	Supplier
PUR 725 A	Polyurethane prepolymer	Morton Adhesives
PUR 634 B	Polyester resin	Morton Adhesives

Coating

Once the membrane module has been constructed the membranes are silicone coated. The coating repairs any surface defects and allows the membrane to exhibit the full separation properties of the polymer it is made of. The silicone coating is very permeable and does not exhibit any significant selectivity [112].

To coat the membranes a silicone solution was made. The silicone and curing agent were dissolved to make a 3% w/w solution in hexane. The modules were then immersed in the solution for 10 mins. and then allowed to air dry for 24 hrs. The details of the silicone coating system are given in table 2.3.

Table 2.3 Silicone coating specification

Material	Supplier
Sylgard 184 silicone elastomer (base and curing agent)	Dow Corning
N-Hexane (solvent for Sylgard 184)	Chemistry store, University of Strathclyde

2.5 Gas Permeation Testing

A new multi-chamber rig was designed for the gas permeation testing phase of the project. A rig was designed that would allow up to 6 modules at a time to be tested. This allows for much faster testing and less cylinder handling as all four test gases are attached to the test rig. The rig also allows gas mixtures to be tested and the permeate composition to be tested on line using a gas chromatograph (G.C.).

Fig 2.7 Multi-chamber rig

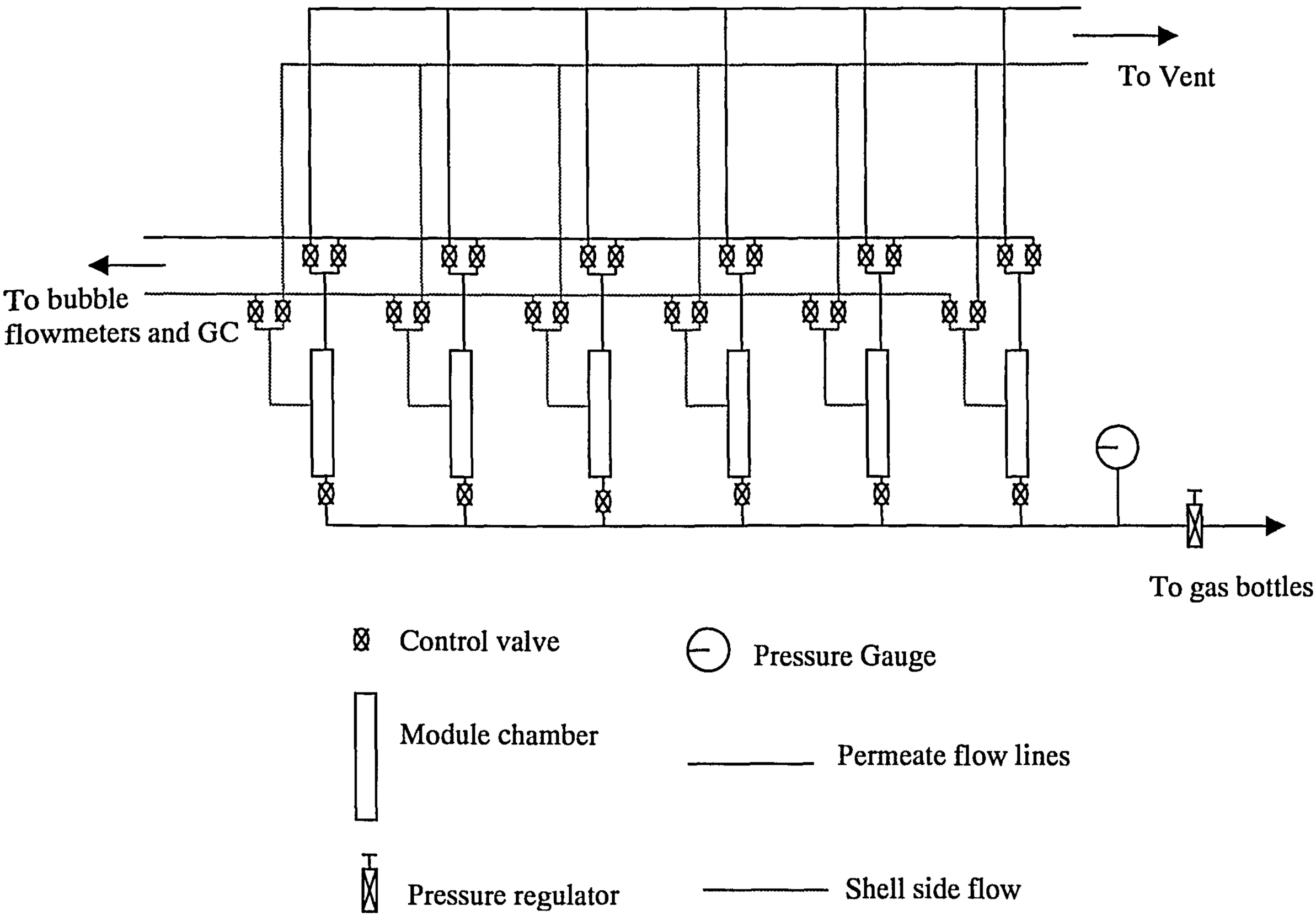

Pure Gas Testing (Coated and Uncoated)

The modules are fitted into the test rig.

Fig 2.8 Permeation chamber

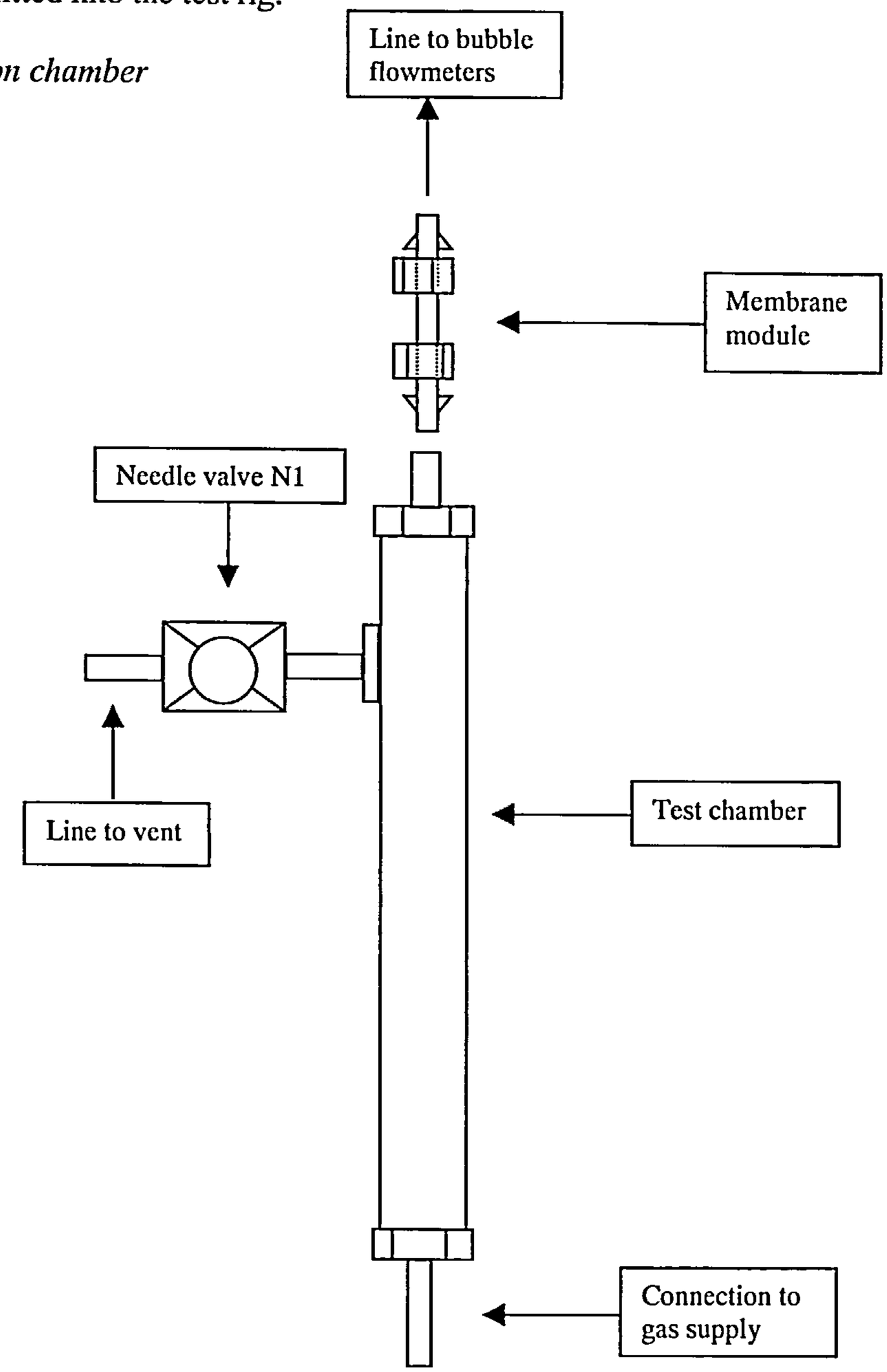

The rig is then flushed with the test gas before being pressurised. The permeate flowrate was measured on a bubble flowmeter. The needle valve N1 is left fully open during pure gas testing. Once the test is over the cylinder valve is shut the vent valve is fully opened and the rig depressurised before being flushed with the next test gas.

Gas Mixture Testing

For gas mixture testing the modules are again fitted into the test rig. The rig is flushed with the test gas and then pressurised. The needle valve N1 is then slightly opened and the vent valve is fully opened. The permeate flowrate is then measured on the bubble flowmeters. The needle valve is then opened until the shell side flow is 10x the permeate flow. This is done so the composition of the gas in the test chamber is the same as the gas in the cylinder. Once both flows have been set a tube is attached to the tube sheet and then to the inlet port on the G.C. The time required to flush the tube with permeate gas is then calculated (Tube volume/permeate flowrate), this time is then multiplied by 5 and after that time has elapsed the permeate composition was measured. The G.C. data is interpreted by a graphical integration package on a P.C. which is interfaced to the G.C. The integration package gives the composition of the permeate gas in volume %. After the test the cylinder valve is closed and the needle valve is fully opened to allow the test chamber to depressurise before being flushed by the next test gas.

The mole fraction of component i in the permeate stream is measured directly using the on line gas chromatograph, a simple mass balance then calculates the mole fraction of component i in the retentate stream. The concentration of component i in the module is taken as the average of the retentate and feed mole fractions. This is more precise than assuming the concentration in the chamber is the same as the feed concentration. This is an improvement on the well mixed model. The permeability of the gases is worked out using the concentrations of the permeate and feed streams.

2.6 Fibre Tensile Tests

In order to obtain bulk physical properties of the fibres they were tested on an Instron 1122 Materials testing instrument. The fibres linear density was first obtained. This is done by weighing a known length of fibre and the then working out the linear density in g/km or tex. This meant that all results obtained could be standardised w.r.t. to linear density.

The fibres were analysed to give a stress/strain curve. A typical curve is shown below.

Fig 2.9 Typical Stress vs. strain curve

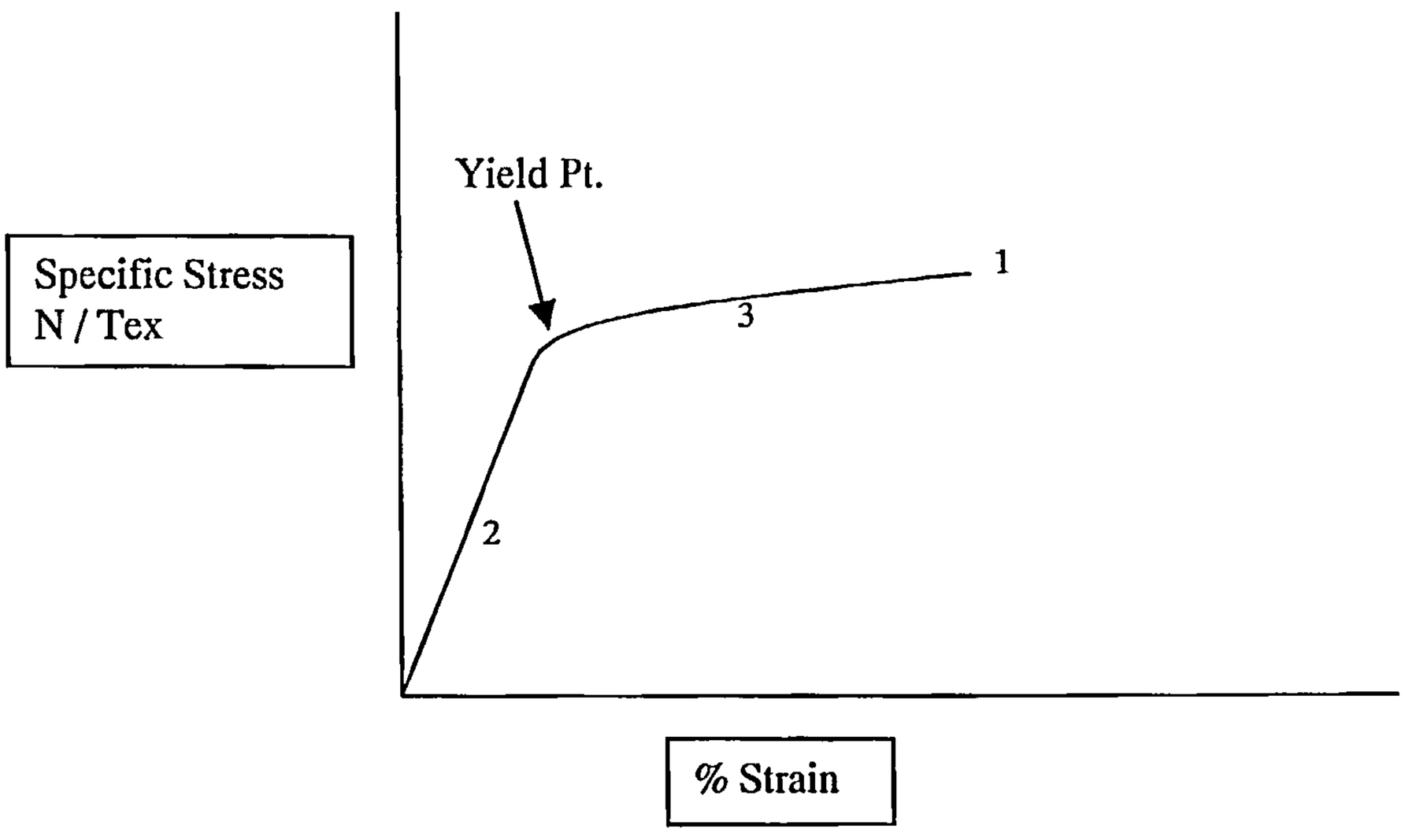

The main areas of interest are:

1. Fibre strength or Tenacity: this is the specific stress at break = load at break/linear density of fibre.

2. First Modulus M1: this is the slope of the stress/strain curve before the yield point.
3. Second Modulus M2: this is the slope of the stress strain curve after the yield point.

The first modulus is a measure of resistance to extension before the elastic limit is reached.

The second modulus is a measure to the resistance after yield i.e. after the structure has been broken.

Chapter 3:

De-coupling Extrusion Shear and Forced Convection Residence Time in the Production of Hollow Fibre Gas Separation Membranes

3.1 Introduction

In this phase of work hollow fibre gas separation membranes were spun using a 22% Polysulphone dope. Recent work in our group has studied the effects of shear and elongation on membrane performance [45,77-80,88,90]. Shilton et al in early work studied the rheological properties of polymer dopes [80].

Shilton then studied the effects of extrusion shear and elongation. Shear was studied by altering the dope extrusion rate while keeping the jet stretch ratio constant. The jet stretch ratio is the ratio of wind up speed to extrusion speed so keeping it constant is important to eliminate any effects from drawing. Elongation was studied by varying the jet stretch ratios at constant dope extrusion rate. Although this early work did not produce very selective membranes it did study fabrication parameters for the first time. Until this work almost all membrane research was focussed on the phase inversion process.

Shilton's later work then studied gas transport through membranes and then developed a resistance model [45]. Further work then developed a model to solve flow conditions for a power law fluid flowing through an annulus to simulate fibre spinning [89].

The next phase of work in the group then focussed on the measurement and effects of molecular orientation on the performance of gas separation membranes. Ismail et al produced flat sheet polysulphone and polyacrylonitrile membranes at different levels of shear [78]. They qualitatively measured the amount of molecular orientation

imparted at high and low shear. The molecular orientation was measured using plane polarised infra red reflection spectroscopy. They then studied the gas permeation properties of the membranes produced. The results showed that qualitatively the higher shear membranes exhibited more molecular orientation for both polymers. The gas permeation results were again disappointing and the membranes did not exhibit high selectivities. The high shear membranes however were more selective for both polymers.

Ismail at al then produced hollow fibres using a multi-component dope developed by Pesek and Koros for flat sheet casting [67]. The dope used was 22% w/w polysulphone, 31.8% w/w N,N-dimethylacetamide, 31.8% w/w Tetrahydrofuran and 14.4% w/w Ethanol. Pure water was used as both internal and external coagulant. The fibres were dry gap wet spun with an air gap of 9cm at two different extrusion rates to give low and high shear membranes [79].

The fibres were spun using forced convection in the dry gap, the gas used was dry nitrogen. These membranes were analysed spectroscopicaly for molecular orientation and the gas permeation properties were studied using CO_2 and CH_4. The spectroscopy showed increased orientation in the high shear membranes. Once coated the high shear membranes exhibited the intrinsic selectivity of the polymer for the CO_2/CH_4 separation. This suggested that the membranes formed had very few surface defects and that they were small enough to be repaired.

Ismail then lowered the water activity of the bore coagulant and repeated the spinning campaign of low and high shear again with forced convection in the air gap [80,88]. The resulting membranes produced were very impressive. They were again analysed using IR spectroscopy and tested using CO_2 and CH_4 gas permeation. The spectroscopy results were disappointing as no clear conclusions could be drawn from them. The gas permeation results were however exceptional. The membranes exhibited more than twice the intrinsic selectivity of the polymer. This increase in selectivity was attributed to increased orientation in the active layer of the membrane.

Other groups have also studied the effect of rheological parameters in the production of hollow fibre membranes.

Aptel et al studied the effect of shear on the production of hollow fibre ultra-filtration membranes [81]. They found that increased levels of shear changed the shapes of the pores and increased the selectivity.

Ekiner and Vassilatos spun polyaramide hollow fibre membranes for methane/ hydrogen separation [82]. They studied the rheology of the spinning dopes and concluded that the high viscosity of their dopes suppressed macro-void formation.

In their most recent paper Ekiner and Vassilatos studied the spinning and properties of hollow polyaramide fibres [113]. They discussed the rheology of the polymer dope in both shear and extensional deformation. They found that their polymer dope was shear thinning but extension hardening. They described the flow of a spinline as

mostly extensional, however all their fibres were produced with draw ratios in the range 5-10 so extensional flow would be a factor in their work. They also observed considerable die-swell with their polymer dopes.

Chung et al have studied the effects of air gap distance and more recently shear on the properties of hollow fibre membranes. The effect of air gap distance on the morphology and thermal properties of Polyethersulfone hollow fibres was studied [114,115]. The work varied the length of the air gap and found that as the length of the air gap increased so the permeability of the fibres decreased. They also analysed the fibres using Differential Scanning Calorimetery to find the glass transition temperature (Tg) of the fibres. They found that as the air gap distance increases the Tg falls. This was attributed to different precipitation pathways resulting in different final structures.

In a later paper polyethersulfone fibres were wet spun at different rates of shear and the effect of shear on morphology and fibre performance was analysed [116]. It was found that increased shear increased the selectivity and changed the morphology of the fibres.

In a paper on ultra-filtration membranes the effect of shear on morphology, performance and the mechanical properties of polyethersulfone hollow fibre membranes was investigated [83]. The fibres were wet spun and it was found that increasing shear increased the separation performance but lowered permeability. They reported a critical shear above which selectivity did not improve.

Wang et al prepared polyetherimide hollow fibre membranes for gas separation [117]. The membranes were produced at a variety of air gaps while extrusion conditions were kept constant. They found that the length of air gap had a significant effect on fibre performance. They found that as air gap length increased the internal coagulation front advanced to the outside of the fibre and damaged the active layer of the membrane. They concluded that at longer air gaps the coagulation front took part in the forming of pores in the active layer. This conclusion was supported by gas permeation testing and electron microscopy.

In previous work in this group fibres were produced at different levels of extrusion shear. This was done by varying the dope extrusion rate, however the air gap length was not varied and so residence time in the air gap varied. This meant that two factors were working together: residence time and extrusion shear.

In Chung's work on the effects of air gap it is impossible to quantify any jet stretch due to the variations between Dope extrusion rate and take up velocity. In his work the fibres were also wet spun and so are significantly different to ours.

In this work for the first time we isolate shear from residence time and study both separately.

3.2 Experimental Campaign

Asymmetric hollow fibre membranes were spun using the dry/wet spinning process with forced convection in the air gap. The spinning dope was an optimised 4 component dope developed by Koros and Pesek [67]. The dope used was 22% w/w polysulphone, 31.8% w/w N,N-dimethylacetamide, 31.8% w/w Tetrahydrofuran and 14.4% w/w Ethanol.

The dope reservoir was kept at 20°C (± 2°C). The dope was delivered from the dope pot to the spinneret by a metering gear pump. The fibres were extruded from the spinneret (O.D. 600μm I.D. 330μm) through the forced convection chamber into the first coagulation bath. The forced convection chamber was a tube of 5cm diameter and of different lengths. The forced convection chamber was flushed with dry nitrogen at a rate of 4l/min. The nitrogen was introduced into the chamber through a 0.25 inch tube which abutted the chamber normal to the surface at half height. There was a gap of 2mm between the base plate of the spinneret and the top of the forced convection chamber and a gap of 2mm between the bottom of the chamber and the surface of the water in the coagulation tank.

Both coagulation tanks were filled with pure water. The first tank was maintained at 14°C by an external cooling unit and the second tank was at room temperature. The bore fluid used was a 20% w/w aqueous potassium acetate solution at room temperature. This gives a water activity of 0.9 for the bore coagulant [68]. The water activity is lowered in the bore to slow down the speed of coagulation from the bore.

Previous work has demonstrated the effect of lowering the water activity of the bore [80]. The bore fluid was injected using a syringe pump, this provides an accurate and pulse free flow of bore fluid. The bore coagulant was injected in a ratio of 1:3 with the polymer dope. This meant that there was no ballooning or contracting of the fibre as the ratio of flow area of the annulus to the flow area of the needle was approximately 3:1.

The fibres were spun in two campaigns. The first campaign kept dope extrusion rate constant but varied residence time in the air gap, by varying the length of the forced convection chamber. The second campaign varied dope extrusion rate and so the level of extrusion shear while keeping residence time in the air gap constant by altering the length of the forced convection chamber. The jet stretch ratio in both campaigns was kept constant at 1 throughout. The fabrication conditions of both campaigns are summarised below in tables 3.1 and 3.2.

Table 3.1 Spin Campaign 1

Run	Dope extrusion rate (cm^3/min)	Air gap height (cm)	Air gap residence time (s)
1.1	2.5	5	0.237
1.2	2.5	9	0.426
1.3	2.5	15	0.710
1.4	2.5	20	0.947

Table 3.2 Spin Campaign 2

Run	Dope extrusion rate (cm^3/min)	Air gap height (cm)	Air gap residence time (s)
2.1	0.833	5	0.710
2.2	1.5	9	0.710
2.3	2.5	15	0.710
2.4	3.333	20	0.710

Air gap residence time is worked out by first working out the linear velocity (d.e.r./flow area) and then dividing the length of the air gap by the linear velocity.

3.3 Results

3.3.1 Rheology

Previous work on the 22% polymer spinning dope had suggested that it was a shear thinning power law fluid with a power law index of 0.693 and a power law constant of 43.1 ($Pa.s^n$) [117]. However in recent work on a more sensitive rheometer with an advanced solvent trap preventing volatile solvent loss these values were found to be different. The difference was partly due to solvent loss but also due to sample loss, as the high shear rates require high rotational speeds. The sample loss was noticed as a negative normal force was registered at high rotational speeds. This was confirmed using an optical shear cell.

The latest results report a power law index of 0.925 and a power law constant of 2.06 ($Pa.s^n$) [87]. Using these results in a flow profile solver described by Shilton [89], shear conditions throughout the fibre cross section are solved and the shear rate at the outer wall of the annulus (the membrane active layer) can be calculated. These are given for the two campaigns in tables 3.3 and 3.4 below.

Table 3.3 Campaign 1. Extrusion Shear

Run	Dope Extrusion Rate (cm^3/min)	Shear at Wall (1/s)
1.1	2.5	8838
1.2	2.5	8838
1.3	2.5	8838
1.4	2.5	8838

Table 3.4 Campaign 2 Extrusion Shear

Run	Dope Extrusion Rate (cm^3/min)	Shear at Wall (1/s)
2.1	0.833	2945
2.2	1.5	5303
2.3	2.5	8838
2.4	3.33	11772

3.3.2 Gas Permeation Testing

The membranes produced were potted into modules as described. Due to the delicate nature of the fibres they were potted individually. This meant that any damaged fibres could be spotted quickly and discarded. In a bundle of 3 or more fibres the effect of a broken fibre will be masked.

3.3.2.1 Uncoated

The membranes produced in this study were found to have no significant pores even at 10000x magnification. The membranes produced also exhibit above intrinsic selectivities after coating, this makes any attempt at resistance modelling the coated membranes worthless. The above intrinsic selectivity suggests that all the gas flows through solid polymer and there are no pores present. The uncoated data contradicts this.

The fibres were potted as individual threads and then tested with four gases, O_2, N_2, CH_4 and CO_2. The permeability of the gases was calculated from the flow of gas and the membrane surface area. The gases were considered in two pairs, O_2/N_2 and

CH_4/CO_2. The model considered the uncoated membranes and the two flow mechanisms encountered: Knudsen diffusion and solution diffusion. Tables 3.5 and 3.6 below show the uncoated permeabilities.

Table 3.5 Campaign 1: Uncoated permeation data

Run	Dry gap residence time (s)	Shear at wall (1/s)	P O_2	P N_2	P CH_4	P CO_2	Ω (O_2/N_2)	Ω (CO_2/CH_4)
1.1	0.237	8838	109.95	111.68	160.41	136.69	0.99	0.87
1.2	0.426	8838	15.13	7.84	9.78	56.49	2.06	6.49
1.3	0.710	8838	38.12	32.20	43.75	80.78	1.27	2.18
1.4	0.947	8838	35.17	26.62	35.28	84.62	1.33	2.43

Table 3.6 Campaign 2: Uncoated permeation data

Run	Dry gap residence time (s)	Shear at wall (1/s)	P O_2	P N_2	P CH_4	P CO_2	Ω (O_2/N_2)	Ω (CO_2/CH_4)
2.1	0.710	2945	4.91	2.65	3.77	15.21	2.50	6.69
2.2	0.710	5303	15.18	12.90	18.07	30.93	1.27	2.10
2.3	0.710	8838	38.12	32.20	43.75	80.78	1.27	2.18
2.4	0.710	11772	94.02	93.19	129.02	77.39	1.07	0.87

P= Pressure normalised flux x 10^6 [cm^3(stp)/(s cm^2 cmHg)], measured at 25°C and at a pressure differential of 5 bar.

SEM analysis showed no visible pores on the surface even at 10000 x magnification. This suggests that the pore radius is no greater than 100Å. Therefore it is reasonable to ignore any contribution from viscous flow as even at a pore radius of 300 Å the flow is 85% Knudsen diffusion [45]. The pore radius in the model was therefore considered to be 100 Å.

The permeation of a gas through a membrane can be described by the equation.

$$Q = PA\Delta p$$

The Knudsen and solution diffusion flow mechanisms can be represented by the permeability expressions

$$P_{solutiondiffusion} = \frac{P}{\lambda}$$

$$P_{Knudsendiffusion} = \frac{8}{3}\left(\frac{1}{2\pi RoTM}\right)^{\frac{1}{2}} r\frac{A_p}{\lambda}$$

The overall permeability of a gas was considered to be the sum of the two components.

$$Pi_{overall} = Pi_{solutiondiffusion} + Pi_{Knudsendiffusion}$$

or

$$P_{i\,overall} = \frac{\bar{P}_i}{\lambda} + \frac{8}{3}\left(\frac{1}{2\pi RoTM_i}\right)^{\frac{1}{2}} r\frac{A_p}{\lambda}$$

Two gases i and j are then considered and the permeability expressions are solved simultaneously to yield Ap the surface porosity and λ the skin thickness.

$$P_{i\,overall} = \frac{\bar{P}_i}{\lambda} + \frac{8}{3}\left(\frac{1}{2\pi RoTM_i}\right)^{\frac{1}{2}} r\frac{A_p}{\lambda}$$

$$P_{j\,overall} = \frac{\bar{P}_j}{\lambda} + \frac{8}{3}\left(\frac{1}{2\pi RoTMj}\right)^{\frac{1}{2}} r\frac{A_p}{\lambda}$$

The pore radius is fixed at 100 Å and the molecular weight, temperature and gas constant are entered. The simultaneous permeability equations were then solved using the computer program Mathcad by inputting the uncoated gas pressure

normalised fluxes to yield the skin thickness and surface porosity. An average value for skin thickness and porosity was then calculated from the two models (O_2/N_2 and CH_4/CO_2). Six results were used from each category to give an average value.

Campaign 1: Varying Residence Time

Table 3.7 Campaign 1: Skin thickness and surface porosity

Run	Air Gap length (cm)	Air Gap residence time (s)	Dope Extrusion rate (cm^3/min)	Shear at wall (1/s)	Skin Thickness (Å)	Surface Porosity (m^2/m^2)
1.1	5	0.237	2.5	8838	1450	4.00×10^{-6}
1.2	9	0.426	2.5	8838	1023.5	1.54×10^{-7}
1.3	15	0.710	2.5	8838	997	7.66×10^{-7}
1.4	20	0.947	2.5	8838	707.5	4.685×10^{-7}

Campaign 2: Varying Extrusion Shear

Table 3.8 Campaign 2: Skin thickness and surface porosity

Run	Air Gap length (cm)	Air Gap Residence Time (s)	Dope Extrusion rate (cm^3/min)	Shear at wall (1/s)	Skin Thickness (Å)	Surface Porosity (m^2/m^2)
2.1	5	0.710	0.833	2945	3665	2.22×10^{-7}
2.2	9	0.710	1.5	5303	2890	1.56×10^{-6}
2.3	15	0.710	2.5	8838	997	7.66×10^{-7}
2.4	20	0.710	3.33	11772	392.5	3.61×10^{-6}

3.3.2.2 Coated Results

The fibres were potted individually into modules and then silicone coated to repair any surface defects. The modules were then tested on the multi-chamber rig with the four gases; O_2, N_2, CO_2 and CH_4.

The pressure-normalised flux (P/λ) is determined from

$$\left(\frac{P}{\lambda}\right)_i = \frac{Q_i}{A\Delta p}$$

The flow of gas was measured using bubble flowmeters and the membrane area was measured directly.

The selectivity is determined from

$$\Omega_j^i = \frac{\left(\frac{P}{\lambda}\right)_i}{\left(\frac{P}{\lambda}\right)_j}$$

The apparent skin thickness was calculated using the pressure-normalised flux, the intrinsic permeability of the gas/polymer pairing and the surface area of the fibre. The calculation of an apparent skin thickness is only justified if the fibres exhibit 80% of the intrinsic selectivity [64], any less than 80% and the gas passing through the pores must be taken into account. The diameter of the fibre was obtained using an optical microscope fitted with a graticule and the length was obtained using a ruler. The apparent wall thickness is an average value obtained from all four gases.

The results for the coated work are given below in Tables 3.9 and 3.10.

Campaign 1: Varying Residence Time

Table 3.9 Campaign 1: Gas permeabilities and selectivites

Run	Air Gap Residence time (s)	Shear at wall (1/s)	P O_2	P N_2	P CO_2	P CH_4	Ω (O_2/N_2)	Ω (CO_2/CH_4)	Apparent wall Thickness Å
1.1	0.237	8838	10.6	1.81	82.2	2.40	6.38	36.8	848
1.2	0.426	8838	10.1	1.50	58.2	1.54	7.46	40.1	1070
1.3	0.710	8838	11.8	1.68	89.0	2.27	7.01	39.5	794
1.4	0.947	8838	15.2	2.96	84.4	3.76	5.30	26.3	590

Campaign 2: Varying Extrusion Shear

Table 3.10 Campaign 2: Gas permeabilities and selectivities

Run	Air Gap Residence Time (s)	Shear at wall (1/s)	P O_2	P N_2	P CO_2	P CH_4	Ω (O_2/N_2)	Ω (CO_2/CH_4)	Apparent wall thickness Å
2.1	0.710	2945	2.99	0.797	16.0	0.851	4.08	23.4	2809
2.2	0.710	5303	3.51	0.849	19.3	1.00	4.79	25.5	2459
2.3	0.710	8838	11.8	1.68	89.0	2.27	7.01	39.5	794
2.4	0.710	11772	16.3	7.31	61.9	8.73	2.94	12.0	N/A

P= Pressure normalised flux x 10^6 [cm^3(stp)/(s cm^2 cmHg)], measured at 25°C and at a pressure differential of 5 bar.

3.3.3 Fibre Mechanical Strength

The fibres were tested on an Instron machine. The results are an average of 6 fibres tested.

Campaign 1: Varying Residence Time

Table 3.11 Campaign 1: Fibre tensile properties

Run	Extrusion Rate (cm^3/min)	Air Gap Residence time (s)	Max % Strain	% Strain at Break	Max Tenacity (N/tex)	Tenacity at Break (N/tex)	1st Modulus (N/tex)	2nd Modulus (N/tex)
1.1	2.5	0.237	47.81	48.03	0.0229	0.0225	0.6963	0.0147
1.2	2.5	0.426	53.96	54.26	0.0223	0.0218	0.6451	0.0145
1.3	2.5	0.710	50.28	50.66	0.0242	0.0239	0.723	0.0157
1.4	2.5	0.947	55.67	55.7	0.0227	0.0223	0.6407	0.0145

Campaign 2: Varying Extrusion Shear

Table 3.12 Campaign 2: Fibre tensile properties

Run	Extrusion Rate (cm^3/min)	Air gap residence time (s)	Max % Strain	% Strain at break	Max Tenacity (N/tex)	Tenacity at break (N/tex)	1st Modulus (N/tex)	2nd Modulus (N/tex)
2.1	0.833	0.710	50.22	50.74	0.0254	0.0253	0.8541	0.0125
2.2	1.5	0.710	49.46	50.13	0.0247	0.0247	0.8504	0.0143
2.3	2.5	0.710	50.28	50.66	0.0242	0.0239	0.723	0.0157
2.4	3.33	0.710	47.46	47.51	0.0234	0.0234	0.762	0.0155

3.4 Electron Microscopy

The fibres produced from the 22% polymer dope were analysed on a JEOL scanning electron microscope, model 840 A. The samples were cut with a fresh razor and mounted on sample stubs before being sputter coated with gold.

The photos were taken with a SLR camera and are shown below.

Fig 3.1 Fibres Produced with Varying Residence Time

DER 2.5 cm^3/min
Residence Time 0.237 s

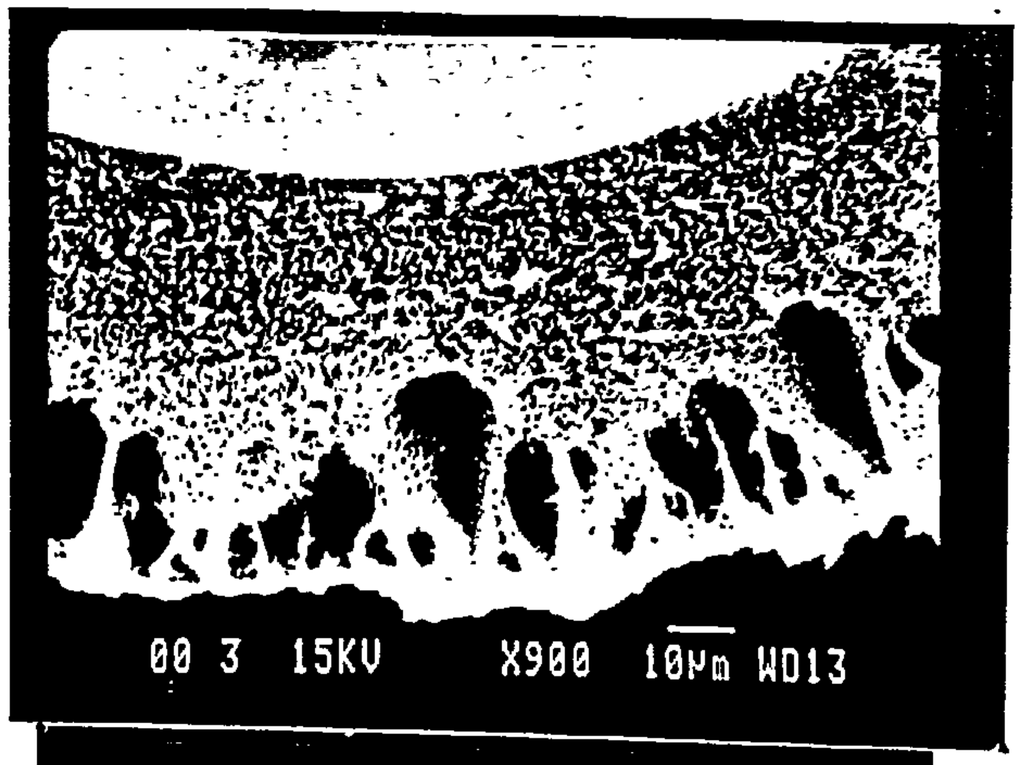

DER 2.5 cm^3/min
Residence Time 0.426 s

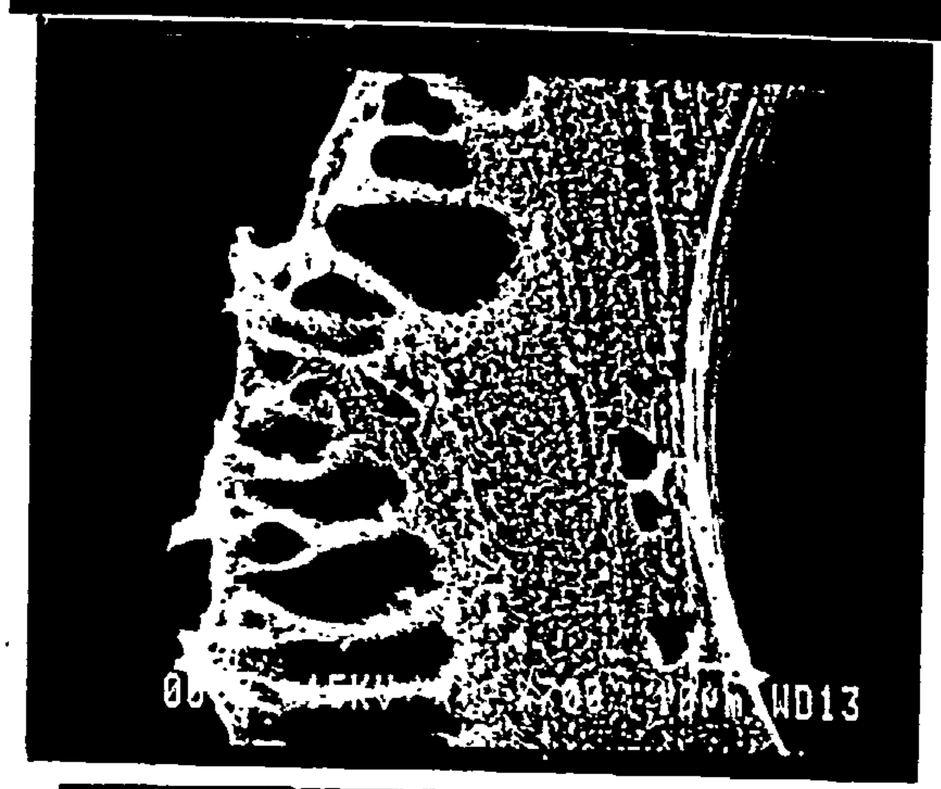

DER 2.5 cm^3/min
Residence Time 0.710 s

DER 2.5 cm^3/min
Residence Time 0.947 s

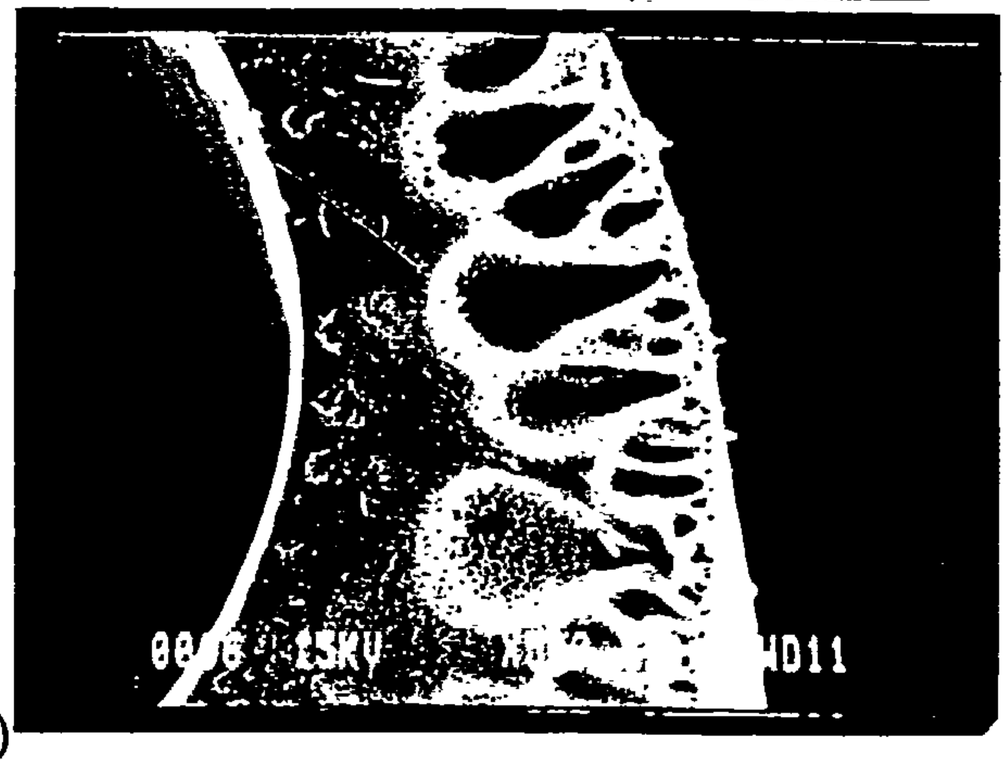

(Extrusion Shear is 8838 1/s Throughout)

Fig 3.2 Fibres Produced at Varying Extrusion Shear

DER 0.833 cm^3/min
Extrusion Shear 2948 1/s

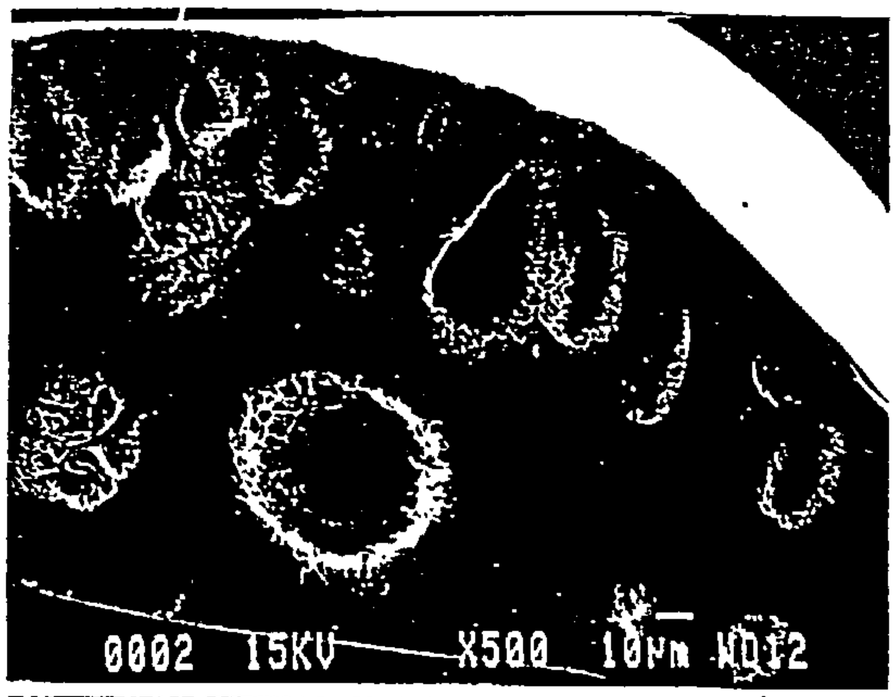

DER 1.5 cm^3/min
Extrusion Shear 5303 1/s

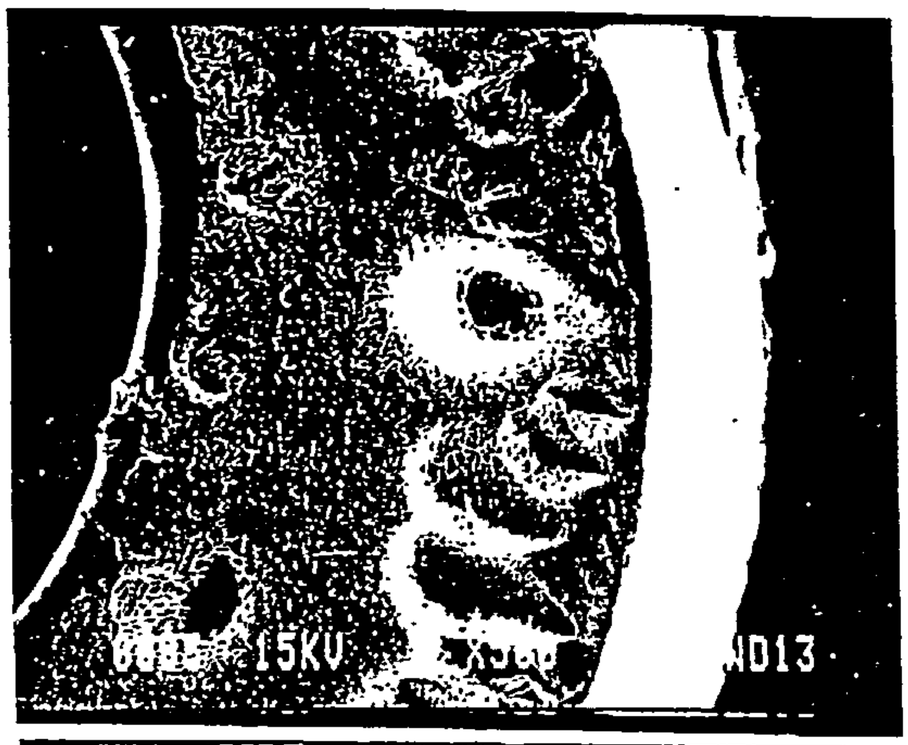

DER 2.5 cm^3/min
Extrusion Shear 8838 1/s

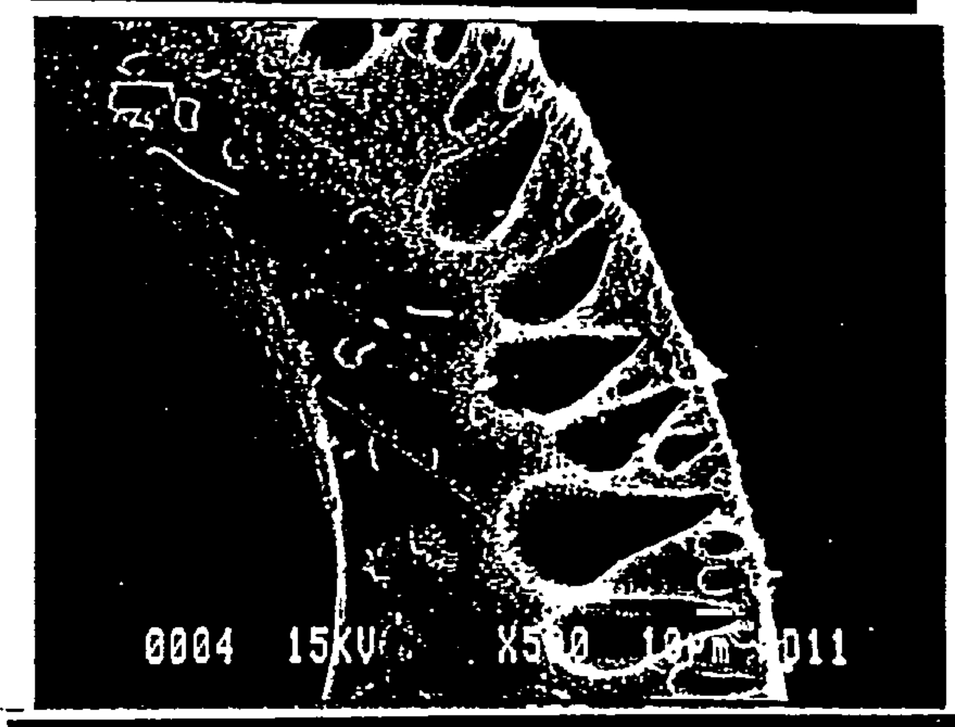

DER 3.33 cm^3/min
Extrusion Shear 11772 1/s

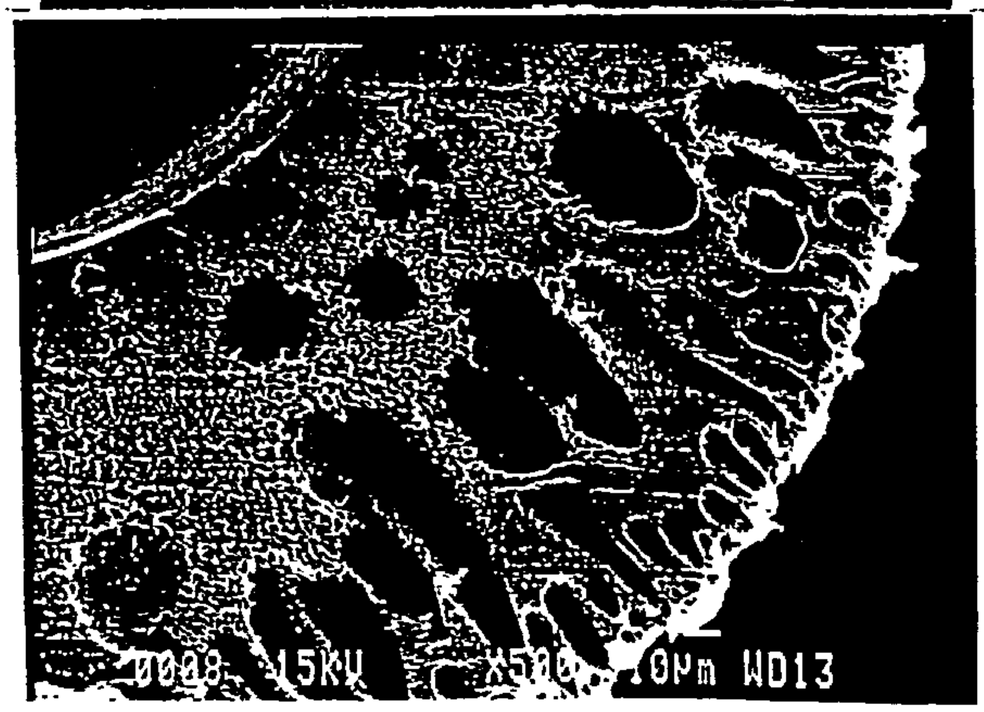

(Residence Time Fixed at 0.710 s)

3.5 Discussion of Results

3.5.1 Fibres Spun With Varying Residence Time

Uncoated Data

The uncoated results are used to give an idea of the physical characteristics of the fibres. The uncoated results give an idea of the thickness of the active layer and the surface porosity. These results provide a more complete understanding than a skin thickness calculated from any coated data as the coated data takes no account of surface porosity.

The results are quite interesting. At the shortest air gap (0.237s) the skin is at it's thickest but most porous. This suggests that the skin has not yet coalesced properly. Brown in work on latex coalescence and Koros and Pinnau on their work on skin formation suggested that circular nodules coalescing due to capillary pressure could form a thin defect free skin [69,70]. The nodules are formed as a result of the spinodal phase separation at the surface of the fibre due to solvent evaporation. The phase separated regions coarsen due to surface tension effects and eventually the polymer rich regions fuse under the action of the capillary pressure at the fibre gas interface.

At the next air gap (0.426s) the skin has become significantly thinner but also much less porous. This suggests that the skin has now formed completely and that coalescence has finished.

When the air gap is increased again (0.710s) the porosity increases and the skin becomes slightly thinner. The thinning of the skin is possibly due to the re-dissolution of the back of the skin into the bulk of the fibre, which has not yet solidified. The increase in porosity is possibly due to the coagulation front moving from the bore out through the fibre affecting the skin formation process at the surface of the fibre.

At the longest air gap (0.947s) the skin has become thinner still but the porosity decreases slightly. The thinner skin is in line with the trend but the decrease in porosity is unexpected. There is an explanation for the drop in porosity and that is that some of the fibres tested for the 0.710s air gap were defective. When testing uncoated fibres they are all essentially defective, however after coating some fibres still display defects due to handling or damage during potting. After coating these are easily spotted and the results discarded. However when testing the fibres uncoated it is more difficult to identify defective fibres during testing. Once the models have been solved the defective fibres can be seen. The results for the fibres spun at the 0.710s air gap show more scatter than the other categories which suggests the presence of defective fibres (see appendix 1 p186). The results after coating also support this suggestion.

Coated Data

The coated permeation results give the performance of the membranes for gas separation. The results can also be used to work out an apparent skin thickness. The

apparent skin thickness does not however take into account gas transmission through pores so gives a thinner calculated skin thickness.

The gas separation properties of the membranes are very impressive. The 3 membrane types spun at 0.237,0.426 and 0.710s air gaps all display above the intrinsic selectivity for the O_2/N_2 and CO_2/CH_4 separations. The higher than expected selectivities have been recorded before and have been attributed to increased molecular orientation in the active layer [80].

At the 0.237s air gap the fibres exhibit a high permeability and high selectivity. This gives a thin apparent skin thickness (848 Å). The higher permeability and therefore thin skin could be due to flow through pores and would explain the difference between the coated and uncoated results. It is also possible that the polymer matrix is more permeable before it has coalesced and this explains the difference between the coated and uncoated results. The high selectivity despite the pores could be due to increased molecular orientation in the membrane active layer.

At the 0.426s air gap the permeability drops and the selectivity increases. This gives an apparent skin thickness of 1070 Å, which is very similar to the value from the uncoated modelling. The rise in selectivity also suggests a fall in surface porosity and this is the same trend as the uncoated data.

As the air gap increase to 0.710s the permeability rises and the selectivity falls suggesting the skin becomes thinner and more defective. The apparent skin thickness calculated is 794 Å, which supports this. This also agrees with the uncoated results.

At the highest residence time and longest air gap (0.947s) the permeability rises further still and the selectivity falls. This suggests the skin has become thinner and more defective. The apparent skin thickness calculated was 590 Å. This also supports the suggestion that some of the fibres used for the uncoated modelling for the 0.710s air gap were defective. The fall in selectivity as the air gap is increased from 0.710 to 0.947s suggests that the 0.947s fibres are more defective and not less defective as the uncoated data suggests. The thinning of the active layer is possibly due to the redissolution of the active layer into the bulk of the fibre. The increase in porosity could be due to the advancing internal coagulation front affecting the skin formation.

The results suggest that the active layer of the membrane is formed in the air gap during extrusion. It is not formed immediately but takes some time to form. After it has formed it can be damaged by the coagulation front advancing from the lumen of the fibre at longer residence times. This is in agreement with work by Wang et al [116].

Instron Data

The instron results for varying air gap residence time show no significant trends. Although the active layer changes in the air gap the bulk of the fibre is formed by a combination of coagulation from the lumen and coagulation in the first bath. The

active layer represents a tiny % of the bulk of the fibre so any subtle changes in the active layer are unlikely to be picked up by a bulk test. The linear density and external dimensions of the fibres are all very similar for the 4 categories so they all display similar mechanical properties.

SEM Data

The images in fig 3.1 from the electron microscopy do not show any significant trends as residence time is increased. The active layer is so thin that even at the greatest magnification it is impossible to detect. The general morphology of the fibres also does not change significantly as residence time is increased.

3.5.2 Fibres Spun With Varying Extrusion Shear

The effect of varying shear on the formation of the active layer is quite striking.

Uncoated Results

The uncoated results give an accurate insight into the thickness and porosity of the active layer.

At the lowest level of extrusion shear (2945 1/s) the skin is thickest and least porous. The skin is 3665 Å thick and the porosity is 2.22×10^{-7} m^2/m^2.

As the rate of shear increases to 5303 1/s the skin becomes thinner but more porous. The skin thickness decreases to 2890 Å but the porosity increases to 1.6×10^{-6}

m^2/m^2. This is quite a marked increase in porosity and again could be due to defective fibres, this will be discussed further with the coated results.

As the rate of shear increases from 5303 to 8838 1/s the skin thins dramatically. The active layer becomes 997 Å thick but the porosity decreases to 7.66×10^{-7} m^2/m^2. Finally as the rate of shear increases to 11772 1/s the skin thickness falls to 392.5 Å and the porosity increases to 3.61×10^{-6} m^2/m^2.

The effect of shear on the thickness of the active layer is quite obvious, increasing the level of extrusion shear results in thinning of the active layer. The effect of shear on porosity is less clear.

Coated Results

The coated results show similar trends to the uncoated data. At the lowest rate of shear the selectivity is low for both the O_2/N_2 and CO_2/CH_4 separations. The low selectivity suggests the presence of surface pores. The permeability is also low and this suggests a thick skin, the apparent skin thickness calculated is 2809 Å. The thick skin coupled with the presence of pores would lead to a low selectivity. The relative resistance of the thick skin forces more of the gas flow through the pores. This is in good agreement with the uncoated results.

As the rate of shear increases the skin becomes thinner. The apparent skin thickness as the rate of shear increases to 5303 1/s falls to 2459 Å. The selectivity also increases slightly for both the O_2/N_2 and CO_2/CH_4 separations. This suggests that the

porosity does not become significantly greater. The porosity could increase slightly as the relative resistance of the skin decreases as it becomes thinner so more gas would pass through the skin relative to the pores. However the uncoated data suggested a huge rise in porosity and this would not give the increase in selectivity seen. A more plausible suggestion is that some of the fibres tested for the uncoated results were damaged.

As the extrusion shear increases to 8838 1/s the apparent skin thickness decreases considerably to 794 Å. The selectivity for the O_2/N_2 and CO_2/CH_4 separations both rise to above the recognised intrinsic value for the polymer. This suggests that the skin has become much less porous, coupled with the low relative resistance of the skin this explains the rise in selectivity. Again this agrees well with the uncoated results. The low relative resistance of the skin means more gas flows through the polymer matrix. The fact that the selectivity rises above the intrinsic value suggests that the active layer has become oriented and thus exhibits superior properties to the isotropic polymer. This has been discussed before [78-80].

At the highest rate of extrusion shear (11772 1/s) the permeability of the membrane's rise considerably but the selectivity falls dramatically. The selectivity falls so far that an apparent skin thickness calculation cannot be justified. The low selectivity suggests that most of the gas is now passing through pores and not the polymer matrix. The low selectivity and the data for skin thickness and porosity from the uncoated data suggest that the skin has become so thin that any defects completely penetrate the skin and render it useless.

Instron Data

Again the instron results do not reveal any significant trends. Although there is a trend in both the maximum tenacity and tenacity at break categories these are dependent on the failure mechanism of the fibre. The 1st modulus which is a better indicator of structural differences shows no clear trend.

SEM Data

The SEM images in fig 3.2 show a change in morphology as extrusion shear is increased. The outer layer of the fibre is a thick dense layer at the lowest level of extrusion and the substructure has a few circular macrovoids. As the extrusion shear is increased the outer dense layer becomes thinner and the macrovoids become teardrop shaped. The active layer is however too thin to distinguish on the images.

3.6 Gas Mixture work.

To complement the pure gas studies a further campaign of work was carried out. The most selective category of fibres was analysed using gas mixture permeation testing. This category was the fibres extruded at 2.5 cm^3/min with an air gap of 9cm. The fibres were potted and coated as normal and fitted into the rig. They were then tested with two gas mixtures, a CO_2/CH_4 and O_2/N_2 mixture both approximately 50/50 mole % and supplied by BOC with certified compositions. The compositions were 49.8 / 50.2 mole % O_2/N_2 and 50.6 / 49.4 mole % CO_2/CH_4.

The permeate gas was analysed using a GC connected to a PC which had an integration package installed. The integration package gives the composition of the permeate gas in vol %. The vol % is equivalent to mole fraction and this can be used to calculate the selectivity of the membranes as follows.

$$\Omega_j^i = \frac{y_{ip}}{1-y_{ip}}\left(\frac{(1-y_{ir})p_r - (1-y_{ip})p_p}{y_{ir}p_r - y_{ip}p_p}\right)$$

The mole fraction of component i in the permeate stream is measured directly using the on line gas chromatograph, a simple mass balance then calculates the mole fraction of component i in the retentate stream. The concentration of component i in the module is taken as the average of the retentate and feed mole fractions. This is more precise than assuming the concentration in the chamber is the same as the feed concentration. This is an improvement on the well mixed model. The permeability of the gases is worked out using the concentrations of the permeate and feed streams. Once the mole fraction of the feed and permeate gases are used to work out the

concentrations in the module and the operating pressures (feed is at 6 bar, permeate at 1 bar) are plugged into the equation the selectivity can be calculated.

The permeability of the gas is calculated by multiplying the mole fraction by the total permeate flow rate to give a component permeate flow rate. This is then used in

$$\left(\frac{P}{\lambda}\right)_i = \frac{Q_i}{A\Delta p}$$

where Δp takes into account the partial pressures of the component to give the driving force.

3.6.1 Results

The six modules were tested and the results calculated. The average of the six modules is shown below.

Table 3.13 Gas mixture permeation results

Campaign	% O_2 in Permeate	P O_2	P N_2	Ω (O_2/N_2)	% CO_2 in permeate	P CO_2	P CH_4	Ω (CO_2/CH_4)
1.2	83.15	10.1	1.43	7.08	96.31	59.5	1.45	41.70

P= Pressure normalised flux x 10^6 [cm^3(stp)/(s cm^2 cmHg)], measured at 25°C and at a pressure differential of 5 bar.

3.6.2 Discussion

The results show that there is not a great deal of difference between the results obtained using pure gases and gas mixtures. The selectivity for the O_2/N_2 separation is slightly lower than the value obtained using pure gases and the selectivity for the CO_2/CH_4 is slightly higher than the value obtained using pure gases. The

permeabilities of the slow gases also decrease slightly but again the differences are minimal. This suggests that as the membranes absorb the gases there is not an appreciable alteration in the structure and the selective mechanism is not altered by the presence of two types of penetrants.

Chapter 4:

Spinning Industrial Membranes

4.1 Introduction

Although the fibres spun from the 22% polymer dope can exhibit extremely high selectivities and fluxes they are mechanically weak. The fibres are fragile and easily damaged. In an industrial environment operating pressures are higher and a more robust fibre is required. To pot fibres in bundles of 10^5 fibres requires a degree of handling and so the fibres must be durable.

In order to produce tougher more durable membranes that would survive in an industrial environment a second campaign of work was undertaken. In order to improve the mechanical strength of the fibres the polymer content of the fibres was increased. A 40% multi-component dope developed by Koros et al was utilised [68]. The dope composition is 40% w/w Polysulphone, 35.7% w/w DMAc, 11.9% w/w THF and 12.4% w/w EtOH. The dope components have the same purpose in the dope as in the 22% Psf dope but are in different proportion. The DMAc is the base solvent the THF is the volatile solvent and the EtOH is added to make the dope unstable.

An analogous spinning campaign was carried out to the one for the first phase of work. One spinning campaign was carried out at constant shear while residence time was varied and the other at constant residence time while extrusion shear was varied.

The 40% Psf dope was found to be unworkable at room temperature. The delivery lines failed under the pressure developed in the system. In order to lower the viscosity of the polymer dope the fibres were spun at an elevated temperature of

50°C. This presented a challenge and the spin line had to modified to extrude the fibres at increased temperatures without compromising safety. The dope pot was kept in a water bath and a heat exchanger was introduced into the polymer delivery line. The gear pump and spinneret were heated by hot air blowers and the spinneret was modified so a thermocouple could be inserted to measure the temperature of the dope as it was spun.

Fig 4.1 Modified extrusion system

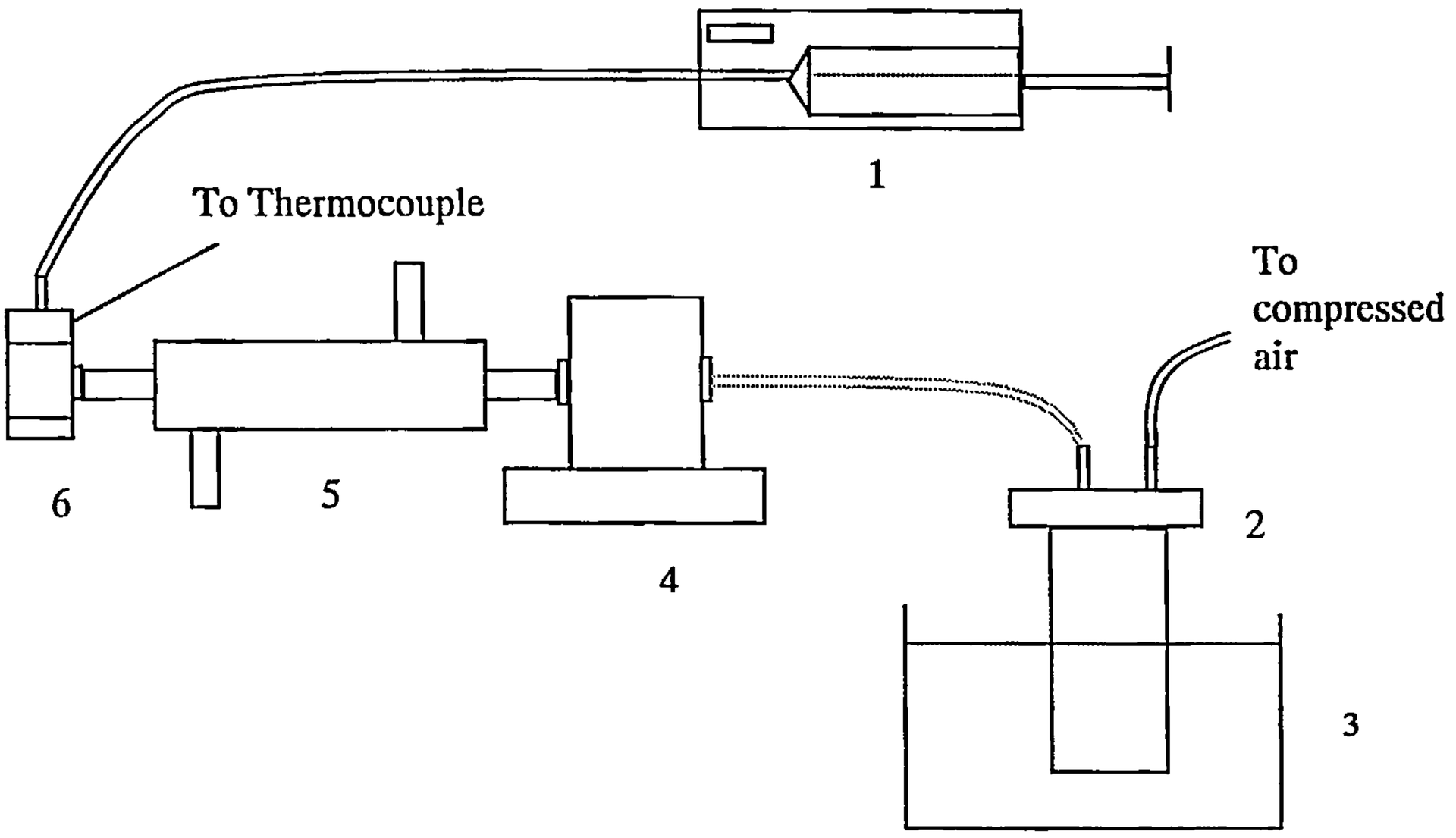

1. Syringe pump
2. Dope Pot
3. Heated Water Bath
4. Metering gear pump
5. Heat Exchanger
6. Spinneret

The two spinning campaigns are summarised in the tables 4.1 and 4.2 below.

Table 4.1 Spin Campaign 3

Run	Dope extrusion rate (cm^3/min)	Air gap height (cm)	Air gap residence time (s)
3.1	2.5	5	0.237
3.2	2.5	9	0.426
3.3	2.5	15	0.710
3.4	2.5	20	0.947

Table 4.2 Spin Campaign 4

Run	Dope extrusion rate (cm^3/min)	Air gap height (cm)	Air gap residence time (s)
4.1	0.833	5	0.710
4.2	1.5	9	0.710
4.3	2.5	15	0.710
4.4	3.33	20	0.710

4.2 Results

4.2.1 Rheology

The modified dope was analysed using the T.A. Instruments AR 1000 rotational rheometer. The dope was analysed at 50°C to reproduce the spinning conditions. The dope was found to be shear thinning with a power law index of 0.8352 and a power law constant of 120.4. This shows that the more concentrated dope is considerably more viscous and also more shear thinning than the 22% dope (c.f. page 89).

The different spinning campaigns were modelled using the flow profile software and the results are given below in tables 4.3 and 4.4.

Table 4.3 Campaign 3: Extrusion Shear

Run	Dope Extrusion Rate (cm^3/min)	Shear at wall (1/s)
3.1	2.5	9118
3.2	2.5	9118
3.3	2.5	9118
3.3	2.5	9118

Table 4.4 Campaign 4: Extrusion shear

Run	Dope Extrusion Rate (cm^3/min)	Shear at wall (1/s)
4.1	0.833	3038
4.2	1.5	5471
4.3	2.5	9118
4.2	3.33	12162

4.2.2 Gas Permeation Tests

The membranes were potted into modules as described in the experimental methods section and coated as necessary. After preliminary single filament testing the fibres were potted in bundles of 3 fibres. This was due to the low permeability of the fibres making flow measurements from single fibres very difficult and time consuming.

4.2.2.1 Uncoated

The membranes were potted in bundles of three fibres and then tested with four gases, O_2, N_2, CH_4 and CO_2. The results of the gas testing are given in Tables 4.5 and 4.6 below. The gases were again considered in two pairs and the permeability of the respective gases was then used in the two models to calculate skin thickness and the surface porosity of the fibres. The models were the same as those described in chapter 3. An average value was then taken from the two models for both surface porosity and skin thickness. Six results were used from each category to give an average value. The results of the modelling are shown in Tables 4.7 and 4.8 below.

Table 4.5: Campaign 3 Uncoated Permeability data

Run	Air Gap Residence Time (s)	Shear at Wall (1/s)	P O_2	P N_2	P CH_4	P CO_2	Ω (O_2/N_2)	Ω (CO_2/CH_4)
3.1	0.237	9118	1.233	0.648	0.925	3.839	2.321	4.755
3.2	0.426	9118	0.632	0.222	0.261	2.023	2.877	7.854
3.3	0.710	9118	0.514	0.155	0.114	1.901	3.336	16.702
3.4	0.947	9118	0.766	0.150	0.147	2.891	5.161	19.711

Table 4.6 Campaign 4: Uncoated Permeability data

Run	Air Gap Residence Time (s)	Shear at Wall (1/s)	P O_2	P N_2	P CH_4	P CO_2	Ω (O_2/N_2)	Ω (CO_2/CH_4)
4.1	0.710	3038	1.221	0.308	0.293	5.057	4.003	17.876
4.2	0.710	5471	1.251	0.312	0.296	5.116	4.045	17.809
4.3	0.710	9118	0.514	0.155	0.114	1.901	3.336	16.702
4.4	0.710	12162	0.996	0.250	0.220	3.187	4.078	14.839

P= Pressure normalised flux x 10^6 [cm^3(stp)/(s cm^2 cmHg)], measured at 25°C and at a pressure differential of 5 bar.

Campaign 3: Varying Residence Time

Table 4.7 Campaign 3: Skin thickness and surface porosity

Run	Air Gap length (cm)	Air Gap Residence time (s)	Dope Extrusion Rate (cm^3/min)	Shear at wall (1/s)	Skin Thickness (Å)	Surface Porosity (cm^2/cm^2)
3.1	5	0.237	2.5	9118	15500	2.34×10^{-7}
3.2	9	0.426	2.5	9118	22500	7.7×10^{-8}
3.3	15	0.710	2.5	9118	24300	3.52×10^{-8}
3.4	20	0.947	2.5	9118	15100	1.165×10^{-8}

Campaign 4: Varying Extrusion Shear

Table 4.8 Campaign 4: Skin Thickness and porosity

Run	Air Gap length (cm)	Air Gap residence time (s)	Dope Extrusion Rate (cm^3/min)	Shear at wall (1/s)	Skin thickness (Å)	Surface Porosity ($cm^2/^2$)
4.1	5	0.710	0.833	3038	9380	2.385×10^{-8}
4.2	9	0.710	1.5	5471	9170	2.405×10^{-8}
4.3	15	0.710	2.5	9118	24300	3.52×10^{-8}
4.4	20	0.710	3.33	12162	13250	2.99×10^{-8}

4.2.2.2. Coated Results

The fibres were again potted in bundles of 3 and then silicone coated. The fibres were then tested with the four gases, O_2, N_2, CH_4 and CO_2. The permeability and selectivity were calculated as described in chapter 3.

Campaign 3: Varying Residence Time

Table 4.9 Campaign 3: Gas permeabilities and selectivities

Run	Air Gap Residence Time (s)	Shear at wall (1/s)	P O_2	P N_2	P CH_4	P CO_2	Ω (O_2/N_2)	Ω (CO_2/CH_4)	Apparent Wall Thickness (Å)
3.1	0.237	9118	1.00	0.22	0.24	3.07	4.59	13.39	N/A
3.2	0.426	9118	0.75	0.21	0.21	2.55	3.55	12.31	N/A
3.3	0.710	9118	0.59	0.16	0.15	2.19	3.62	14.58	N/A
3.4	0.947	9118	0.72	0.15	0.14	2.54	4.74	18.01	N/A

Campaign 4: Varying Extrusion Shear

Table 4.10 Campaign 4: Gas permeabilities and selectivities

Run	Air Gap Residence Time (s)	Shear at wall (1/s)	P O_2	P N_2	P CH_4	P CO_2	Ω (O_2/N_2)	Ω (CO_2/CH_4)	Apparent Wall Thickness (Å)
4.1	0.710	3038	1.07	0.17	0.19	4.45	6.27	23.15	9650
4.2	0.710	5471	0.99	0.18	0.17	4.40	5.57	25.12	10228
4.3	0.710	9118	0.59	0.16	0.15	2.19	3.61	14.58	N/A
4.4	0.710	12162	0.91	0.19	0.17	3.15	4.78	18.28	N/A

P= Pressure normalised flux x 10^6 [cm^3(stp)/(s cm^2 cmHg)], measured at 25°C and at a pressure differential of 5 bar.

4.2.3 Fibre Mechanical Strength

The fibres were again examined on an Instron machine. The results are an average taken from 6 fibres.

Campaign 3: Varying Residence Time

Table 4.11 Campaign 3: Fibre tensile properties

Run	Extrusion Rate (cm^3/min)	Air Gap Residence time (s)	Max % Strain	% Strain at Break	Max Tenacity (N/tex)	Tenacity at break (N/tex)	1st Modulus (N/tex)	2nd Modulus (N/tex)
3.1	2.5	0.237	57.94	58.47	0.0284	0.0282	1.0031	0.0115
3.2	2.5	0.426	51.69	51.90	0.0284	0.0278	1.0164	0.0120
3.3	2.5	0.710	55.86	56.63	0.0283	0.0280	1.0124	0.0121
3.4	2.5	0.947	68.37	68.53	0.0286	0.0282	0.8979	0.0102

Campaign 4: Varying Extrusion Shear

Table 4.12 Campaign 4: Fibre tensile properties

Run	Extrusion Rate (cm^3/min)	Air Gap Residence time (s)	Max % Strain	% Strain at Break	Max Tenacity (N/tex)	Tenacity at break (N/tex)	1st Modulus (N/tex)	2nd Modulus (N/tex)
4.1	0.833	0.710	42.15	42.67	0.0269	0.0266	0.9127	0.0104
4.2	1.5	0.710	59.89	60.57	0.0285	0.0280	0.8905	0.0106
4.3	2.5	0.710	55.86	56.63	0.0283	0.0280	1.0124	0.0121
4.4	3.33	0.710	59.40	59.53	0.0304	0.0299	1.088	0.0101

4.3 SEM Images

The fibres were mounted on stubs and coated as described in chapter 3. They were analysed on a Hitachi scanning electron microscope with a computer graphics package. The images produced are displayed below in figures 4.2 and 4.3.

Fig 4.2 Fibres produced at varying residence time.

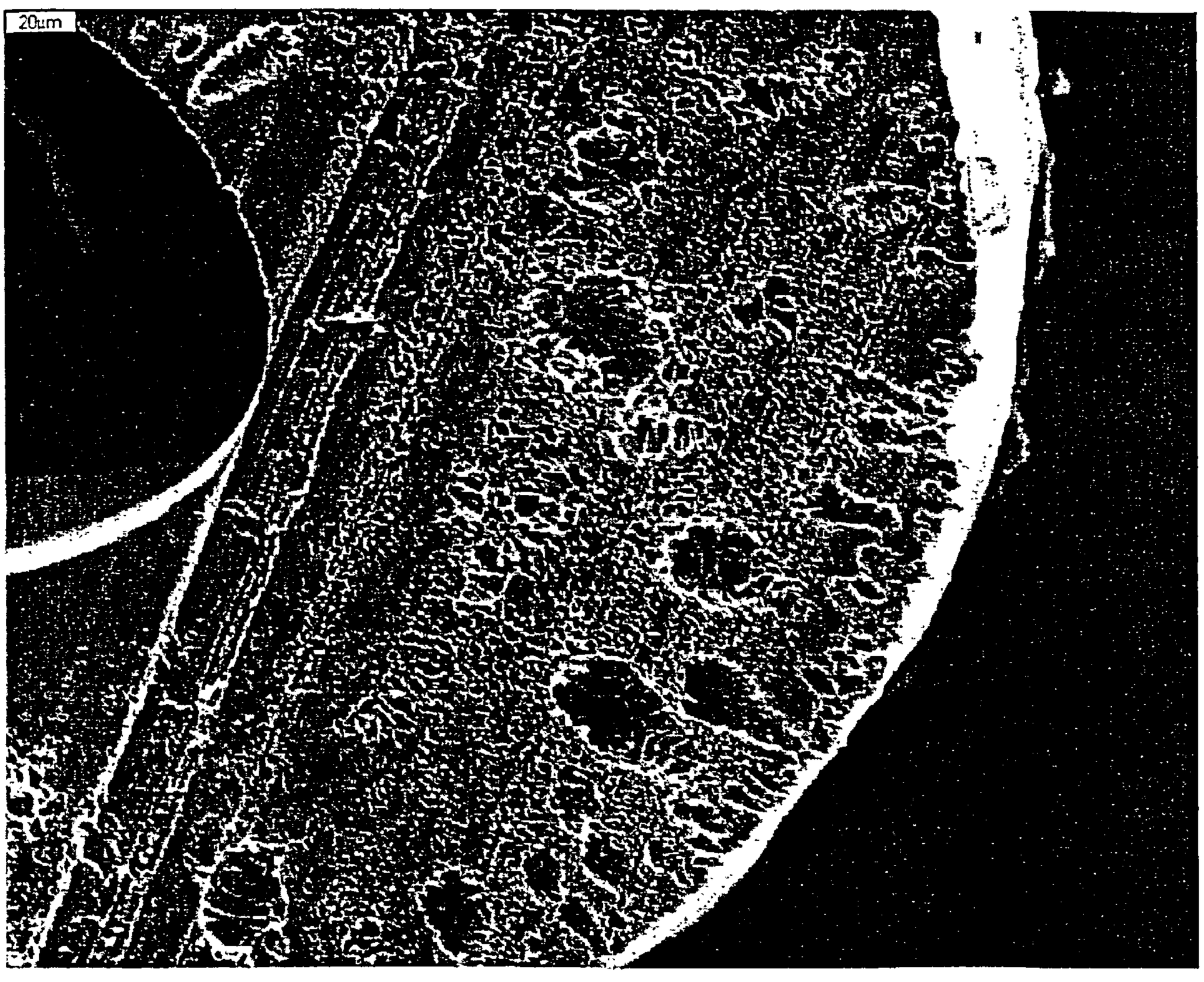

DER 2.5 cm^3/min
Residence Time 0.237 s

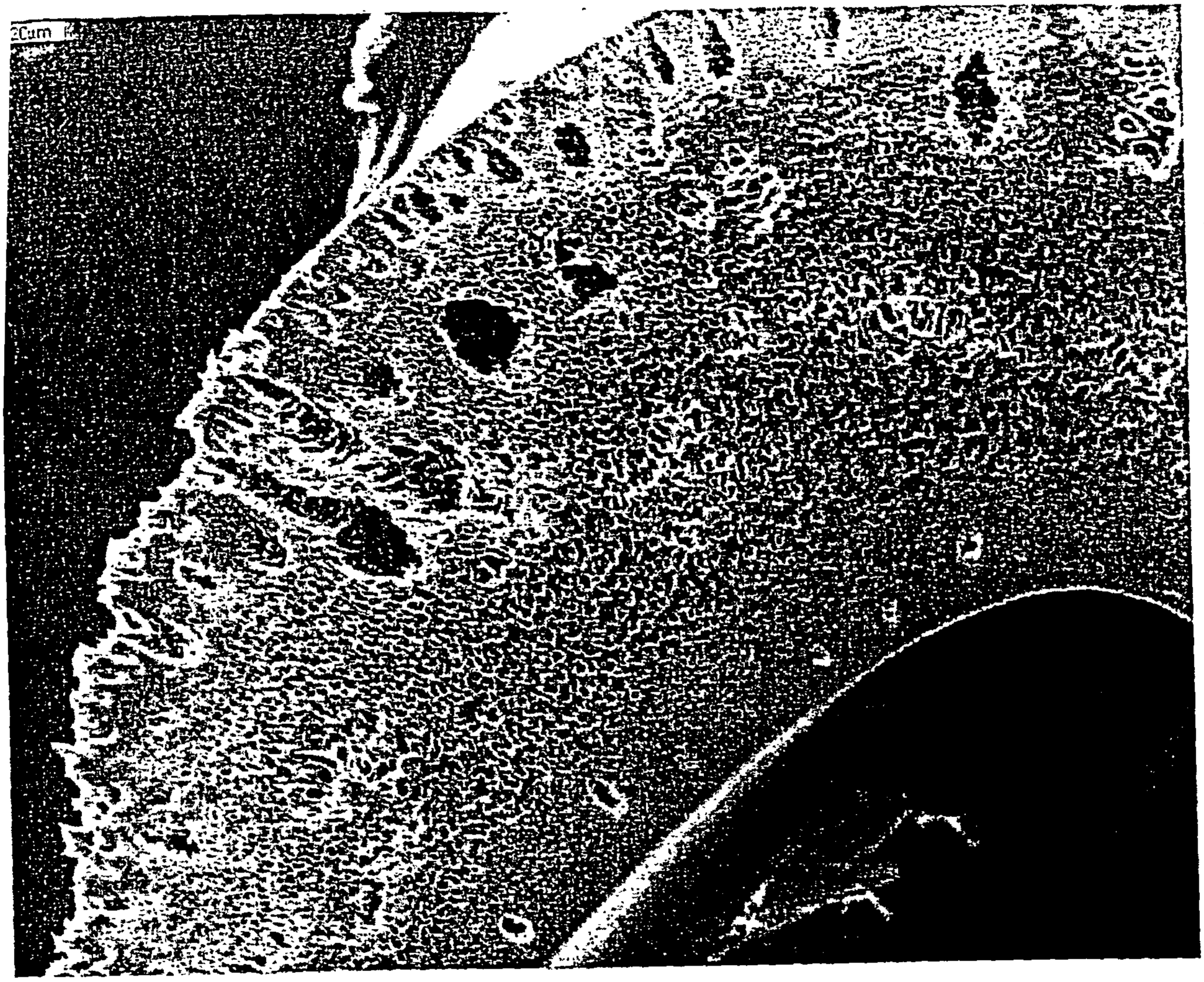

DER 2.5 cm^3/min
Residence Time 0.426 s

DER 2.5 cm^3/min
Residence Time 0.710 s

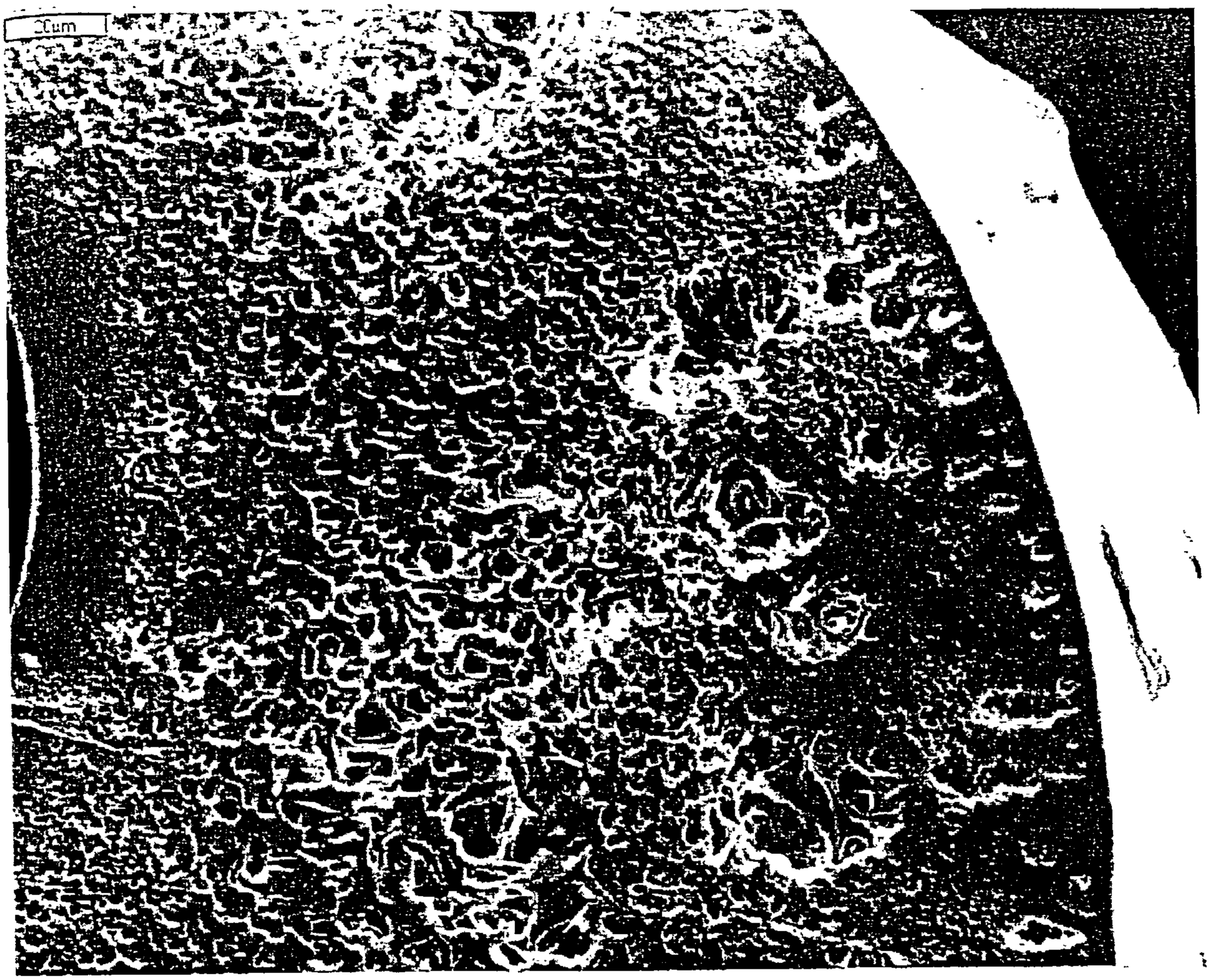

DER 2.5 cm^3/min
Residence Time 0.947 s

(Extrusion Shear is 9118 1/s Throughout)

Fig 4.3 Fibres produced at varying extrusion Shear

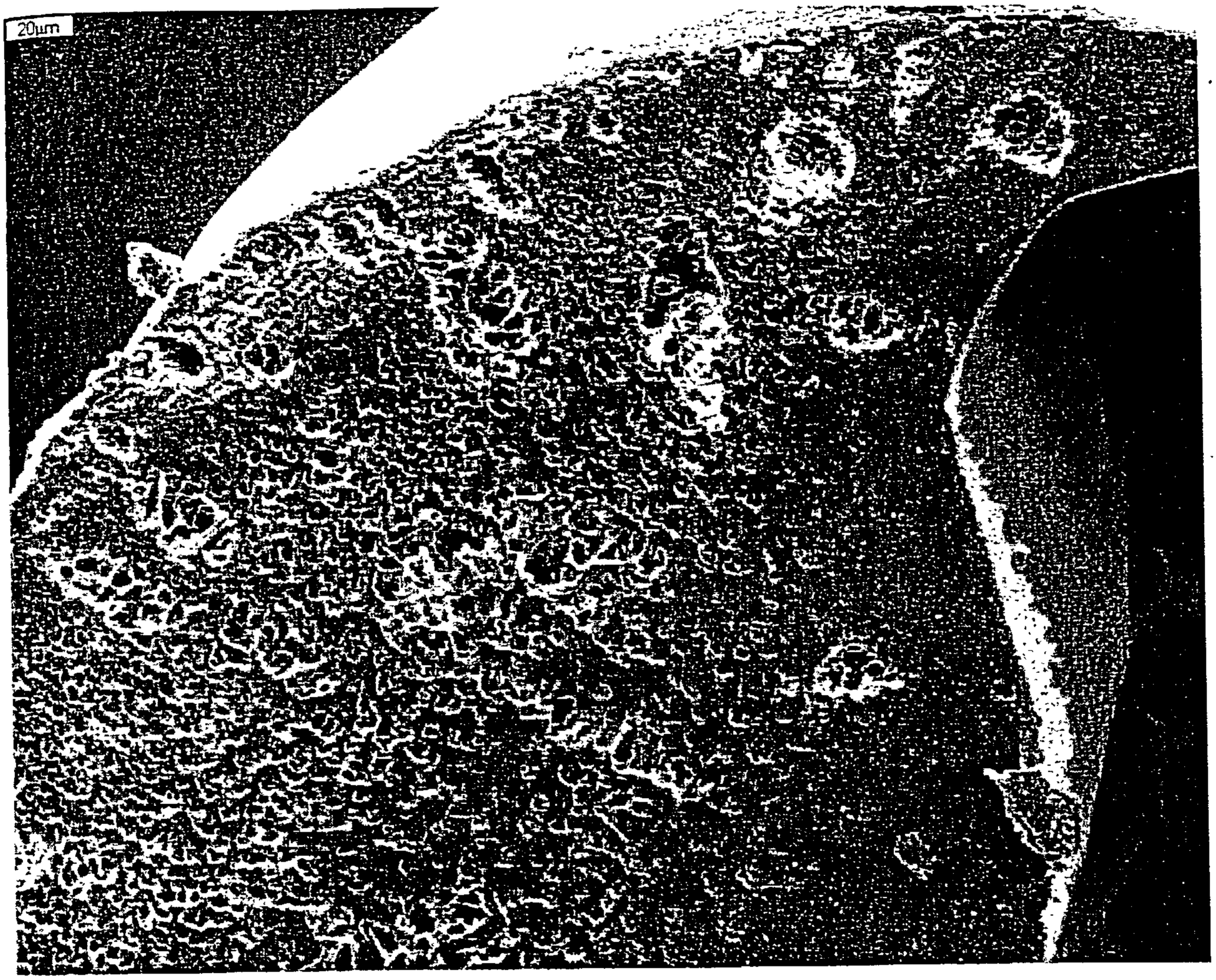

DER 0.833 cm^3/min
Extrusion Shear 3038 1/s

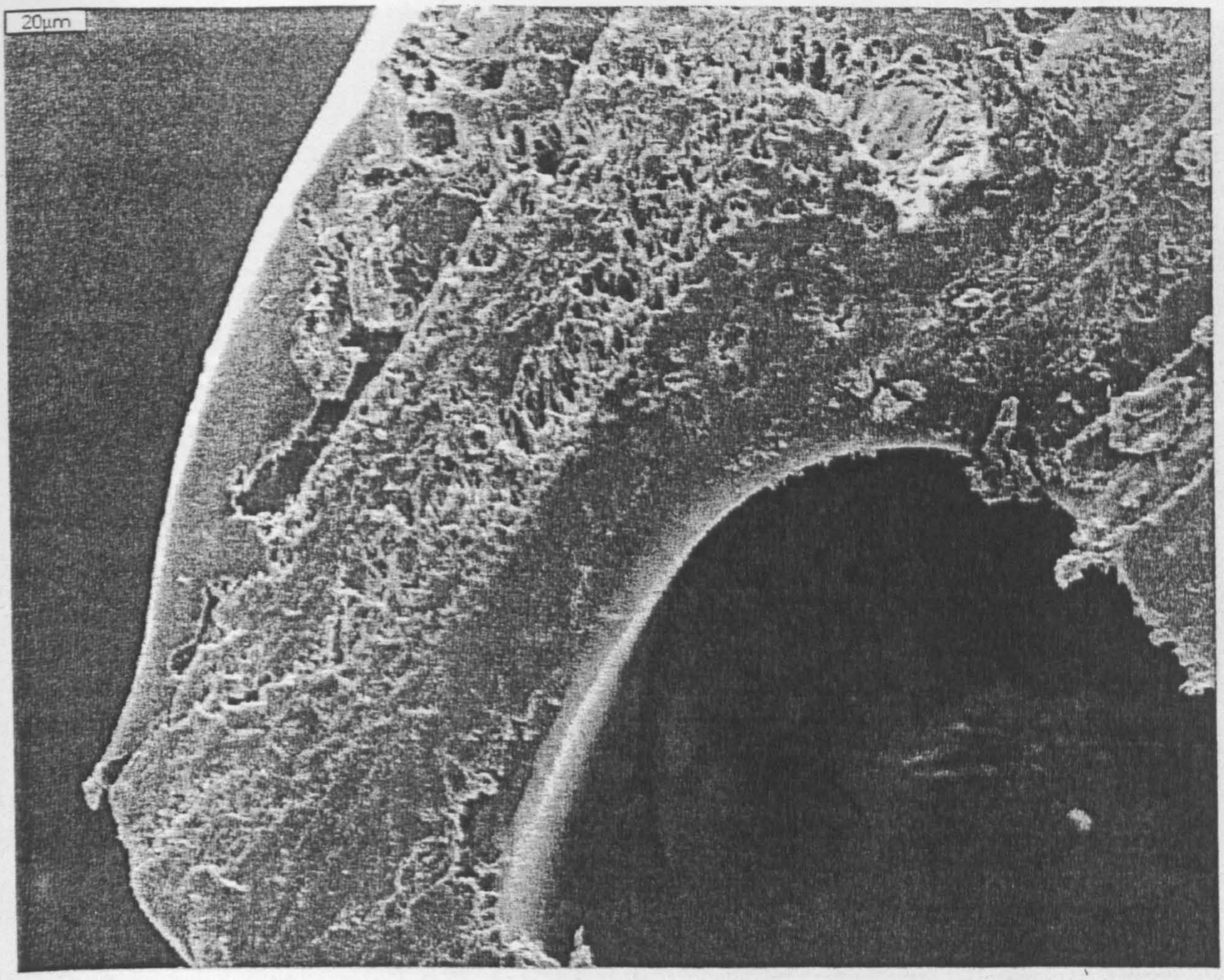

DER 1.5 cm^3/min
Extrusion Shear 5471 1/s

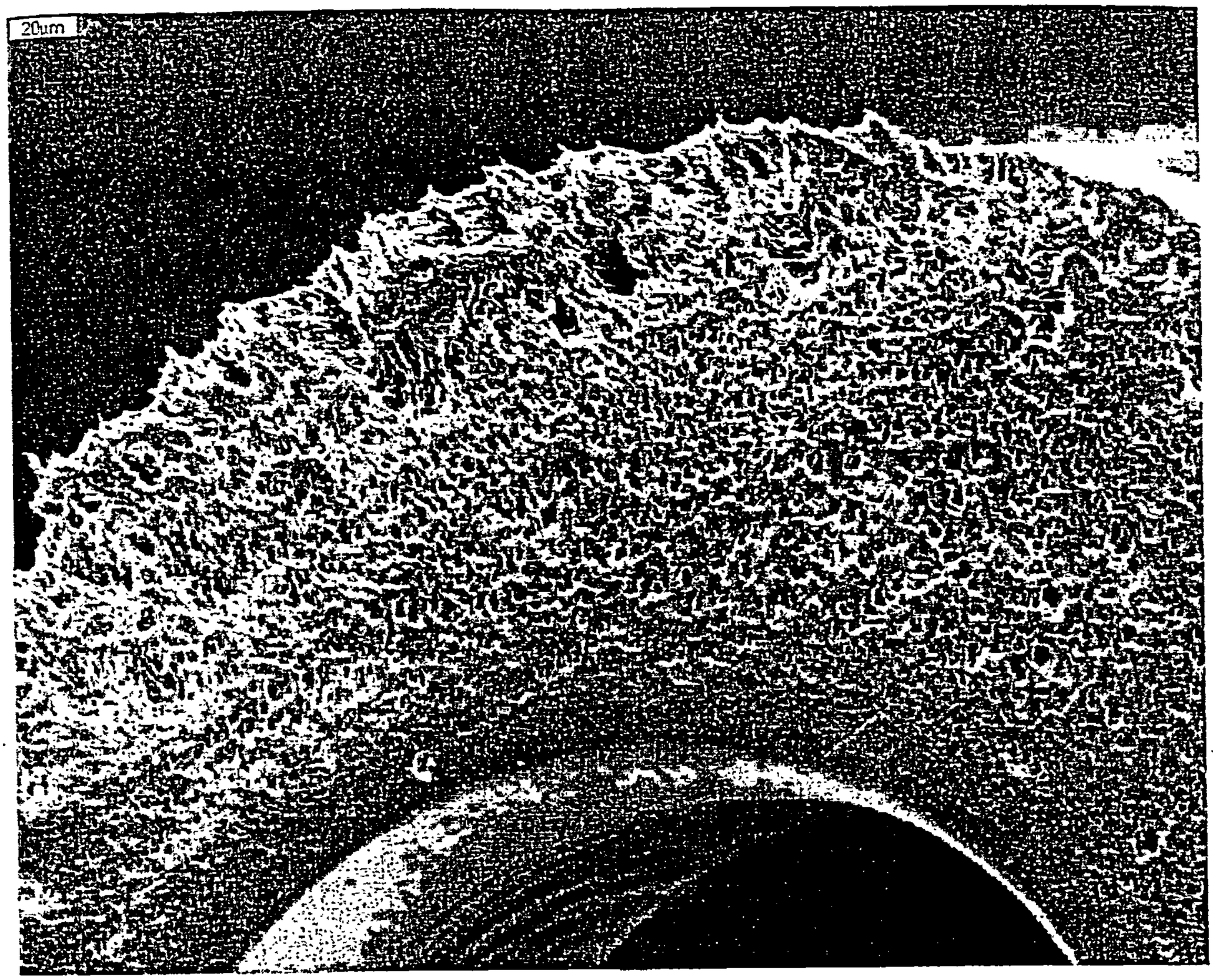

DER 3.33 cm^3/min
Extrusion Shear 12162 1/s

(Residence Time Fixed at 0.710 s)

4.4 Discussion of Results

4.4.1 Fibres Spun With Varying Residence Time

Uncoated Data

The uncoated results for varying residence time show an interesting trend. At the shortest residence time (0.237s) the skin is 15000 Å thick and the porosity is 2.34 x 10^{-7} m^2/m^2. The skin is considerably thicker than the skins formed in the fibres spun from the 22% polymer solution. The porosity is also lower than that seen in the equivalent 22% fibre. The porosity is the highest level of surface porosity in this campaign and this is the same trend as the 22% campaign. This suggests that the skin has not yet formed.

At the residence time (0.426s) the skin has become thicker and less porous. This could be due to the phase separation progressing further into the membrane and the nodules taking longer to coalesce. There is still no evidence of damage from the coagulation front moving in from the lumen.

At the third residence time (0.710s) the skin is at its thickest and the porosity has decreased further still. This suggests that the nodules at the surface are still forming and coalescing.

At the final air gap the porosity has decreased further but the skin has become thinner. This could be due to the back of the skin re-dissolving into the bulk of the fibre. This effect is the same that seen as the residence time is increased to its maximum in the 22% campaign.

The trend in porosity is interesting. It shows clearly that there is no effect from the internal coagulation front breaching the outer skin even at the longest dry-gap residence time. This effect was seen at the longest forced convection residence time during the 22% work. This is not surprising given the greater polymer content of the spinning dope. This would mean the diffusion of water through the dope would be much slower.

The fact that the skin is still coalescing at the longest air gap is interesting. This would suggest that the polymer nodules formed by the phase separation are much stiffer and resist deformation more and so take longer to coalesce. This is again to be expected given the polymer content of the dope. As the dope phase separates the polymer content of the polymer rich phase will be much higher than that of the 22% polymer dope.

The trend in skin thickness is not as clear as the trend in porosity. The results suggest that the skin takes some time to form and so for the first 3 air gaps the skin becomes thicker. At the final air gap the skin becomes thinner possibly due to the effect of the bulk fibre re-dissolving the back of the outer skin.

Coated Results

The coated results show similar trends to the uncoated results. However all the fibres exhibited poor gas separation performance and so an apparent skin thickness calculation could not be justified. The low selectivities obtained suggest that a substantial proportion of the gas flux is passing through pores.

At the shortest residence time (0.237s) the selectivities are 4.59 for O_2/N_2 and 13.39 for the CO_2/CH_4 separations. The low permeabilities and selectivities suggest that the membranes have thick porous skins. The O_2/N_2 selectivity is 75% of the intrinsic selectivity whereas for CO_2/CH_4 the selectivity is 48% of the intrinsic value. This is not surprising as CO_2 is by far the fastest gas. The relative resistance of the skin is therefore less for CO_2 than for CH_4 the slowest gas. Therefore any defect will effect the flux of CH_4 far more than CO_2. CH_4 is also a much lighter gas and so is much faster through pores than CO_2. O_2 and N_2 however are similar in size and speed of diffusion through pores and although O_2 travels faster through the polymer matrix the difference is not as marked as for CO_2/CH_4. This means that the effect of pores is more marked for CO_2/CH_4 than for O_2/N_2. This explains why the selectivities are not the same fraction of the intrinsic values.

At the next residence time the permeability falls for all the gases and the selectivity also falls. The falling permeability suggests that the skin has become thicker and the falling selectivity suggests the porosity has increased. The uncoated data shows that the skin does increase in thickness however the porosity decreases. The fall in selectivity is due to the increase in the relative resistance of the skin. Although the porosity has decreased the relative resistance of the skin has almost doubled, this means more of the slower gas is encouraged to flow through the pores.

As the residence time increases to 0.710s the permeability decreases further but the selectivity increases. This suggests that the skin has become thicker but less porous. This supports the uncoated data.

At the longest residence time the permeability increases and the selectivity increases. This suggests that the skin has become thinner and less porous. This supports the uncoated data.

Instron Results

The results from the mechanical testing show no trends again. However it should be noted that although the 1st modulus is corrected for linear density (N/tex) the fibres spun from the 40% dope are stronger than those spun from the 22% dope. This is a good result as it shows that the industrial membranes are stronger than the fibres produced from the standard dope. The maximum tenacity is also higher for the 40% fibres although it is also corrected for linear density.

SEM Images

The images produced do not show any obvious trends. The fibres are however still porous but do not contain any large macrovoids unlike the fibres produced from the 22% dope.

4.4.2 Fibres Spun With Varying Extrusion Shear

The effect of extrusion shear on the production of membranes from the 40% Psf dope is less clear than the effect of shear on the production of membranes from the 22% Psf dope.

Uncoated results

At the lowest rate of shear (3038 1/s) the skin formed is quite thin and the porosity is at its lowest. The skin is 9380 Å thick and the porosity is 2.385×10^{-8} m^2/m^2. As the shear increases to 5471 1/s the skin thins slightly to 9170 Å and the porosity increases slightly to 2.405×10^{-8} m^2/m^2.

As the shear is increased again to 9118 1/s there is a massive increase in the skin thickness to 24300 Å and the surface porosity also increases slightly to 3.52×10^{-8} m^2/m^2. As the shear is increased again to 12162 1/s the skin becomes much thinner again and the porosity falls slightly. The skin is 13250 Å thick and the porosity is 2.99×10^{-8} m^2/m^2.

Coated Results

The coated results show similar trends to the uncoated data. At the lowest rate of shear (3038 1/s) the fibres are the most selective and the apparent skin thickness is at its lowest. The apparent skin thickness is 9650 Å and the selectivities are 6.27 for O_2/N_2 and 23.15 for CO_2/CH_4. The high selectivities indicate that the membranes are not very porous and this agrees with the uncoated data.

As the rate of shear increases to 5471 1/s the apparent skin thickness increases slightly to 10228 Å and the selectivity falls to 5.57 for O_2/N_2 but rises slightly to 25.12 for CO_2/CH_4. This is quite unusual but the changes are minimal.

As the rate of shear increases again to 9118 1/s the permeability falls by 40% and the selectivity drops too low to justify an apparent skin thickness calculation. The selectivity falls to 3.61 for O_2/N_2 and 14.58 for CO_2/CH_4. The lowering permeability and the fall in selectivity suggest that the skin has become considerably thicker and more porous. This agrees with the uncoated data.

As the extrusion shear is increased to 12162 1/s the permeability increases and the selectivity increases as well. The selectivity increases to 4.78 for O_2/N_2 and 18.28 for CO_2/CH_4. The rise in permeability suggests the skin becomes thinner but the permeabilities are still lower than for the first two levels of shear. This means that although the skin becomes thinner it is still thicker than the first two categories spun at the lowest levels of shear. The rise in selectivity also suggests that the membranes become less porous but again are still more porous than the first two categories. This is also in good agreement with the uncoated data.

Instron Results

The results from the mechanical testing do not show any trends significant trends as the level of extrusion shear is increased. Although the active layer is affected by the level of extrusion shear this represents a tiny fraction of the fibre and so does not

contribute to the fibre bulk properties. The fibres are again more rigid than the fibres spun from the 22% dope.

SEM Images

Again the images show no clear trend but have no large voids compared to the equivalent 22% fibres.

4.5 Gas Mixture Work

To complement the pure gas permeation testing a campaign of gas mixture testing was carried out. This studied the most selective fibres produced using the 40% Psf dope. This category of fibre was that extruded at 0.833 cm^3/min with a 5cm air gap. The membranes were potted and coated in modules of 3 fibres as described in chapter 2 and tested as described in chapter 2. The selectivity and permeability was calculated as described in chapter 3.

4.5.1 Results

The six modules were produced and coated as described in chapter 2. The selectivities and permeabilities were calculated as described in chapter 3. Table 4.13 shows the average results for the six modules tested.

Table 4.13 Gas Mixture Permeation Results

Campaign	% O_2 in Permeate	P O_2	P N_2	Ω (O_2/N_2)	% CO_2 in permeate	P CO_2	P CH_4	Ω (CO_2/CH_4)
1.4	81.67	1.035	0.178	6.29	94.33	4.72	0.183	26.22

P= Pressure normalised flux x 10^6 [cm^3(stp)/(s cm^2 cmHg)], measured at 25°C and at a pressure differential of 5 bar.

4.5.2 Discussion

The selectivities and permeabilities calculated for the gas mixture work are similar to the values calculated for the pure gases. The selectivity for the O_2/N_2 separation is slightly higher when using the gas mixture but the difference is minimal. The

selectivity for the CO_2/CH_4 separation is actually slightly higher when using the gas mixture. The difference in the permeabilities is also minimal.

Chapter 5:

Spinning Novel Reinforced Gas Separation Membranes

5.1 Introduction

The membranes spun from the 22% polymer dope exhibit excellent gas separation properties and are productive membranes, they are however very delicate. The membranes spun from the 40% polymer dope are more robust and not as selective and are considerably less productive. In order to produce membranes that are permeable, selective and robust a novel approach was tried.

The most common approach to reinforce a polymer material mechanically is to fill it with stiff elongated inclusions such as chopped glass or carbon fibres [108]. Assuming that the filler particles are distributed evenly in the matrix and have a good cohesion to the polymer, an increase both in tensile strength and stiffness can be achieved [109]. Efficiency of reinforcement depends primarily on filler concentration and orientation distribution of the inclusions.

An important condition of efficient reinforcement is that the maximum dimension of the inclusion has to be much smaller than the minimum dimension of the composite. For our hollow fibre membranes the wall thickness is the critical dimension. The wall thickness of the membranes is about 150 μm. Both glass and conventional carbon fibres are continuous and have diameters of several microns. Such fibres can be chopped to a minimum length of about 200 μm and are so unsuitable for this application.

Vapour grown carbon fibre is a new class of material. These are produced by a different method to conventional carbon fibres and have unique physical characteristics and there is a prospect of low cost fabrication [119]. VGCF is similar to fullerene tubes in the nano-scale domain of initial formation and in the highly graphitic structure of the initial fibril. Processing conditions and treatments affect their properties greatly.

Table 5.1 Physical properties of VGCF [120]

Fibre diameter/length	0.1/1000 μm to 10/10000 μmμm
Tensile strength	2.7 to 7.0 GPa
Tensile Modulus	400 to 600 Gpa
Strain at break	0.5 to 1.5%
Density	1.8 to 2.1 g/cm^3
Electrical resistivity	1x 10^5 to 2x 10^6 S/m
Thermal conductivity	20 to 1950 W/mK

Table 5.1 shows the range of physical properties achieved for VGCF. It has been shown that due to the sub micron diameters and moderate lengths these carbon fibres can easily be incorporated in polymer fibres [121]. Thus VGCF with sub micron diameter and length below 100 μm are considered as the most appropriate filler to mechanically reinforce the polysulphone hollow fibre membranes.

5.2 Experimental

The VGCF used were supplied by Applied Science Inc (USA). The average diameter was about 200 nm and the length was in the range 5 to 60 μm.

The VGCF was added to the standard 22% polymer dope used in the first stage of this work. The amount of VGCF added was 0.6, 1.4 and 2.8 vol % with respect to the amount of polysulphone. The VGCF was pre dispersed in THF (about 10% of the THF required for the dope) in order to distribute it evenly. The dispersion of VGCF was stirred mechanically at room temperature for 30 min and then placed in an ultrasonic bath for another 30 min to break up the loosely aggregated filaments. After that the dispersion was added to the dope and stirred vigorously for 30 min.

The dope was filtered through a 230 μm stainless steel wire mesh before spinning to remove any remaining aggregates.

The three composite dopes were then spun using an air gap of 9cm and a nitrogen flow rate of 4 l/min in the forced convection chamber. The bore fluid and coagulation tank conditions were identical to the earlier campaigns. The DER was kept constant at 2.5 cm^3/min throughout.

The fibres were then treated and dried in the same fashion as described before.

For permeation testing the fibres were potted as single fibre modules and silicone coated as described before. They were then tested on the gas permeation rig using the same gas pairs as before (O_2, N_2, CH_4 and CO_2).

The fibres were also tested for their mechanical properties. The tensile properties were measured on the Instron 1122 machine and the fibres were also examined for their dynamic modulus using a Rheovibron machine at 10Hz.

5.3 Results and Discussion

5.3.1 Gas Permeation

Table 5.2 Gas permeabilities and selectivities

VGCF content (vol.%)	P O_2	P N_2	Ω (O_2/N_2)	P CO_2	P CH_4	Ω (CO_2/ CH_4)
0	10.10	1.50	7.46	58.20	1.54	40.10
0.6	12.31	2.27	5.42	66.28	2.31	28.69
1.4	14.08	3.18	4.43	75.73	4.23	17.89
2.8	16.93	7.48	2.26	67.64	9.79	6.91

P= Pressure normalised flux x 10^6 [cm^3(stp)/(s cm^2 cmHg)], measured at 25°C and at a pressure differential of 5 bar.

The gas permeation results are shown in the table above. As can be seen as VGCF content increases the permeability increases, unfortunately the selectivity decreases as the permeability increases. The decrease in selectivity suggests an increase in the surface porosity as the VGCF content is increased.

5.3.2 Mechanical Testing

Table 5.3 Tensile properties (static)

VGCF content (vol%)	Tenacity (MPa)	1st Modulus (MPa)	Strain at Break %
0.0	22.6	815.3	47.7
0.6	22.2	876.9	42.7
1.4	22.7	944.2	36.1
2.8	23.1	1005.6	22.2

Table 5.3 shows the mechanical properties of the filled membranes. Tenacity was found to be almost insensitive to VGCF content while the 1st modulus and % strain at break show a typical trend for fibre reinforced thermoplastics: stiffness is increased and ductility is decreased as VGCF content is increased. The increase in tensile modulus indicates that the carbon fibres adhere well to the polysulphone. Elongation at break falls from 47.7% for the unfilled membranes to 22.2% for the fibre with the highest VGCF content. However even at the highest VGCF content sample failure occurs well above the yield point. This suggests that the VGCF are evenly spread in the polymer matrix and do not produce weak points in the material at low extensions. The insensitivity of tenacity to VGCF content suggests that the matrix morphology plays the key role in the failure mechanism (eg. microvoids).

Table 5.4 Tensile properties (dynamic)

VGCF Content (vol%)	Moduli (relative to unfilled membranes)
0	1
0.6	1.09
1.4	1.20
2.8	1.29

The dynamic modulus results give an idea of the membrane response at low deformations. This is more like the conditions experienced in real life rather than the tensile characteristics at break. The dynamic modulus values display the same trend as the static moduli obtained from the tensile tests. The reinforcement effect however is greater in the dynamic measurements. The membranes with the highest VGCF content display an increase of 29% in the dynamic modulus over the unfilled membranes the increase is only 23% for the static tensile tests.

5.3.3 SEM Results

The membranes were mounted and coated as described before. The samples were analysed and the images of interest are shown below.

Fig 5.1 Reinforced membranes

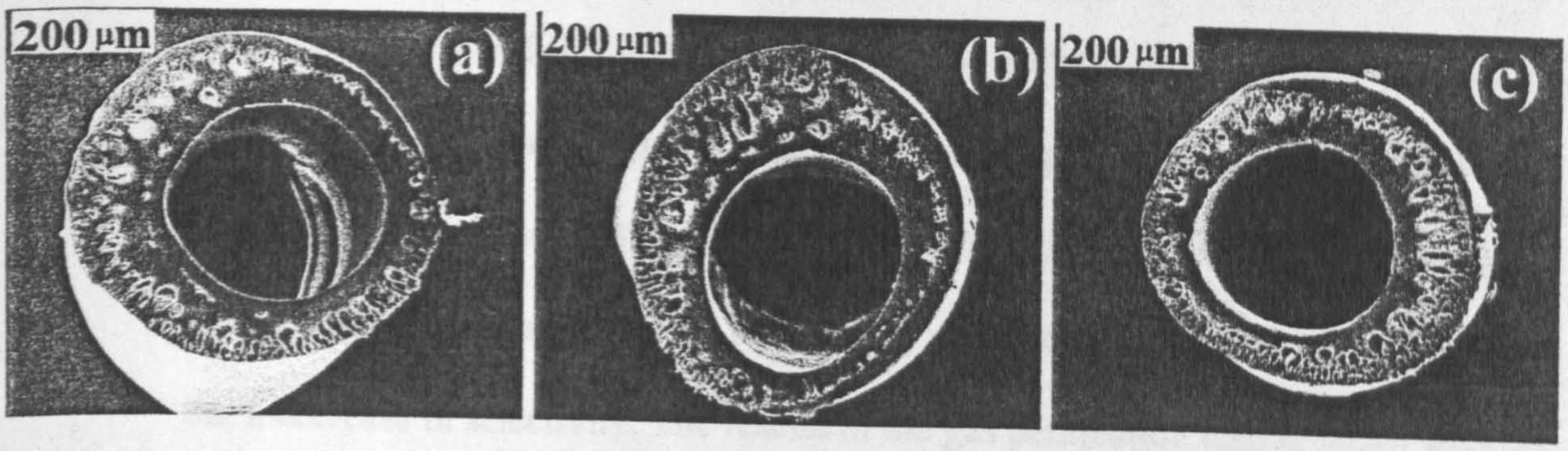

(a) 0 vol% VGCF

(b) 1.4 vol% VGCF

(c) 2.8 vol% VGCF

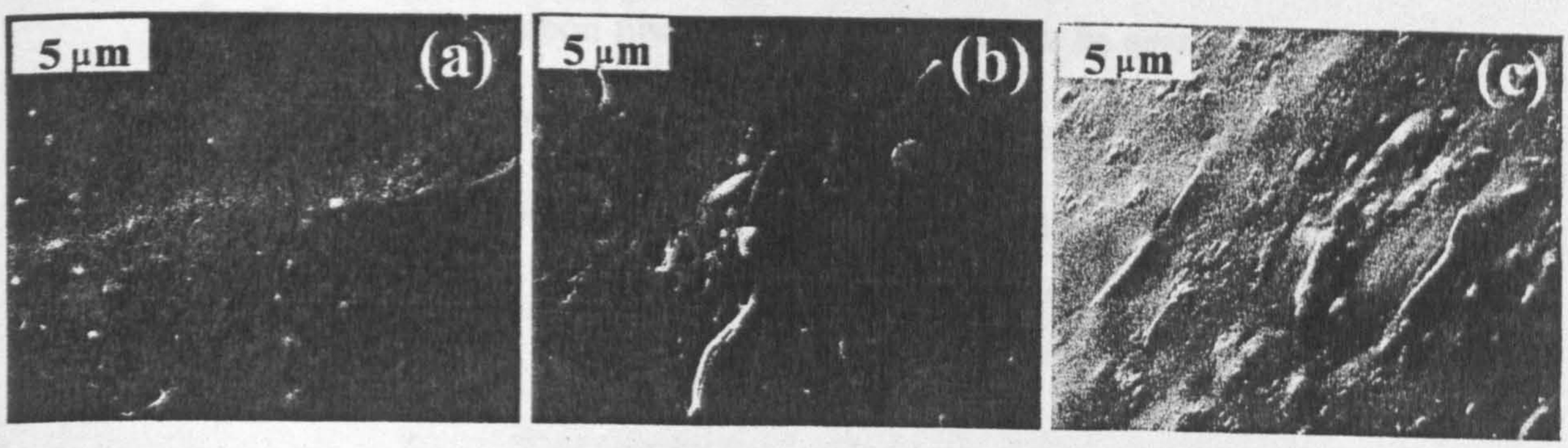

(a) 0 vol% VGCF

(b) 1.4 vol% VGCF

(c) 2.8 vol% VGCF

5.4 Discussion

The SEM photographs show the asymmetric structure of all the membranes. No substantial difference in morphology was detected between the un-filled and composite membranes.

The active layer is too thin to be studied using electron microscopy but some useful information can be derived from observations of the outside surface of the membranes. The unfilled membranes have few surface defects and these can be sealed with the silicone coating. However in the composite fibres some of the carbon fibres can be seen protruding through the surface of the membrane. These create extra damage to the active layer resulting in an increase in membrane permeability but a decrease in selectivity. The results of the gas permeation testing agree with this observation.

The images of the surface also provide more evidence of the strong interfaces between the filler material and the polysulphone matrix and also evidence of the even distribution of the carbon fibres in the matrix. As can be seen in fig no 5.1 there are no voids adjacent to the carbon fibres protruding from the membrane skin. The SEM photographs also provide evidence of the preferential orientation of the VGCF fibres in the extrusion direction.

The detrimental effects of the VGCF on the membrane selectivity experienced in this study could be overcome by altering the properties of the VGCF used. First of all the VGCF used in this study have a very broad length distribution. It can be seen in *fig*

5.1 that only the large VGCF disturb the membrane surface. Therefore using shorter VGCF with a narrow length distribution should be considered as a way to reduce surface damage. Secondly the requirements of the coating material may be different for the composite membranes compared to the unfilled membranes. The thickness of the silicone coating may be insufficient to completely cover the sections of carbon fibres proud of the surface. Coating with a more concentrated silicone solution could be a means to improve the membrane's selectivity. Finally the composition of the dope has changed compared to the standard dope. The amount of free solvent has been reduced due to absorption into the carbon fibres, this might affect the phase separation and so the active layer formation.

Chapter 6:

Discussion, Model Development, Conclusions and Recommendations for Future Work

6.1 Discussion

In the course of this work 3 main variables were studied: Air gap residence time, extrusion shear and polymer content/dope composition. A later phase of work also studied the effect of reinforcing the fibres with an advanced carbon fibre. These effects will all be considered now.

6.1.1 Residence Time

In order to consider the effect of residence time it is useful to consider what is happening in the air gap (fig 6.1). Firstly the fibre is extruded from the spinneret. As it is extruded the outside of the fibre begins to experience phase separation as the THF evaporates. At the same time the inside of the fibre phase separates and coagulates as it comes into contact with the bore fluid. As the fibre passes through the air gap the skin is formed and the coagulation front moves out from the bore. Then the fibre enters the coagulation tank where the fibre completes coagulating.

Fig 6.1 Dry/Wet Processes

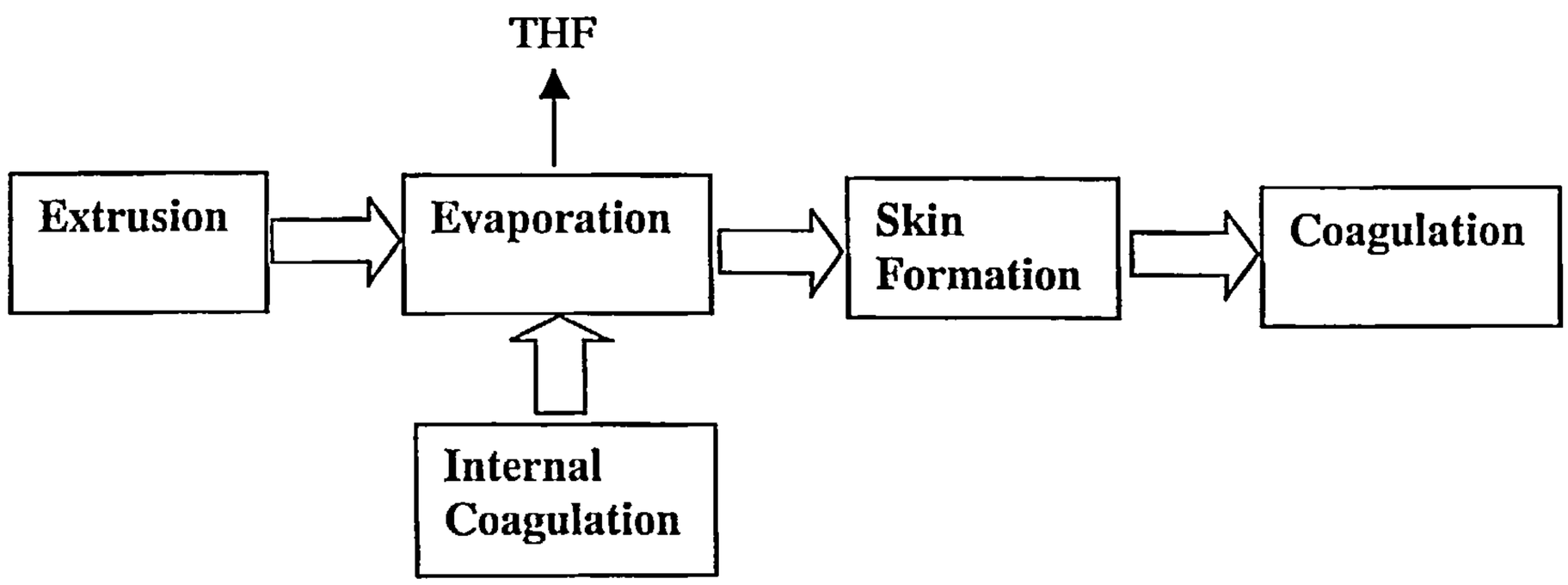

Each of these processes will now be examined in detail, firstly the evaporation.

6.1.1.1 Evaporation Model Development

There are two main areas in the forced convection chamber. First is the impingement zone, this is where the jet of nitrogen enters the chamber and comes into direct contact with the fibre. The nitrogen enters the chamber at half height. The nitrogen then flows through the tube and out the bottom and top of the tube. In order to study the mass transfer a simple model to describe the nitrogen flow in the forced convection chamber was developed in this study.

Fig 6.2 Forced Convection Model

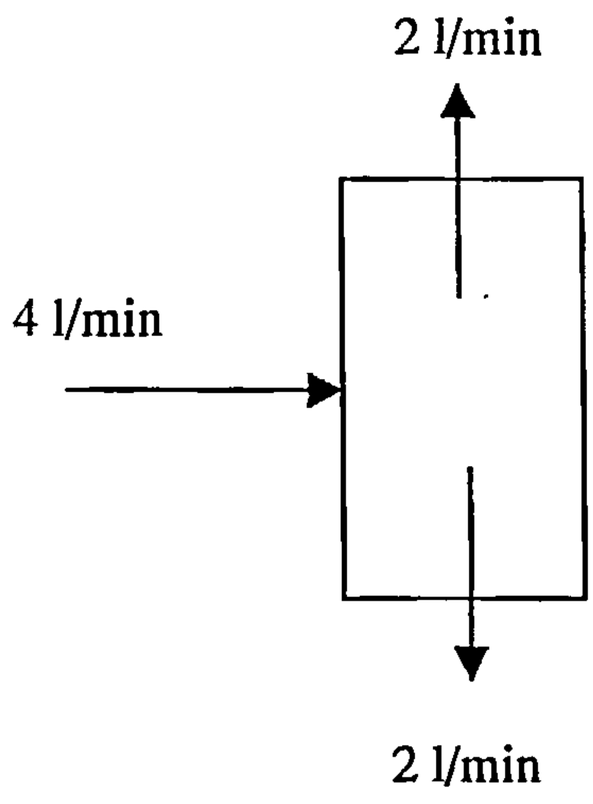

The model assumptions are that

1. The flow regime in the pipe is continued as a jet until the nitrogen strikes the fibre.
2. After the jet strikes the fibre the nitrogen divides equally and 2 litres flow up the chamber and 2 litres flow down the pipe.

Tsay and McHugh studied forced convection with respect to cast films and developed the following expression

$$\frac{kL_c y_{airlm}}{Dg} = 0.664\,\mathrm{Re}^{0.5}\,Sc^{0.33}$$

from an analogy with heat transfer [122].

Re = the Reynolds number

Sc = the Schmidt number ($\mu/\rho Dg$)

k = Mass transfer coefficient (cm/s)

L_c = Length of cast film

$y_{air\ lm}$ = Log mean mole fraction difference of the air

Dg = The mutual diffusion coefficient for the air-solvent system.

This expression was developed to describe evaporation from flat sheets from a heat transfer expression. An expression was found in Treybal [123] for heat transfer from a fluid flowing normally to a vertical tube. This was modified to a mass transfer expression and was used to model the impingement zone. The expression is

$$Sh = 0.43 + 0.532\,\mathrm{Re}^{0.5}\,Sc^{0.31}$$

Where

Sh = The Sherwood number

Re = Reynolds No.

Sc = Schmidt No.

Now the Sherwood no. $Sh = \frac{kd}{D}$

Where

k = Mass transfer coefficient

d = Characteristic dimension (same as in Re)

D = The diffusion coefficient

An expression was then found for the mass transfer in the pipe again from heat transfer. The expression was developed from an expression describing laminar forced convection and was found in Eckert and Drake [124].

$$Sh = 0.332\,\mathrm{Re}^{0.5}\,Sc^{0.33}$$

The value of the diffusion coefficient was calculated from an expression in Sinnot [125].

The formula for THF is C_4H_8O

The volume contributions are

C = 16.5 x 4

H = 1.98 x 8

O = 5.48 x 1

-20 contribution for the ring, so $\sum_a v_i = 67.32$

For N_2 $\sum_b v_i = 17.9$

$$D = \frac{1.013x10^{-7}\,x298^{1.75}\left(\frac{1}{28}+\frac{1}{72}\right)^{0.5}}{1.013\left[(17.9)^{\frac{1}{3}}+(67.32)^{\frac{1}{3}}\right]^{0.5}}$$

$$D_{THF/N_2} = 1.066x10^{-5}\,m^2/s$$

The Schmidt and Reynolds numbers were then worked out for the two different zones and both expressions were evaluated to give their respective Sherwood nos.

The Gas Velocities are calculated:

For the impingement zone

$Q=6.667 \times 10^{-5}\ m^3/s$

Flow Area = $1.256 \times 10^{-5}\ m^2$

Gas Velocity = 5.308 m/s

Taking values for viscosity and density from Steam Tables

Re = 212.2

For the chamber
$Q = 3.333 \times 10^{-5}\ m^3/s$

Flow Area = $1.963 \times 10^{-3}\ m^2$

Gas Velocity = 0.017 m/s

Re = 0.68

For both the chamber and impingement zone Sc is constant = 1.407

The two correlations are

$Sh = 0.43 + 0532\,\mathrm{Re}^{0.5}\,Sc^{0.31}$ for the impingement zone

$Sh = 0.332\,\mathrm{Re}^{0.5}\,Sc^{0.33}$ for the chamber

These are evaluated to give the two Sherwood nos.

These are 9.045 for the impingement and 0.306 for the tube.

The Sherwood nos. were then used to work out the respective k values. These k values were then used to work out an overall mass transfer coefficient, F from

F= kc

Where c is the molar volume of the gas.

The two values of F calculated are

$F = 6.573 \times 10^{-3}$ kmol/m^2.s for the impingement zone

$F = 2.22 \times 10^{-4}$ kmol/m^2.s for the chamber zone

As can be seen the more aggressive flow of nitrogen at the impingement zone results in a much higher mass transfer coefficient for the impingement zone.

Now multiplying the mass transfer coefficient by the respective areas and the driving force should give a rate of solvent loss from the impingement zone and the tube. The driving force is worked out by calculating the vapour pressure of the THF in the dope and calculating the mole fraction of the gas this represents.

Standard Spinning

The Antoine equation is used to calculate the vapour pressure of the THF at 25ºC [125]. The calculated vapour pressure is 161.08 mmHg.

This pressure is then multiplied by the mole fraction of THF in the dope to give a vapour pressure above the filament, this is 63.47 mmHg. This pressure is then divided by the total pressure, this gives an equilibrium mole fraction of 0.0835.

The mole fraction of THF in the bulk of the gas is considered to be 0. The driving force Δy is therefore 0.0835.

The rates of THF loss are calculated at

2.979×10^{-4} g/s in the impingement zone

2.516×10^{-3}h g/s in the chamber (where h is the height of the chamber)

Now calculating the amount of THF lost at each of the chamber heights and comparing this to the amount of THF entering the system a % loss of THF from the fibre can be calculated. This is shown in Table 6.1 underneath.

Table 6.1 THF loss (standard spinning)

Chamber Height (cm)	Residence Time (s)	Mass loss of THF, Impingement (g/s)	Mass loss of THF, Laminar (g/s)	% loss THF (total)
20	0.947	2.979×10^{-4}	5.04×10^{-4}	6.05
15	0.710	2.979×10^{-4}	3.78×10^{-4}	5.10
9	0.426	2.979×10^{-4}	2.27×10^{-4}	3.96
5	0.237	2.979×10^{-4}	1.26×10^{-4}	3.20

The table shows that although there is a difference in the amount of THF lost between the longest and shortest air gaps it is not as large as would be expected from the relative size difference. This is because the aggressive mass transfer in the impingement zone contributes a substantial proportion of the mass transfer and indeed dominates at the shorter chamber heights. This explains why that at these chamber heights the skin formation process appears to be independent of chamber height (c.f. page 97,99).

It is also possible that the very aggressive mass transfer in the impingement zone "seals" the skin of the membrane and thus stops mass transfer in the second half of the chamber and so makes the chamber height even less of a factor.

This process is then repeated for the 40% dope, which is spun at a higher temperature and has a different dope composition.

Industrial Spinning

The Antoine equation is used to calculate the vapour pressure of THF at 50°C [125]. The calculated vapour pressure is 437.11 mmHg. This is multiplied by the mole fraction to give a vapour pressure above the filament. This pressure is 85.24 mmHg. This gives a mole fraction of 0.112 of THF in the vapour above the filament. This gives a driving force Δy of 0.112.

The gas flow conditions are the same as for the standard spinning so the Re and Sc nos. are the same giving the same Sherwood nos. so the same mass transfer coefficients are calculated. Once the mass transfer coefficients are multiplied by the respective areas and the new driving force the rates of THF loss from the fibre for the industrial spinning can be calculated. These are given below in table 6.2.

Table 6.2 THF loss (industrial spinning)

Chamber Height (cm)	Residence Time (s)	Mass loss of THF, Impingement (g/s)	Mass loss of THF, Laminar (g/s)	% Loss THF (total)
20	0.947	3.568×10^{-3}	6.80×10^{-3}	100
15	0.710	3.568×10^{-3}	4.50×10^{-3}	100
9	0.426	3.568×10^{-3}	2.70×10^{-3}	100
5	0.237	3.568×10^{-3}	1.50×10^{-3}	100

Even at the shortest air gap all the THF is lost from the fibre, so effectively the rate of THF loss is independent of chamber height for the industrial spinning as well.

The table shows that even at the shortest air gap all the THF is lost from the fibre. This explains why the skins are much thicker than the skins formed during the standard spinning (c.f. page 121,122). Koros in his work with 40% Psf fibres reported a skin thickness of 1200 Å [68]. These fibres were produced using the same dope as the 40% fibres in this work. These skins are considerably thinner than those formed in our work. He does not describe the forced convection chamber in great detail in his work but it does not seem to include the aggressive impingement zone that our system contains. This supports the suggestion in this work that the impingement zone has a significant effect on the mass transfer, resulting in the thick skins seen in this work.

The model does not take into account the change in driving force; as the THF evaporates the driving force will decrease. For the standard spinning the overall loss of THF is not significant but for the industrial spinning the driving force will change considerably as the THF is lost.

The model does not take into account the speed of diffusion of the THF through the filament to the surface where it evaporates. The viscosity of the industrial dope is much higher so the THF will diffuse to the surface of the fibre much slower so the rate of THF loss will be slower than predicted but it will still be much higher than the loss during the standard spinning.

6.1.1.2 Skin Coalescence Model Development

The results from the uncoated resistance modelling from the 22% work also support the suggestion that although evaporation times vary they are not the dominant effect in skin formation. The results for the 22% work suggest that at the shortest residence time the skin does not have a chance to coalesce properly but at longer residence times the skin actually becomes thinner not thicker as would be expected.

This can be explained by developing a skin coalescence model. In Brown's work on skin formation in latexes he considered spherical nodules coalescing to form a uniform skin [70]. Here consider 3 spherical nodules surrounded by a bounding triangle.

Fig 6.3 Polymer nodule/skin coalescence

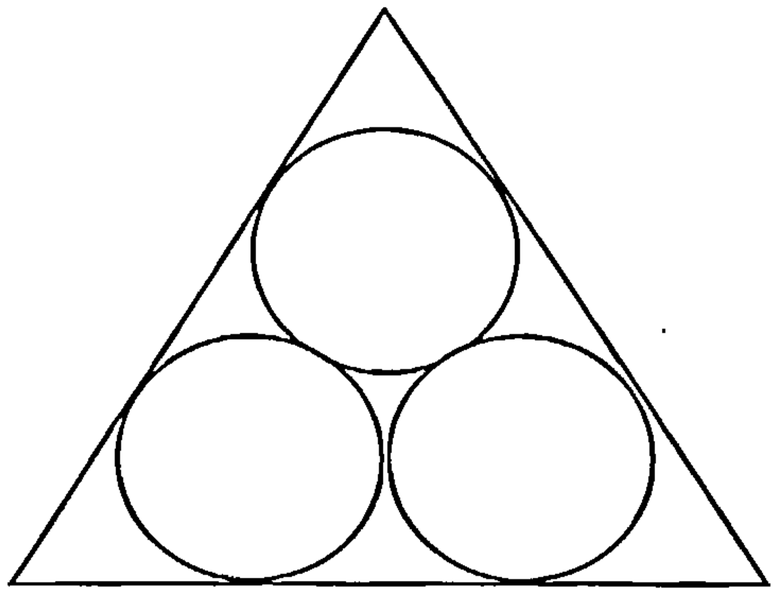

The 3 polymer rich nodules form a throat, which contains the polymer poor phase. The throat exerts a capillary pressure due to surface tension effects. It is the capillary pressure that drives the coalescence. The bounding triangle can be considered to be the same area of skin formed once the spheres have coalesced.

The volume of the 3 spheres is calculated and then divided by the area of the triangle to give an equivalent skin thickness once the spheres have coalesced.

For example an initial polymer nodule of diameter 1400 Å a skin of 680 Å is formed once the nodules have coalesced. This is in surprisingly good agreement with the experimental data. The data for the 22% fibres shows an initial skin thickness of 1450 Å this has reduced to 707.5 Å for the longest residence time. However other factors must be considered. It is unlikely that at the shortest air gap the skin consists entirely of perfectly spherical nodules and that by the longest air gap the skin has become a perfectly flat film. Coalescence must have started at the shortest air gap and the internal coagulation must also have a part to play. Koros suggests in his work that some of the skin re-dissolves into the bulk of the fibre [68]. This effect is likely to be more pronounced at longer air gaps, leading to thinner skins at longer air gaps. The fibres spun at the longest air gap also showed increased porosity, not what is expected as the skin has longer to coalesce. This increase in porosity is thought to be due to the internal coagulation front reaching the outer layers of the fibre and damaging the skin.

The model works well for the standard spinning but is harder to fit to the industrial spinning. The industrial dope has a much higher polymer content and so the viscosity is much higher. The data shows that the skin becomes thicker and then thinner as the air gap increases. The porosity decreases continuously as the air gap increases. These results suggest that skin formation is considerably slower than in the 22% fibres. This can explain the thickening and then thinning of the skin. The nodules take

longer to form and so as the air gap is increased the nodules are still forming at the 15cm air gap. The nodules are also much stiffer and so are still coalescing at the longest air gap. This also shows that the internal coagulation front does not reach the outside of the fibre as the porosity does not increase. Although the reduction in skin thickness as the air gap is increased from 15 to 20 cm seems large it is of the same magnitude as the decrease in the 22% fibres (between 5 and 9cm).

6.1.1.3 Internal Coagulation

The bore coagulant used throughout the spinning campaigns was a 20% w/w potassium acetate solution. This gives a water activity of 0.9 [68]. In previous work changing the water activity of the bore coagulant had a striking effect on fibres produced at the same extrusion conditions [80].

Lowering the water activity of the bore considerably improved the gas separation properties of the fibres, the permeability decreased but the selectivity more than doubled. This suggested that lowering the water activity of the bore reduced the surface porosity of the fibres. It is thought that if the internal coagulation front reaches the outside of the fibre before the fibre reaches the coagulation bath then this will result in damage to the skin. By lowering the water activity of the bore the internal coagulation is slowed and the skin is not damaged.

The effect if the internal coagulation front on skin integrity can be seen quite clearly for the 22% work. As the residence time passes a critical point the internal coagulation front reaches the outside of the fibre and the skin is damaged. This can

be seen as the air gap increases from 15 to 20cm. The permeability increases and the selectivity falls sharply as the surface defects undermine the separation performance.

The fact that this is not seen in the 40% work is to be expected. For the 22% fibres the internal coagulation front does not reach the outside of the fibre until the longest air gap. The 40% fibres will coagulate slower due to the higher polymer content leading to much slower diffusion across the phase interface. This would mean that an even longer air gap would be required before this phenomenon was seen in the 40% work.

6.1.2 Shear

The effect of shear on the membrane skin characteristics is quite striking. For the 22% fibres there is a clear trend, for the 40% fibres the trend is less clear.

For the 22% fibres as extrusion shear is increased the membrane skin becomes thinner. In his work on polymer solubility and shear effects Wolf introduced a stored energy term E_s to describe the extra energy effects of flowing systems. Wolf showed that shear could result in either flow induced homogenisation or phase separation depending on the ability of the components to store flow energy. Some systems showed both homogenisation and separation at different conditions.

In work on the 22% spinning dope no evidence of shear induced phase separation was seen [87]. It is possible that for the 22% system as shear increases the solution is able to store energy and so become more stable. This could result in less phase

separation for the same amount of solvent loss (all the fibres spun at different rates of shear experience the same evaporation conditions). This increase in stability would explain the thinner skins as shear increases.

The effect of shear on the 40% fibres is less clear. Initially as shear is increased there is no effect then suddenly the skin thickness increases greatly. It is possible that at this shear level the solution is able to store less flow energy as the shear pulls apart molecular entanglements (shear thinning). This loss of stored energy makes the solution less stable and so phase separates faster resulting in a thicker skin. As the shear is increased further the skin becomes thinner again. It is possible that as the shear increases further the solution is able to store energy again and so become more stable. These islands of instability have been observed before by Wolf [100,104,106].

The effect of shear on selectivity for the 22% work is quite clear. As the level of shear increases the selectivity increases due to molecular orientation in the active layer. Once a critical level of shear is passed the skin becomes to thin and any defects in the active layer degrade separation performance considerably.

6.1.3 Polymer Content

The effect of polymer content is quite clear. As the polymer content increases from 22 to 40% the fibres differ considerably. Unsurprisingly linear density and breaking load increase as the polymer content of the fibre increases. The tensile properties of the fibres are however standardised on the basis of polymer content (linear density). The tenacity and 1st modulus of the fibres both increase as the polymer content is

increased. The skin thickness also increases considerably as the polymer content increases. This suggests that as the polymer content is increased not only are the fibres more dense but the cohesive forces between the molecules become stronger.

Unfortunately increasing the polymer content greatly reduces the permeability of the fibres and so reduces their productivity. In some cases the skins became so thick that although the porosity was extremely low the fibres still exhibited low selectivities.

6.1.4 Fibre Reinforcement

The effect of reinforcing the membranes with carbon fibres is obvious. The mechanical properties are improved but this is accompanied with a loss of gas separation properties.

The loss of gas separation properties could be addressed by using a fibre with a more concentrated length distribution. From the microscopy it appeared that only the longer fibres protruded through the skin of the membrane. A fibre that had the mechanical properties of the reinforced membranes produced in this study along with the selective properties seen in the standard spinning campaign in this study would be very impressive.

6.2 Conclusions

The effects of extrusion shear and forced convection residence time both have an important impact on the performance of hollow fibre membranes. Polymer content also greatly effects the performance and properties of hollow fibre membranes. The effect of reinforcing fibres is mixed.

Extrusion shear not only effects the molecular orientation of the membranes but also the thickness of the active layer. The thickness of the active layer is an important factor in the performance of the membrane. If the active layer is too thick then any defects render the membrane useless. Increased molecular orientation is beneficial to the performance of a gas separation membrane. Increasing the molecular orientation can lead to above intrinsic selectivities. It is important to balance the relationship between molecular orientation and skin thickness in order to produce high performance membranes.

The effects of residence time on membrane performance are clearly shown in this work. If the residence time is too short then the skin does not have a chance to form and performance is degraded. If the residence time is too long then the internal coagulation front will reach the outer layer of the fibre and damage the active layer degrading the performance.

The aggressive forced convection technique pioneered in our group also effects the membrane performance. The mass transfer of volatile solvent is greatly influenced

by the aggressive impingement zone, which is a feature of our system. This leads to the formation of thick oriented skins.

Increasing the polymer content of the fibres greatly effected the performance and properties of the membranes. Unfortunately the aggressive forced convection process coupled with the increase in polymer content led to thick skins which although extremely sound were too unproductive to be used in an industrial environment. Increasing the polymer content did however improve the mechanical properties of the fibres.

6.3 Recommendations for Future Work

Theoretical studies should be carried to better understand some aspects of this work.

1. A study of the polymer solutions to develop a phase diagram and theoretical studies to see how this is affected by shear should be investigated to further understand the effect of extrusion shear on active layer thickness.
2. A detailed development of a model to describe the mass transfer in the forced convection chamber and also a model to describe the mass transfer in the bore. This coupled with a phase diagram would give a good insight into the membrane formation processes taking place in the forced convection chamber.
3. The design of higher polymer content dopes which would produce desired morphologies for gas separation membranes should also be undertaken

A number of practical studies could also be undertaken to further this work.

1. The development of a phase diagram from experimental work should be carried out. This would enable a direct comparison with any theoretical phase diagram developed to better understand the phase separation process and the polymer/solvent, polymer/non-solvent and solvent/non-solvent interactions.
2. An experimental study of the forced convection chamber using the GC to study the composition of the gas produced would lead to a better understanding of the mass transfer in the air gap and would also complement any model developed.
3. A further campaign of work with a high polymer content dope to fine tune the forced convection process and produce a fibre with a suitable morphology for industrial gas separation should be undertaken.

4. Further work on reinforcing membranes with novel carbon fibres should be undertaken with a more controlled length distribution of fibre to see if the fibres can be reinforced without losing their separation properties.
5. Further spectroscopic studies (IR, Raman and PALS) of the membrane active layer should be carried out to try and quantify orientation and also to further study the molecular conformation in the active layer should be carried out to better understand the phenomenon of super selectivity.

List of Publications Arising From this Work

Refereed Journal Papers

1. I. D. Sharpe, A. F. Ismail and S. J. Shilton, A study of extrusion shear and forced convection residence time in the spinning of polysulphone hollow fibre membranes for gas separation, Sep. and Purif. Tech. 17 (1999) 101-100
2. S. A. Gordeyev, I. D. Sharpe and S. J. Shilton, Processing and properties of polysulphone hollow fibre membranes for gas separation filled with sub-micron carbon fibres, Macromol. Symp. 170 (2001) 273-281

Conference Papers/Posters

1. I. D. Sharpe, A. F. Ismail and S. J. Shilton, Extrusion shear and the development of advanced industrial hollow fibre membranes for gas separation, PB-37 Euro-Membrane '99
2. A. F. Ismail, I. D. Sharpe, I. R. Dunkin and S. J. Shilton, Polysulphone membranes with enhanced selectivity: Gas mixture permeation tests, PB-38 Euro-Membrane '99
3. V. Bhardwaj, A Macintosh, I. D. Sharpe, S. A. Gordeyev and S. J. Shilton, Spinning and characterisation of carbon black filled asymmetric hollow fibre membranes for gas separation, United Engineering conference on "Advanced Membrane Technology" 2001

References

1. J.A. Nollet, Investigations on the causes for the ebullition of liquid (translated from the original manuscript by K. Boddeker), J. Mem. Science 100 (1995) 1-3.
2. J.K. Mitchell, On the penetrativeness of fluids, Royal Inst. J. 2 (1831) 101-118.
3. A. Fick, On liquid diffusion (translated from the original manuscript by K. Boddeker), J .Mem. Science 100 (1995) 33-38
4. T. Graham, On the absorption and dialytic separation of gases by colloid septa, Part 1- Action of a septum of caouchtouc, Philos. Mag. 32 (1866) 401-420.
5. S. Von Wroblewski, Weid. Ann. Physik, 8 (1899) 29
6. S. Loeb and S. Sourirajan, Sea water demineralisation by means of an osmotic membrane, Adv. Chem. Ser. 38 (1962) 117
7. J. M. S. Henis and M. K. Tripodi, Multicomponent membranes U.S. patent no 4230463 1980
8. J. M. S. Henis and M. K. Tripodi, Composite hollow fibre membranes for gas separation: The resistance model approach, J. Mem. Science 8 (1981) 233
9. S. J. Shilton, Ph.D. Thesis, University of Strathclyde 1992
10. W. J. Koros, Membranes: learning a lesson from nature, Chem. Eng. Prog. (Oct 1995) 68-81.
11. P.S. Puri, Gas separation membranes- current status, Japanese Mem. J. Vol. 6 No. 3 (1996) 117-126.
12. M.D. Rosenzweig, Unique membrane system spurs gas separation, Chem. Eng. 30 (1981) 62-66.
13. D. J. Stookey, J. E. Graham and W. M. Pope, Natural gas processing with Prism separators, Env. Prog. 3 (1984) 212-214

14. P. S. Puri, Membrane Gas Separations: An opportunity for industrial gas companies or just a niche market, Key note Lecture B-01, Euromembrane 99.

15. R. R. Zoland and G. K. Fleming, in W. S. Ho and K. K. Sirdar, Membrane handbook, Van Nostrand Reinhold, New York, 1992, Chap 2-6.

16. H. K. H. Minaki, S. Takaki, K. Tanaha and K. Okamoto, Pervaporation and vapour permeation of water/organic liquid mixtures through a T type zeolite membrane, Abstract lecture B-05 Euromembrane 1999.

17. H. Daynes, Proc. Roy. Soc. London, Ser. A, 97A (1920) 286.

18. R. Barrer, Trans. Faraday Soc. 35 (1939) 628

19. S. A. Stern, Polymers for gas separation: The next decade, J. Mem. Science 94 (1994) 1-65.

20. S. A. Stern and S. Trohalaki, Fundamentals of gas diffusion in rubbery and glassy polymers, in W. J. Koros (ed.) Barrier polymers and structures, A.C.S. Symp. Ser. 423 (1990) 22-59.

21. P. Meares, The diffusion of gases through polyvinyl acetate, J. Am. Chem. Soc. 76 (1954) 3415-3422.

22. W. W. Brandt Model calculations of the temperature dependence of small molecule diffusion in high polymers, J. Phys. Chem. (1959) 1080-1084

23. W. W. Brandt and B. A. Anyses, Diffusion of gases in fluoro-carbon polymers, J.A.P.S. 7 (1963) 1919-1931.

24. A. T. DiBenedetto and D. R. Paul, An interpretation of gaseous diffusion through polymers using fluctuation theory, J. Polym. Sc. Part A-2 (1964) 1001-1015.

25. M. H. Cohen and D. Turnbull, Molecular transport in Liquids and gases, J. Chem. Phys. 31 (1959) 1164-1169

26. S. A. Stern and H. L. Frisch, The selective permeation of gases through polymers, An. Rev. Mater. Sc. 22 (1981) 523-550

27. H. Fujita, Diffusion in polymer diluent systems, Fortschr.: Hoch polym. Forsch. 3 (1964) 1-47

28. M. S. Suwandi and S. A. Stern, Transport of heavy organic vapours through silicone rubber, J. Polym. Sc. Polym. Phys. Ed. 11 (1973) 663-681.

29. S. A. Stern, S. M. Fang and H. L. Frisch, Effect of pressure on gas permeability co-efficient. A new application of "free volume" theory, J. Polym. Sc. Part A-2 , 10 (1972) 201-209.

30. S. A. Stern, S. M. Fang and H. L. Frisch, A "free volume" model of permeation of gas and liquid mixtures through polymer membranes, Chem. Eng. Sc. 30 (1975) 773-780.

31. a. S.A. Stern, S. A. Kulharni and H. L. Frisch, Tests of a "free volume" model of gas permeation through polymer membranes. I. Pure CO_2, CH_4, C_2H_4 and C_2H_5 in polyethylene, J. Polym. Sc. Phys. Ed. 21 (1983) 467-481.

b. S.A. Stern, S. A. Kulharni and H. L. Frisch, Tests of a "free volume" model of gas permeation through polymer membranes. II. Pure Ar, SF_6, CF_4 and $C_2H_2F_2$ in polyethylene, J. Polym. Sc. Phys. Ed. 24 (1986) 2149-2166.

32. S. A. Stern, G. R. Mauze and H. L. Frisch, Tests of a "free volume" for the permeation of gas mixture through polymer membranes CO_2-C_2H_4, CO_2-C_3H_4, C_2H_4-C_3H_8 mixtures in polyethylene, J. Polym. Phys. Ed. 21 (1983) 1275-1298.

33. J. Crank, The mathematics of diffusion, 2nd Ed. Clarendon Oxford 1975.

34. R. T. Chern, W. J. Koros, B. Yui, H. B. Hopfenberg and V. T. Stannet, Selective permeation of CO_2 and CH_4 through kapton polyimide: Effects of penetrant competition and gas phase non-ideality, J. Polym. Sc. 22 (1984) 1061-1084

35. H. L. Frisch, Sorption and transport in glassy polymers, a review, Polym. Eng. Sc. 20 (1980) 2-13

36. D. R. Paul and W.J. Koros, Effect of partial immobilising sorption on permeability and the diffusion time lag, J. Polym. Sc. Polym. Phys. Ed. 14 (1976) 675-685.

37. D. R. Paul, Gas sorption and transport in glassy polymers, Ber. Bunsenges Phys. Chem. 83 (1979) 294-302

38. W. J. Koros, D. R. Paul and G. S. Huvard, Energetics of gas sorption in glassy polymers, J. Polym. Sc. Part A-2 8 (1979) 956-960.

39. W. R. Veith, J. M. Howell and J. H. Hsieh, J. Mem. Sc. 1 (1976) 177-220.

40. W.J. Koros, A. H. Chan and D. R. Paul, Sorption and transport of various gases in polycarbonate, J. Mem. Sc. 2 (1977) 165-190

41. a. R. J. Pace and A. J. Datyner, Statistical mechanical model for diffusion of simple penetrants in polymers I. Theory, J. Polym. Sc. Polym. Phys. Ed. 17 (1979) 437-451.

b. As above II, Applications: Non vinyl polymers, J. Polym. Sc. Polym. Phys. Ed. 17 (1979) 453-463

c. As above III, Applications: vinyl and related polymers, J. Polym. Sc. Polym. Phys. Ed. 17 (1979) 465-476

42. a. R. J. Pace and A. J. Datyner, Statistical mechanical model for diffusion of complex penetrants in polymers I: Theory, J. Polym. Sc. Polym. Phys. Ed. 17 (1979) 1675- 1692

b. As above II: Applications, J. Polym. Sc. Polym. Phys. Ed. 17 (1979) 1693- 1708

43. a. J. S. Vrentas and J. L. Duda, Diffusion in polymer-solvent systems I: Re examination of free volume theory, J. Polym. Sc. Polym. Phys. Ed. 15 (1977) 403-416

b. J. S. Vrentas, J. L. Duda, S. T. Ju and H. T. Liu, Prediction of diffusion co efficients for polymer-solvent system, A.I.Ch.E. J. 28 (1982) 279-285.

44. A. Fouda, Y. Chen, J. Bai and T. Matsuura, J. Mem. Sc. 64 (1991) 263

45. S. J. Shilton, G. Bell and J. Ferguson, The deduction of fine structural details of gas separation membranes using resistance modelling of gas permeation, Polymer 37 (1996) 485-492

46. R. E. Kesting, Synthetic polymeric membranes: A structural perspective, 2nd Ed. McGraw Hill, New York, 1985

47. P. van de Witte, P.J. Dijkstra, J. W. A. van den Berg and J. Feijen, Phase separation processes in polymer solutions in relation to membrane formation, J. Mem. Sc. 117 (1996) 1-31

48. M. Mulder, Basic principles of membrane technology, 2nd Ed. Kluwer academic publishers, 1996

49. P. J. Flory, Statistical mechanics of chain molecules, Interscience New York, 1969

50. W. J. Joros and G. K. Fleming, Membrane based gas separation, J. Mem. Sc. 83 (1993) 1-80

51. J. W. Cahn, Phase separation by spinodal decomposition in isotropic systems, J. Chem. Phys. 42 (1965) 93-99.

52. S. Nunes and T. Inoue, Evidence for spinodal decomposition and nucleation and growth mechanisms during membrane formation, J. Mem. Sc. 111 (1996) 93-103

53. J. G. Wijmans, J. Kant, M. H. V. Mulder and C. A. Smolders, Phase separation phenomena in solutions of polysulphone in mixtures of a solvent and non solvent: Relationship with membrane formation, Polymer 26 (1985) 1539.

54. S. J. Law and S. K. Mukhopadhyay, The construction of a phase diagram for a ternary system used for the wet spinning of acyrlic fibres based on a linearized cloud point curve correlation, J. of Appl. Poly. Sc. 65 (1997) 2131-2139.

55. J. Y. Kim, H. K. Lee, K. J. Baik and S. C. Kim, Liquid-liquid phase separation in polysulphone/solvent water systems, J. of Appl. Poly. Sc. 65 (1997) 2643-2653.

56. C. Barth and B. A. Wolf, Quick and reliable routes to phase diagrams for Polyethersulphone and polysulphone membrane formation, Macromol. Chem. Phys. 201 (2000) 365-374

57. S. A. McKelvey, D. T. Clausi and W. J. Koros, A guide to establishing hollow fibre macroscopic properties for membrane applications, J. Mem. Sc. 124 (1997) 223-232

58. A. J. McHugh and C. S. Tsay, Dynamics of the phase inversion process, J. of Appl. Poly. Sci. 46 (1992) 2011-2021.

59. C. S. Tsay and A. J. McHugh, Mass transfer dynamics of the evaporation step in membrane formation by phase inversion, J. Mem. Sc. 64 (1991) 81-92.

60. A. Ziabicki, Fundamentals of fibre formation, John Wiley, New York 1976.

61. P. S. Puri, Fabrication of hollow fibre gas separation membranes, Gas Sep. Purif. 4 (1990) 29-36.

62. J. A. van't Hoff, A. J. Reuvers, R. M. Boom, H. H. Rolevink and C. A. Smolders, Preparation of asymmetric gas separation membranes with a high selectivity by a dual-bath coagulation method. J. Mem. Sc. 70 (1992) 17-30.

63. I. M. Wienk, H. A. Teanis, Th. v. d. Boomgaard and C. A. Smolders, A new spinning technique for hollow fibre ultrafiltration membranes, J. Mem. Sc. 78 (1993) 93-100.

64. I. Pinnau and W. J. Koros, Defect free ultra high flux asymmetric membranes, U. S. patent 49024222 (1990).

65. I. Pinnau, J. Wind and K. V. Pieneman, Ultrathin multicomponent polyethersulphone membranes for gas separation made by dry/wet phase inversion, Ind. Eng. Chem. Res. 29 (1990) 2028-2032.

66. I. Pinnau and W. J. Koros, Influence of quench medium on the structures and gas permeation properties of polysulphone membranes made by wet and dry/wet phase inversion, J. Mem. Sc. 71 (1992) 81-96.

67. S. C. Pesek and W. J. Koros, Aqueous quenched asymmetric polysulphone membranes perpared by dry/wet phase separation, J. Mem. Sc. 81 (1993) 71-88.

68. S. C. Pesek and W. J. Koros, Aqueous quenched asymmetric hollow fibre membranes prepared by dry/wet phase separation, J. Mem. Sc. 88 (1994) 1-19.

69. I. Pinnau and W. J. Koros, A qualitative skin layer formation mechanism for membranes prepared by dry/wet phase inversion, J. Polym. Sc.: Part B Polym. Phys. 31 (1993) 419-427.

70. G. L. Brown, Formation of films from polymer dispersions, J. Polym. Sc. 22 (1956) 423-434

71. I. M. Wienk, Th. van den Boomgaard and C. A. Smolders, The formation of nodular structures in the top layer of ultrafiltration membranes, J. of Appl. Poly. Sc. 53 (1994) 1011-1023

72. M. Han and D. Bhattacharyaya, Changes in morphology and transport characteristics of polysulphone membranes made by different demixing conditions, J. Mem. Sc. 98 (1995) 191-200.

73. D. R. Paul, Spin orientation during acrylic fibre formation by wet-spinning, J of Appl. Poly. Sc. 13 (1969) 817-826

74. K. E. Perepelkin and B. M. Pugatch, Khimicheskiye Volokna 1 (1974) 48

75. M. R. Mackley, R. T. J. Marshall, J. B. A. F. Smeulders and F. D. Zhao, The rheological characterisation of polymeric and colloid fluids, Chem. Eng. Sc. 49 (1994) 2551-2565.

76. L. E. Nelson, Polymer rheology, Marckl Dekker, New York 1979

77. S. J. Shilton, G. Bell and J. Ferguson, The rheology of fibre spinning and the properties of hollow fibre membranes for gas separation, Polymer 35 (1994) 5327

78. S. J. Shilton, A. F. Ismail, P. J. Gough, I. R. Dunkin and S. L. Gallivan, Molecular orientation and the performance of synthetic polymeric membranes for gas separation, Polymer 38 (1997) 2215-2200.

79. A. F. Ismail, S. J. Shilton, I. R, Dunkin and S. L. Gallivan, Direct measurement of rheologically induced molecular orientation in gas separation hollow fibre membranes and the effect on selectivity, J. Mem. Sc. 126 (1997) 133-137.

80. A. F. Ismail and S. J. Shilton, Polysulphone gas separation membranes with enhanced selectivity, J. Mem. Sc. 139 (1998) 285-286.

81. P. Aptel, N. Abidine, F. Ivaldi and J. P. Lafaille, Polysulphone hollow fibres-Effect of spinning conditions on ultrafiltration properties, J. Mem. Sc. 22 (1985) 199-215.

82. O. M. Ekiner and G. Vassilatos, Polyaramide hollow fibres for hydrogen/methane separation- spinning and properties, J. Mem. Sc. 53 (1990) 259-273

83. T. S. Chung, J-J. Qin and J. Gu, Effect of shear rate within the spinneret on morphology separation performance and mechanical properties of ultrafiltration polyethersulphone hollow fibre membranes. Chem. Eng. Sc. 55 (2000) 1077-1091.

84. A. de Waele, Oil Colour Chem. Ass. J. 6 (1923) 23

85. W. Ostwald, Kolloid-Z 36 (1925) 99

86. R. I. Tanner, Engineering Rheology, Oxford science publications, Revised Ed. 1988.

87. S. A. Gordeyev, G. B. Lees, I. R. Dunkin and S. J. Shilton, Super-selective polysulphone hollow fibre membranes for gas separation: rheological assessment of the spinning solution, Polymer 42 (2001) 4347-4352.

88. A. F. Ismail, I. R. Dunkin, S. L. Gallivan and S. J. Shilton, Production of super selective polysulphone hollow fibre membranes for gas separation, Polymer 40 (1999) 6499-6506.

89. S. J. Shilton, Flow profile induced in spinneret during hollow fibre membrane spinning, J. of Appl. Poly. Sc. 65 (1997) 1359-1362.

90. I. D. Sharpe, A. F. Ismail and S. J. Shilton, A study of extrusion shear and forced convection residence time in the spinning of polysulphone hollow fibre membranes for gas separation, Sep. and Purif. Tech. 17 (1999) 101-109.

91. A. T. Serkov and O. A. Khanchich, Formation of oriented structures in the precipitation of polymers from concentrated solutions. Khimicheskie Volokna 4 (1977) 12-16.

92. Y. Takeuchi, Y. Shuto and F. Yamamoto, Band pattern development in shear oriented thermotropic copolyester extrudate, Polymer 29 (1988) 605-612.

93. M. Bousmina and R. Muller, Rheology/Morphology/flow conditions relationships for polymethylmethacrylate/rubber blend, Rheol. Acta 35 (1996) 369-381.

94. K. E. Perepelkin, The structural factor in the orientation process of fibres and films of flexible and rigid chain polymers, Khimicheskie volokna 4 (1977) 7-12.

95. J. Ferguson, C. Dougleris and G. R. McKay, Rheological and coagulation features in wet spinning process, J of Non-Newtonian Fluid Mech. 6 (1980) 333-338.

96. G. R. McKay, J. Ferguson and N. E. Hudson, Elongational flow and wet spinning process, J. Non-Newtonian fluid Mech. 4 (1974) 89-98.

97. M. R. Mackley, Hydrodynamics of polymer fluids, J. Poly. Sc. Poly. Symp. 73 (1985) 75-81.

98. H. W. Kammer, J. Kressler and C. K. Kummerbewe, Phase behaviour of polymer blends-Effects of thermodynamics and rheology, Adv. In Poly. Sc. 106 (1993) 31-85

99. D. Jou, J. Casas-Vazquez and M. Criado-Sancho, Thermodynamics of polymer solutions under flow: phase separation and polymer degradation, Adv. In Poly. Sc. 120 (1995) 207-266.

100. B. A. Wolf, Makromol. Chem. Rapid communication, 1 (1980) 231

101. B. A. Wolf, Thermodynamic theory of flowing polymer solutions and its application to phase separation, Macromolecules 17 (1984) 615-618.

102. H. Kramer-Lucas, H. Shenck and B. A. Wolf, Makromol. Chem. 189 (1988)

103. R. Horst, Calculation of phase diagrams not requiring the derivatives of the Gibbs Energy demonstrated for a mixture of two homo-polymers with the corresponding copolymer, Macromol. Th. Simul. 4 (1995) 449

104. R. Horst and B. A. Wolf, phase diagrams calculated for quaternary polymer blends, J. Chem. Phys. 103 (1995) 3782-3787.

105. R. Horst and B. A. Wolf, Phase diagrams calculated for sheared ternary polymer blends, Polymer 38 (1997) 4697-4703.

106. W. W. Graessley, Adv. In Poly. Sc. 16 (1974) 1.

107. B. A. Wolf, Improvement of polymer solubility: Influence of shear and pressure, Pure & Appl. Chem. 69 (1997) 929-933.

108. D. D. L. Chung, Carbon fibre composites, Boston MA: Butterworth-Heineman, 1994.

109. L. T. Drzal, M. Madhukar, Fibre-matrix adhesion and its relationship to composite mechanical properties, J. Mater. Sc. 28 (1993) 569-610.

110. S. A. Gordeyev, I. D. Sharpe and S. J. Shilton, Processing and properties of polysulphone membranes for gas separation filled with sub micron carbon fibres,

111. P. Manos, U.S. Patent 4120098 (1978)

112. R. R. Ward, R. C. Chang, J. C. Danos, J. A. Carde, U.S. Patent 4214020 (1980)

113. O. M. Ekiner and G. Vassilatos, Polyaramide hollow fibres for H_2/CH_4 separation II: Spinning and properties, J. Mem. Sc. 186 (2001) 71-84.

114. T. S. Chung and X. Hu, Effect of air gap distance on the morphology and thermal properties of Polyethersulphone hollow fibres, J. Appl. Poly. Sc. 66 (1997) 1067-1077.

115. T. S. Chung Z. L. Xu and W. Lin, Fundamental understanding of the effect of air gap distance on the fabrication of hollow fibre membranes, J. of Appl. Poly. Sc. 72 (1999) 379-395.

116. T. S. Chung, S. K. Teoh, W. W. Y. Lau an M. P. Srinivasan, Effect of shear stress within the spinneret on hollow fibre membrane morphology and separation performance, Ind. Eng. Chem. Res. (1998) 3930-3938

117. D. Wang, K. Li and W. K. Teo, Preparation and characterisation of polyetherimide asymmetric hollow fibre membranes for gas separation, J. Mem. Sc. 138 (1998) 193-201.

118. A. F. Ismail, Ph.D. Thesis, University of Strathclyde 1997.

119. M. L. Lake, in proceedings of NATO ASI workshop "Carbon filaments and nanotubes" Budapest, June 19-30, 2000, Chapter X.

120. Pyrograph III, Technical bulletin, Applied Sc. Inc. Cedarville Ohio (1998)

121. C. A. Bernardo, S. A. Gordayev and J. A. Fereira, in proceedings of NATO ASI workshop "carbon filaments and nanotubes" Budapest, June 19-30 2000, Chapter XIV.

122. C. S. Tsay and A. J. McHugh, A rational for structure formation during phase inversion, J. of Poly. Sc. Part B: Poly. Phys. 30 (1992) 309-313.

123. R. E. Treybal, Mass transfer operations, McGraw-Hill, International Ed 1981.

124. E. R. G. Eckert and R. M. Drake, Heat and Mass Transfer, McGraw-Hill 2nd Edn. 1959.

125. R. K. Sinnot, Chemical Engineering Vol. 6, Butterworth-Heinemann 3rd Edn. 1999

Appendices

Appendix 1: 22% Polymer Fibre: Gas permeation Data

Uncoated Experimental Data

Campaign 1: Varying Residence Time, Constant extrusion shear

Run	Air Gap Residence time (s)	Extrusion Shear (1/s)	P O_2	P N_2	P CH_4	P CO_2	Ω (O_2/N_2)	Ω (CO_2/CH_4)
1.1	0.237	8838	137.9336	142.2389	204.9913	181.1697	0.969732	0.883792
1.1	0.237	8838	124.0191	126.0775	178.9966	138.5846	0.983673	0.77423
1.1	0.237	8838	115.0003	118.2627	168.9223	124.1758	0.972414	0.735106
1.1	0.237	8838	68.46058	66.70017	96.38753	100.6253	1.026393	1.043966
1.1	0.237	8838	91.16978	90.31905	128.9126	123.171	1.009419	0.955461
1.1	0.237	8838	123.1061	126.4982	184.2474	152.3927	0.973184	0.827109

Run	Air Gap Residence time (s)	Extrusion Shear (1/s)	P O_2	P N_2	P CH_4	P CO_2	Ω (O_2/N_2)	Ω (CO_2/CH_4)
1.2	0.426	8838	11.85562	5.201352	6.851081	50.87935	2.279334	7.426471
1.2	0.426	8838	15.31337	6.847629	8.469718	59.3624	2.236302	7.008782
1.2	0.426	8838	12.7625	5.682116	7.249528	50.39694	2.246082	6.951754
1.2	0.426	8838	20.66476	15.11506	19.92034	61.29335	1.367164	3.076923
1.2	0.426	8838	13.66651	6.397434	7.437218	53.22415	2.13625	7.156459
1.2	0.426	8838	16.50139	7.815839	8.729936	63.80917	2.111276	7.309237

P= Pressure normalised flux x 10^6 [cm^3(stp)/(s cm^2 cmHg)], measured at 25°C and at a pressure differential of 5 bar.

Run	Air Gap Residence time (s)	Extrusion Shear (1/s)	P O_2	P N_2	P CH_4	P CO_2	Ω (O_2/N_2)	Ω (CO_2/CH_4)
1.3	0.710	8838	21.41414	13.72759	18.2714	58.84359	1.559934	3.22053
1.3	0.710	8838	45.58568	42.51444	58.33377	89.34469	1.07224	1.531612
1.3	0.710	8838	60.02003	57.9353	78.94238	100.8922	1.035984	1.278049
1.3	0.710	8838	40.60416	32.99009	44.23984	86.17215	1.230799	1.94784
1.3	0.710	8838	23.94	16.46515	21.65103	66.05272	1.45398	3.050789
1.3	0.710	8838	37.12847	29.56034	41.05894	83.39172	1.256023	2.031025

Run	Air Gap Residence time (s)	Extrusion Shear (1/s)	P O_2	P N_2	P CH_4	P CO_2	Ω (O_2/N_2)	Ω (CO_2/CH_4)
1.4	0.947	8838	35.37088	28.93211	38.94931	87.53011	1.222548	2.247283
1.4	0.947	8838	29.87022	22.73088	29.74624	81.57243	1.314082	2.742276
1.4	0.947	8838	32.22534	23.8218	31.11837	75.25857	1.352767	2.418462
1.4	0.947	8838	39.74103	31.28999	41.4732	86.87734	1.270088	2.094783
1.4	0.947	8838	39.72656	29.5915	39.66241	86.94141	1.342499	2.192035
1.4	0.947	8838	34.06694	23.35209	30.72171	89.54318	1.458839	2.914655

P= Pressure normalised flux x 10^6 [cm^3(stp)/(s cm^2 cmHg)], measured at 25°C and at a pressure differential of 5 bar.

Campaign 2: Varying Extrusion Shear, Constant Residence Time

Run	Air Gap Residence time (s)	Extrusion Shear (1/s)	P O_2	P N_2	P CH_4	P CO_2	Ω (O_2/N_2)	Ω (CO_2/CH_4)
2.1	0.710	2945	7.779709	6.533497	9.448562	18.79521	1.190742	1.989213
2.1	0.710	2945	3.366243	1.173056	1.485496	13.58234	2.869636	9.143302
2.1	0.710	2945	3.333193	0.885304	1.160503	13.39041	3.765029	11.53846
2.1	0.710	2945	4.109118	2.010082	2.843499	13.83055	2.044254	4.863921
2.1	0.710	2945	6.538706	4.088037	5.940802	13.69946	1.599473	2.305995
2.1	0.710	2945	4.356588	1.231773	1.751787	17.99171	3.536842	10.27049

Run	Air Gap Residence time (s)	Extrusion Shear (1/s)	P O_2	P N_2	P CH_4	P CO_2	Ω (O_2/N_2)	Ω (CO_2/CH_4)
2.2	0.710	5303	9.350837	4.995786	6.850063	30.72759	1.871745	4.485739
2.2	0.710	5303	18.15883	16.62343	24.00532	40.03618	1.092363	1.667804
2.2	0.710	5303	12.42293	10.1952	14.24713	25.99996	1.218508	1.824926
2.2	0.710	5303	13.54417	11.85808	16.74604	24.48977	1.142189	1.462422
2.2	0.710	5303	24.25209	22.95483	31.5048	32.22675	1.056514	1.022916
2.2	0.710	5303	13.33868	10.7976	15.07423	32.12541	1.235337	2.131148

P= Pressure normalised flux x 10^6 [cm^3(stp)/(s cm^2 cmHg)], measured at 25°C and at a pressure differential of 5 bar.

Run	Air Gap Residence time (s)	Extrusion Shear (1/s)	P O_2	P N_2	P CH_4	P CO_2	Ω (O_2/N_2)	Ω (CO_2/CH_4)
1.3	0.710	8838	21.41414	13.72759	18.2714	58.84359	1.559934	3.22053
1.3	0.710	8838	45.58568	42.51444	58.33377	89.34469	1.07224	1.531612
1.3	0.710	8838	60.02003	57.9353	78.94238	100.8922	1.035984	1.278049
1.3	0.710	8838	40.60416	32.99009	44.23984	86.17215	1.230799	1.94784
1.3	0.710	8838	23.94	16.46515	21.65103	66.05272	1.45398	3.050789
1.3	0.710	8838	37.12847	29.56034	41.05894	83.39172	1.256023	2.031025

Run	Air Gap Residence time (s)	Extrusion Shear (1/s)	P O_2	P N_2	P CH_4	P CO_2	Ω (O_2/N_2)	Ω (CO_2/CH_4)
2.4	0.710	11772	21.414144	13.72759	18.2714	58.84359	1.559934	3.22053
2.4	0.710	11772	45.58568	42.51444	58.33377	89.34469	1.07224	1.531612
2.4	0.710	11772	60.02003	57.9353	78.94238	100.8922	1.035984	1.278049
2.4	0.710	11772	40.604166	32.99009	44.23984	86.17215	1.230799	1.94784
2.4	0.710	11772	23.94	16.46515	21.65103	66.05272	1.45398	3.050789
2.4	0.710	11772	37.12847	29.56034	41.05894	83.39172	1.256023	2.031025

P= Pressure normalised flux x 10^6 [cm^3(stp)/(s cm^2 cmHg)], measured at 25°C and at a pressure differential of 5 bar.

Coated Experimental Data

Campaign 1: Varying Residence Time, Constant Extrusion Shear

Run	Air Gap Residence time (s)	Extrusion Shear (1/s)	P O_2	P N_2	P CH_4	P CO_2	Ω (O_2/N_2)	Ω (CO_2/CH_4)	λ (Å)
1.1	0.237	8838	13.35426	1.957144	2.022398	84.52917	6.823342	41.79651	747.7442
1.1	0.237	8838	8.915775	1.069256	1.765894	82.46877	8.338302	46.70087	1059.966
1.1	0.237	8838	11.00894	1.649534	2.172486	83.42713	6.673969	38.40169	818.8466
1.1	0.237	8838	9.719837	2.36301	2.933623	87.60057	4.113328	29.86088	718.3256
1.1	0.237	8838	12.49069	2.849255	3.655341	75.84921	4.383844	20.75024	619.9467
1.1	0.237	8838	7.953711	0.997297	1.846859	79.15971	7.975268	42.8618	1120.538

Run	Air Gap Residence time (s)	Extrusion Shear (1/s)	P O_2	P N_2	P CH_4	P CO_2	Ω (O_2/N_2)	Ω (CO_2/CH_4)	λ (Å)
1.2	0.426	8838	9.253732	1.148804	1.096891	55.85525	8.055102	50.92141	1224.578
1.2	0.426	8838	10.35333	1.37423	1.512813	66.77214	7.533917	44.13774	999.9311
1.2	0.426	8838	11.64256	2.008615	2.202671	69.38897	5.796311	31.5022	784.1737
1.2	0.426	8838	8.283858	1.027592	0.980668	47.26497	8.061427	48.19672	1381.826
1.2	0.426	8838	10.28681	0.931224	1.508112	63.49985	11.04655	42.10554	1159.083
1.2	0.426	8838	10.52455	2.48845	1.935115	46.53378	4.229362	24.04704	872.0518

P= Pressure normalised flux x 10^6 [cm^3(stp)/(s cm^2 cmHg)], measured at 25°C and at a pressure differential of 5 bar.

Run	Air Gap Residence time (s)	Extrusion Shear (1/s)	P O_2	P N_2	P CH_4	P CO_2	Ω (O_2/N_2)	Ω (CO_2/CH_4)	λ (Å)
1.3	0.710	8838	13.02414	1.830415	2.130244	85.18217	7.115404	39.98704	756.8638
1.3	0.710	8838	11.54858	1.514522	2.804508	91.81377	7.62523	32.73792	776.8907
1.3	0.710	8838	9.465252	1.713028	2.051996	82.44234	5.52545	40.17667	860.9207
1.3	0.710	8838	9.82236	1.405507	2.261793	91.90897	6.988483	40.63545	873.208
1.3	0.710	8838	14.49077	1.839372	1.883996	83.00305	7.878105	44.05692	763.1432
1.3	0.710	8838	12.24501	1.768724	2.503303	99.41356	6.923077	39.71296	731.0668

Run	Air Gap Residence time (s)	Extrusion Shear (1/s)	P O_2	P N_2	P CH_4	P CO_2	Ω (O_2/N_2)	Ω (CO_2/CH_4)	λ (Å)
1.4	0.947	8838	13.49557	3.168937	7.273501	96.81139	4.258704	13.31015	502.4635
1.4	0.947	8838	14.07639	2.801824	3.477355	85.88578	5.024007	24.69859	586.8556
1.4	0.947	8838	15.16605	2.180173	2.120968	78.35136	6.956351	36.94131	702.9947
1.4	0.947	8838	14.45346	2.75265	2.303313	83.16935	5.250745	36.10857	647.5811
1.4	0.947	8838	14.90377	2.526517	2.649395	76.54905	5.898939	28.89303	644.9551
1.4	0.947	8838	19.21154	4.338799	4.743547	85.37772	4.427846	17.99871	452.56

P= Pressure normalised flux x 10^6 [cm^3(stp)/(s cm^2 cmHg)], measured at 25°C and at a pressure differential of 5 bar.

Campaign 2: Varying Extrusion Shear, Constant Residence Time

Run	Air Gap Residence time (s)	Extrusion Shear (1/s)	P O_2	P N_2	P CH_4	P CO_2	Ω (O_2/N_2)	Ω (CO_2/CH_4)	λ (Å)
2.1	0.710	2945	3.133165	0.579244	0.56281	17.6132	5.409059	31.29513	2933.266
2.1	0.710	2945	2.770544	0.664008	0.756485	15.39318	4.172456	20.34829	2859.912
2.1	0.710	2945	3.619276	1.084542	1.555807	18.69761	3.337146	12.01795	1985.149
2.1	0.710	2945	3.266511	0.962131	1.299501	13.7377	3.39508	10.57152	2382.314
2.1	0.710	2945	2.762388	1.059847	0.489618	13.04083	2.606403	26.63469	3042.314
2.1	0.710	2945	2.412633	0.435056	0.434684	17.25167	5.545568	39.68783	3653.336

Run	Air Gap Residence time (s)	Extrusion Shear (1/s)	P O_2	P N_2	P CH_4	P CO_2	Ω (O_2/N_2)	Ω (CO_2/CH_4)	λ (Å)
2.2	0.710	5303	3.828958	1.51235	2.056385	17.07266	2.531793	8.30227	1828.231
2.2	0.710	5303	3.162538	0.621712	0.661948	18.47222	5.086826	27.90583	2738.852
2.2	0.710	5303	3.97869	0.669965	0.668923	23.8131	5.938655	35.59914	2374.546
2.2	0.710	5303	3.629454	1.235946	1.473335	16.29541	2.93658	11.06022	2037.898
2.2	0.710	5303	3.154596	0.538163	0.586464	19.67362	5.861787	33.54619	2888.299
2.2	0.710	5303	3.297298	0.517594	0.56394	20.61059	6.370436	36.5475	2884.757

P= Pressure normalised flux x 10^6 [cm^3(stp)/(s cm^2 cmHg)], measured at 25°C and at a pressure differential of 5 bar.

Run	Air Gap Residence time (s)	Extrusion Shear (1/s)	P O_2	P N_2	P CH_4	P CO_2	Ω (O_2/N_2)	Ω (CO_2/CH_4)	λ (Å)
1.3	0.710	8838	13.02414	1.830415	2.130244	85.18217	7.115404	39.98704	756.8638
1.3	0.710	8838	11.54858	1.514522	2.804508	91.81377	7.62523	32.73792	776.8907
1.3	0.710	8838	9.465252	1.713028	2.051996	82.44234	5.52545	40.17667	860.9207
1.3	0.710	8838	9.82236	1.405507	2.261793	91.90897	6.988483	40.63545	873.208
1.3	0.710	8838	14.49077	1.839372	1.883996	83.00305	7.878105	44.05692	763.1432
1.3	0.710	8838	12.24501	1.768724	2.503303	99.41356	6.923077	39.71296	731.0668

Run	Air Gap Residence time (s)	Extrusion Shear (1/s)	P O_2	P N_2	P CH_4	P CO_2	Ω (O_2/N_2)	Ω (CO_2/CH_4)	λ (Å)
2.4	0.710	11772	26.00547	15.22092	16.63486	83.87138	1.708535	5.041906	288.1678
2.4	0.710	11772	14.40968	5.091759	6.059594	55.55152	2.830001	9.167532	536.389
2.4	0.710	11772	16.2247	6.261375	6.925722	67.6191	2.591236	9.763473	455.7358
2.4	0.710	11772	18.33886	11.39797	15.80823	51.70845	1.608959	3.270983	424.8779
2.4	0.710	11772	11.20034	4.044341	5.287349	53.07218	2.769386	10.03758	629.9309
2.4	0.710	11772	11.40796	1.86424	1.715738	59.18835	6.119364	34.49732	884.817

P= Pressure normalised flux x 10^6 [cm^3(stp)/(s cm^2 cmHg)], measured at 25°C and at a pressure differential of 5 bar.

Gas Mixture Testing

Run	% O_2 in Permeate	P O_2	P N_2	Ω (O_2/N_2)	% CO_2 in Permeate	P CO_2	P CH_4	Ω (CO_2/CH_4)
1.2	83.88	9.95	1.33	7.50	96.17	57.4	1.45	39.68
1.2	82.88	10.1	1.46	6.92	96.49	61.6	1.41	43.61
1.2	82.89	9.23	1.33	6.92	96.51	59.2	1.35	43.87
1.2	84.12	9.72	1.27	7.65	96.71	56.8	1.22	46.72
1.2	81.77	11.3	1.78	6.33	95.63	64.7	1.87	34.63
1.2	83.37	10.4	1.44	7.20	96.34	57.5	1.38	41.71

P= Pressure normalised flux x 10^6 [cm^3(stp)/(s cm^2 cmHg)], measured at 25°C and at a pressure differential of 5 bar.

Appendix 2: 40% Polymer Fibre Gas permeation Testing

Uncoated Experimental Data

Campaign 3: Varying Residence Time, Constant Extrusion Shear

Run	Air Gap Residence time (s)	Extrusion Shear (1/s)	P O_2	P N_2	P CH_4	P CO_2	Ω (O_2/N_2)	Ω (CO_2/CH_4)
3.1	0.237	9118	1.235398	0.597154	0.87258	3.279056	2.068809	3.757885
3.1	0.237	9118	1.368824	0.948967	1.346801	3.322456	1.442436	2.466925
3.1	0.237	9118	0.99997	0.319767	0.409871	3.234794	3.127186	7.89223
3.1	0.237	9118	1.177978	0.29111	0.467743	3.801845	4.046509	8.128062
3.1	0.237	9118	1.53652	1.170928	1.717361	3.554674	1.312224	2.069847
3.1	0.237	9118	1.082138	0.560285	0.737971	3.110482	1.931408	4.21491

Run	Air Gap Residence time (s)	Extrusion Shear (1/s)	P O_2	P N_2	P CH_4	P CO_2	Ω (O_2/N_2)	Ω (CO_2/CH_4)
3.2	0.426	9118	0.631872	0.206434	0.237086	2.030967	3.060886	8.566355
3.2	0.426	9118	0.705896	0.246884	0.331189	2.154327	2.859221	6.504835
3.2	0.426	9118	0.57292	0.197946	0.254527	2.024184	2.894319	7.952715
3.2	0.426	9118	0.617765	0.248983	0.267222	1.962233	2.481151	7.34307
3.2	0.426	9118	0.624198	0.247416	0.260556	2.003299	2.522873	7.688567
3.2	0.426	9118	0.641052	0.186265	0.216802	1.965682	3.441607	9.066717

P= Pressure normalised flux x 10^6 [cm^3(stp)/(s cm^2 cmHg)], measured at 25°C and at a pressure differential of 5 bar.

Run	Air Gap Residence time (s)	Extrusion Shear (1/s)	P O_2	P N_2	P CH_4	P CO_2	Ω (O_2/N_2)	Ω (CO_2/CH_4)
3.3	0.710	9118	0.51002	0.13025	0.102131	1.902493	3.915692	18.62805
3.3	0.710	9118	0.524586	0.159027	0.121405	1.903826	3.298723	15.68157
3.3	0.710	9118	0.51077	0.170363	0.109788	1.849868	2.998131	16.84951
3.3	0.710	9118	0.527085	0.153839	0.126832	1.909576	3.426221	15.05599
3.3	0.710	9118	0.463473	0.152361	0.107697	1.715869	3.041944	15.9323
3.3	0.710	9118	0.546482	0.163794	0.117658	2.125431	3.336407	18.06455

Run	Air Gap Residence time (s)	Extrusion Shear (1/s)	P O_2	P N_2	P CH_4	P CO_2	Ω (O_2/N_2)	Ω (CO_2/CH_4)
3.4	0.947	9118	0.822036	0.189264	0.156138	3.053871	4.34332	19.55874
3.4	0.947	9118	0.765666	0.145854	0.149373	2.928142	5.249523	19.60286
3.4	0.947	9118	0.694898	0.137359	0.133018	2.727877	5.059008	20.50764
3.4	0.947	9118	0.822668	0.155681	0.147313	3.07581	5.284334	20.87948
3.4	0.947	9118	0.719354	0.131496	0.151796	2.625745	5.47052	17.29791
3.4	0.947	9118	0.774128	0.139255	0.143707	2.93441	5.559087	20.41939

P= Pressure normalised flux x 10^6 [cm^3(stp)/(s cm^2 cmHg)], measured at 25°C and at a pressure differential of 5 bar.

Campaign 2: Varying Extrusion Shear, Constant Residence Time

Run	Air Gap Residence time (s)	Extrusion Shear (1/s)	P O_2	P N_2	P CH_4	P CO_2	Ω (O_2/N_2)	Ω (CO_2/CH_4)
4.1	0.710	3038	1.311176	0.367572	0.410285	4.893594	3.567124	11.9273
4.1	0.710	3038	1.182331	0.302873	0.256057	4.873204	3.903723	19.03175
4.1	0.710	3038	1.008393	0.266502	0.29525	4.874252	3.783813	16.50889
4.1	0.710	3038	1.23538	0.24957	0.229286	5.105342	4.950026	22.2663
4.1	0.710	3038	1.321057	0.339231	0.281883	5.411539	3.894271	19.19785
4.1	0.710	3038	1.267641	0.323129	0.282876	5.182967	3.923025	18.32239

Run	Air Gap Residence time (s)	Extrusion Shear (1/s)	P O_2	P N_2	P CH_4	P CO_2	Ω (O_2/N_2)	Ω (CO_2/CH_4)
4.2	0.710	5471	1.291271	0.367572	0.410285	4.870667	3.512973	11.87142
4.2	0.710	5471	1.239841	0.317768	0.26865	5.11287	3.901719	19.03175
4.2	0.710	5471	1.230848	0.268625	0.297603	4.91309	4.582023	16.50889
4.2	0.710	5471	1.168343	0.262101	0.240798	5.361677	4.457603	22.2663
4.2	0.710	5471	1.31573	0.337863	0.280746	5.389719	3.894271	19.19785
4.2	0.710	5471	1.257541	0.320554	0.280622	5.045021	3.923025	17.97798

P= Pressure normalised flux x 10^6 [cm^3(stp)/(s cm^2 cmHg)], measured at 25°C and at a pressure differential of 5 bar.

Run	Air Gap Residence time (s)	Extrusion Shear (1/s)	P O_2	P N_2	P CH_4	P CO_2	Ω (O_2/N_2)	Ω (CO_2/CH_4)
4.3	0.710	9118	0.510002	0.13025	0.102131	1.902493	3.915692	18.62805
4.3	0.710	9118	0.524586	0.159027	0.121405	1.903826	3.298723	15.68157
4.3	0.710	9118	0.51077	0.170363	0.109788	1.849868	2.998131	16.84951
4.3	0.710	9118	0.527085	0.153839	0.126832	1.909576	3.426221	15.05599
4.3	0.710	9118	0.463473	0.152361	0.107697	1.715869	3.041944	15.9323
4.3	0.710	9118	0.546482	0.163794	0.117658	2.125431	3.336407	18.06455

Run	Air Gap Residence time (s)	Extrusion Shear (1/s)	P O_2	P N_2	P CH_4	P CO_2	Ω (O_2/N_2)	Ω (CO_2/CH_4)
4.4	0.710	12162	1.024511	0.306807	0.168904	3.381188	3.339266	20.01836
4.4	0.710	12162	0.983647	0.257295	0.243806	3.100273	3.823037	12.71617
4.4	0.710	12162	1.047951	0.22823	0.215996	3.338957	4.591633	15.45839
4.4	0.710	12162	0.879871	0.276783	0.256983	2.85771	3.178921	11.12025
4.4	0.710	12162	1.080823	0.208918	0.204807	3.254695	5.173442	15.89155
4.4	0.710	12162	0.959044	0.220021	0.230766	3.191322	4.358873	13.82926

P= Pressure normalised flux x 10^6 [cm^3(stp)/(s cm^2 cmHg)], measured at 25°C and at a pressure differential of 5 bar.

Coated Experimental Data

Campaign 1: Varying Residence Time, Constant Extrusion Shear

Run	Air Gap Residence time (s)	Extrusion Shear (1/s)	P O_2	P N_2	P CH_4	P CO_2	Ω (O_2/N_2)	Ω (CO_2/CH_4)	λ (Å)
3.1	0.237	9118	0.905026	0.212611	0.194979	2.96744	4.256726	15.21929	N/A
3.1	0.237	9118	1.146636	0.222721	0.246231	3.442983	5.148313	13.98272	N/A
3.1	0.237	9118	0.802834	0.173818	0.196548	2.598506	4.618831	13.22069	N/A
3.1	0.237	9118	1.116562	0.192163	0.209587	3.465466	5.810489	16.53471	N/A
3.1	0.237	9118	1.031233	0.300431	0.382004	3.042369	3.432512	7.964232	N/A
3.1	0.237	9118	1.003576	0.234523	0.219297	2.946669	4.279227	13.43688	N/A

Run	Air Gap Residence time (s)	Extrusion Shear (1/s)	P O_2	P N_2	P CH_4	P CO_2	Ω (O_2/N_2)	Ω (CO_2/CH_4)	λ (Å)
3.2	0.426	9118	0.738776	0.210665	0.249276	2.746519	3.506869	11.01797	N/A
3.2	0.426	9118	0.7792	0.243426	0.238207	2.459046	3.20105	10.32315	N/A
3.2	0.426	9118	0.670569	0.2048 4	0.169231	2.285395	3.273621	13.50461	N/A
3.2	0.426	9118	0.813857	0.201371	0.173171	2.671677	4.041587	15.42798	N/A
3.2	0.426	9118	0.683326	0.209151	0.212525	2.332834	3.267147	10.97677	N/A
3.2	0.426	9118	0.8250 7	0.205126	0.220345	2.778401	4.022255	12.60929	N/A

P= Pressure normalised flux x 10^6 [cm^3(stp)/(s cm^2 cmHg)], measured at 25°C and at a pressure differential of 5 bar.

Run	Air Gap Residence time (s)	Extrusion Shear (1/s)	P O_2	P N_2	P CH_4	P CO_2	Ω (O_2/N_2)	Ω (CO_2/CH_4)	λ (Å)
3.3	0.710	9118	0.571758	0.175448	0.149909	2.214406	3.258842	14.77169	N/A
3.3	0.710	9118	0.566005	0.153314	0.136603	2.083599	3.691797	15.25291	N/A
3.3	0.710	9118	0.637331	0.171896	0.149785	2.200941	3.707655	14.694	N/A
3.3	0.710	9118	0.616077	0.132173	0.142106	2.217926	4.661141	15.60751	N/A
3.3	0.710	9118	0.572057	0.182927	0.159798	2.167174	3.12725	13.56196	N/A
3.3	0.710	9118	0.56886	0.174055	0.165518	2.247345	3.268284	13.57768	N/A

Run	Air Gap Residence time (s)	Extrusion Shear (1/s)	P O_2	P N_2	P CH_4	P CO_2	Ω (O_2/N_2)	Ω (CO_2/CH_4)	λ (Å)
3.4	0.947	9118	0.628519	0.144669	0.123641	2.258718	4.34452	18.26842	N/A
3.4	0.947	9118	0.743464	0.17068	0.16508	2.422682	4.355889	14.6758	N/A
3.4	0.947	9118	0.723233	0.173593	0.170605	2.523898	4.166245	14.79383	N/A
3.4	0.947	9118	0.740572	0.16168	0.162977	2.667732	4.580493	16.36877	N/A
3.4	0.947	9118	0.680762	0.11709	0.125135	2.488219	5.814024	19.88421	N/A
3.4	0.947	9118	0.809288	0.156639	0.119171	2.87266	5.16657	24.1054	N/A

P= Pressure normalised flux x 10^6 [cm^3(stp)/(s cm^2 cmHg)], measured at 25°C and at a pressure differential of 5 bar.

Campaign 2: Varying Extrusion Shear, Constant Residence Time

Run	Air Gap Residence time (s)	Extrusion Shear (1/s)	P O_2	P N_2	P CH_4	P CO_2	Ω (O_2/N_2)	Ω (CO_2/CH_4)	λ (Å)
4.1	0.710	3038	1.152578	0.188806	0.191028	4.851965	6.104572	25.39926	8976.013
4.1	0.710	3038	0.974354	0.152046	0.19301	4.002178	6.408295	20.73556	10414.8
4.1	0.710	3038	1.100311	0.182581	0.185458	4.661332	6.026415	25.13412	9320.125
4.1	0.710	3038	1.05897	0.167128	0.207952	4.430135	6.336277	21.30361	9523.295
4.1	0.710	3038	1.107203	0.171208	0.199452	4.579516	6.466989	22.96044	9352.456
4.1	0.710	3038	0.998747	0.157832	0.178008	4.159788	6.327892	23.36857	10313.45

Run	Air Gap Residence time (s)	Extrusion Shear (1/s)	P O_2	P N_2	P CH_4	P CO_2	Ω (O_2/N_2)	Ω (CO_2/CH_4)	λ (Å)
4.2	0.710	5471	1.062733	0.172334	0.160232	4.894447	6.1667	30.54608	9769.128
4.2	0.710	5471	0.90937	0.173952	0.190205	4.492856	5.227704	23.62109	9978.645
4.2	0.710	5471	0.748811	0.157795	0.137287	2.543188	4.745453	18.52457	13585.33
4.2	0.710	5471	1.187734	0.205183	0.183712	5.580501	5.788659	30.37632	8507.913
4.2	0.710	5471	1.085765	0.181504	0.204455	4.84936	5.982044	23.71848	9072.312
4.2	0.710	5471	0.951366	0.172136	0.167667	4.016178	5.526843	23.95327	10455.82

P= Pressure normalised flux x 10^6 [cm^3(stp)/(s cm^2 cmHg)], measured at 25°C and at a pressure differential of 5 bar.

Run	Air Gap Residence time (s)	Extrusion Shear (1/s)	P O_2	P N_2	P CH_4	P CO_2	Ω (O_2/N_2)	Ω (CO_2/CH_4)	λ (Å)
3.3	0.710	9118	0.571758	0.175448	0.149909	2.214406	3.258842	14.77169	N/A
3.3	0.710	9118	0.566005	0.153314	0.136603	2.083599	3.691797	15.25291	N/A
3.3	0.710	9118	0.637331	0.171896	0.149785	2.200941	3.707655	14.694	N/A
3.3	0.710	9118	0.616077	0.132173	0.142106	2.217926	4.661141	15.60751	N/A
3.3	0.710	9118	0.572057	0.182927	0.159798	2.167174	3.12725	13.56196	N/A
3.3	0.710	9118	0.56886	0.174055	0.165518	2.247345	3.268284	13.57768	N/A

Run	Air Gap Residence time (s)	Extrusion Shear (1/s)	P O_2	P N_2	P CH_4	P CO_2	Ω (O_2/N_2)	Ω (CO_2/CH_4)	λ (Å)
4.4	0.710	12162	0.748952	0.184723	0.166392	2.512428	4.05446	15.0995	N/A
4.4	0.710	12162	1.017411	0.203374	0.187468	3.753978	5.002667	20.0246	N/A
4.4	0.710	12162	0.914088	0.188819	0.17673	2.951919	4.841087	16.70298	N/A
4.4	0.710	12162	1.04254	0.192746	0.19874	3.677936	5.408874	18.50623	N/A
4.4	0.710	12162	0.835975	0.1945 9	0.156778	2.947432	4.296091	18.80005	N/A
4.4	0.710	12162	0.877339	0.171925	0.148396	3.04929	5.103018	20.54835	N/A

P= Pressure normalised flux x 10^6 [cm^3(stp)/(s cm^2 cmHg)], measured at 25°C and at a pressure differential of 5 bar.

Gas Mixture Results

Run	% O_2 in Permeate	P O_2	P N_2	Ω (O_2/N_2)	% CO_2 in Permeate	P CO_2	P CH_4	Ω (CO_2/CH_4)
4.1	81.99	1.33	0.207	6.43	94.76	5.45	0.194	28.13
4.1	81.32	0.899	0.147	6.12	94.58	4.16	0.153	27.11
4.1	81.61	0.946	0.151	6.25	94.31	4.31	0.168	25.69
4.1	82.58	1.07	0.158	6.76	95.23	5.13	0.164	31.33
4.1	80.95	1.08	0.181	5.95	92.90	5.03	0.252	19.94
4.1	81.57	0.888	0.143	6.23	94.19	4.23	0.169	25.10

P= Pressure normalised flux x 10^6 [cm^3(stp)/(s cm^2 cmHg)], measured at 25°C and at a pressure differential of 5 bar.